INFORMATION TO USERS

This manuscript has been reproduced from the microfilm master. UMI films the text directly from the original or copy submitted. Thus, some thesis and dissertation copies are in typewriter face, while others may be from any type of computer printer.

The quality of this reproduction is dependent upon the quality of the copy submitted. Broken or indistinct print, colored or poor quality illustrations and photographs, print bleedthrough, substandard margins, and improper alignment can adversely affect reproduction.

In the unlikely event that the author did not send UMI a complete manuscript and there are missing pages, these will be noted. Also, if unauthorized copyright material had to be removed, a note will indicate the deletion.

Oversize materials (e.g., maps, drawings, charts) are reproduced by sectioning the original, beginning at the upper left-hand corner and continuing from left to right in equal sections with small overlaps.

Photographs included in the original manuscript have been reproduced xerographically in this copy. Higher quality 6" x 9" black and white photographic prints are available for any photographs or illustrations appearing in this copy for an additional charge. Contact UMI directly to order.

ProQuest Information and Learning
300 North Zeeb Road, Ann Arbor, MI 48106-1346 USA
800-521-0600

UMI®

SCANNING ELECTROCHEMICAL MICROSCOPY OF LIQUID/LIQUID AND LIQUID/MEMBRANE INTERFACES

by

BIAO LIU

A dissertation submitted to the Graduate Faculty in Chemistry in partial fulfillment of the requirements for the degree of Doctor of Philosophy, The City University of New York

2002

This manuscript has been read and accepted for the Graduate Faculty in Chemistry

in satisfaction of the dissertation requirement for the degree of Doctor of Philosophy.

2/26/2002
Date

Chair of Examining Committee

2/26/2002
Date

Executive Officer

Professor Ronald L. Birke

Professor Malgorzata Ciszkowska

Supervisory Committee

THE CITY UNIVERSITY OF NEW YORK

Abstract

Scanning Electrochemical Microscopy of Liquid-Liquid and Liquid-Membrane Interfaces

by

Biao Liu

Adviser: Prof. Michael V. Mirkin

The kinetic and the mechanistic aspects of charge transfers (ET and IT) across the liquid/liquid interfaces were investigated using scanning electrochemical microscopy (SECM). The rate constant of ET across the two immiscible electrolyte solutions (ITIES) is essentially independent of interfacial potential drop in the absence of interfacial adsorption of the common ion when the organic redox reactant is a neutral species. This result is in agreement with the widely accepted three-layer model of the ITIES. However, when a spacer (e.g., a molecular monolayer of a long-chain lipid) prevents the reactants from coming very close to the phase boundary, the interfacial potential drop between the aqueous and organic redox species increases, and the true potential dependence of the rate constant can be observed.

The solvent dynamics effect on ET at the ITIES was observed for the first time. The rate of the ET from ZnPor to $Ru(CN)_6^{3-}$ at the DCE/water interface was about three times as fast as the analogous reaction at the NB/water interface.

A new electrochemical generation/collection (G/C) technique based on the use of dual-pipet electrodes was developed for studying heterogeneous IT reactions and homogeneous chemical reactions involving ionic species. This technique allows quantitative separation of different charge transfer processes simultaneously occurring at the liquid/liquid interface. Using a dual-pipet device one can perform measurements in a thin liquid film formed on the surface of glass separating two barrels. In this way, voltammetry can be carried out "in the air", i.e., in the absence of the external liquid macrophase.

SECM was used to probe the redox activity of individual living cells. The possibilities of measuring the rate and investigating the pathway of transmembrane charge transfer are demonstrated. By this approach, the differences in the redox responses given by normal human breast epithelial cells and metastatic breast cancer cells were investigated. The correlation between redox activity and cellular metastasis was explored. Finally, the amperometric feedback and potentiometric modes of SECM were used to image the topography and map redox and acid-base activities in single mammalian cells.

Acknowledgements

I would like to thank Prof. Michael V. Mirkin for his guidance during this dissertation research. I also express thanks to Prof. Susan A. Rotenberg who gave support to the research project involving human cell studies.

The efforts of Dr. Xiaoguang Sun and Mr. Wei Chen to prepare living cells used in this research are gratefully acknowledged.

I express gratitude especially to Mr. Robert Wurman, whose technical support has been of such great value to me in this research.

I also thank Dr. Shaoyuan Hua who helped a lot at the beginning of this research.

A sincere acknowledgement to Prof. Ronald L. Birke, Prof. Malgorzata Ciskowska, Prof. David C. Locke, and Prof. Gerald Koeppl for their constant support and encouragement.

Finally, the financial support from the City University of New York, the Electrochemical Society, and the American Chemical Society is deeply appreciated.

Table of Contents

List of Tables

List of Charts

Chapter I

Charge Transfer at Liquid/Liquid interfaces - An Overview

1.1. Introduction

The elucidation of the structure and dynamics of the liquid/liquid interface is a fundamental problem of modern chemistry and biology (1,2). In addition to fundamental interest, the charge transfer (CT) reactions occurring at the liquid/liquid interface, i.e., electron transfer (ET) and ion transfer (IT), are relevant to important technological systems from chemical sensors to drug delivery in pharmacology to artificial photosynthesis (1-5). The liquid/liquid system usually consists of an aqueous phase and an immiscible organic phase. At the interface between the two immiscible electrolyte solutions (ITIES) one can conduct reactions that can not occur at solid electrodes, e.g., reactions involving species of very different polarities. The liquid/liquid interface has been suggested as a simple model for biological membranes. It is well known that cellular membranes play a key role in physiological reactions in a living system, and simple models of membrane function are therefore of considerable interest. The ITIES has been widely used for this purpose (2,6-8).

Electrochemical approaches are intrinsically suitable for the studies of CT at the ITIES, since CT across the interface gives rise to a current which is amenable to detection by conventional electrochemical techniques. In fact, electrochemical studies of the ITIES go back at least to the beginning of 20th century when Nernst and Riesenfeld observed ion transfer during the passage of current through the water/phenol interface (9). They were mainly interested in discovering a method to determine the transport numbers of inorganic electrolytes in non-aqueous solvents.

Although the analogy between the water/oil interface and biological membranes was realized soon after the above experiment (10), this field of electrochemistry has remained in the background for a long time. This was mainly due to a lack of knowledge of the interfacial structure and associated

potential distribution across the ITIES. The inherent difficulty in gathering reliable data because of iR drop in an organic phase also hindered the development in this field.

A first breakthrough came in the late 1960s when Gavach and co-workers demonstrated that liquid/liquid interfaces could be polarized like metallic electrode/electrolyte interface and that the Galvani potential difference between the two phases could be used as the driving force for CT reactions (11). This allowed the well established theory and methodology used for the study of CT reactions at metal/electrolyte solution interfaces to be used for studies at the liquid/liquid interfaces.

The second breakthrough was in the late 1970s when Samec and co-workers introduced the four-electrode potentiostat with iR drop compensation by using a positive feedback loop (12-14). This experimental approach opened the way to the studies of both the interfacial structure and CT reactions at the ITIES with modern electrochemical techniques such as cyclic voltammetry, chronoamperometry, differential pulse voltammetry, ac voltammetry and ac impedance.

In 1986, Taylor and Girault introduced micrometer-sized liquid/liquid interface supported at the tip of a pulled glass micropipette (15). Later, Girault's group developed another approach to micro-ITIES fabrication by making a microhole in a thin inert membrane using a UV laser photoablation technique (16). Compared to large ITIES, a micro-ITIES has a number of advantages typical of ultramicroelectrodes, i.e., the absence of the limitations caused by the charging current and iR-drop, relative simplicity of data analysis, and high mass-transfer rate essential for fast kinetic measurements. Because of a much lower ohmic drop, one can carry out electrochemical measurements at a micro-ITIES with low (or zero) concentrations of supporting electrolytes (17). This helps to alleviate the ion-pairing effect on charge transfer reactions. The micro-ITIES has been extensively employed in amperometric and potentiometric sensors (18,19).

Considerable research activities in the last two decades have stimulated theoretical studies in this field, and new models of interfacial structure and CT processes at the ITIES have been proposed. For

example, Marcus has expanded classical ET theory from metal/electrolyte interface to the ITIES, and proposed expressions for reorganization energy and the ET rate constant (20-22). Benjamin has employed molecular dynamics method to provide new insight about the structure of liquid/liquid interfaces and CT processes at the interfaces (23-27). The lattice-gas model has been utilized by Schmickler to describe the liquid/liquid interface and to predict the trends and orders of magnitude for various dynamic processes at the ITIES (28-30).

New approaches to study liquid/liquid interfaces have been developed in recent years. Amongst these are spectroscopic techniques and scanning electrochemical microscopy. UV-Visible and fluorescence detection have been successfully used to investigated the kinetics of CT at the ITIES (31-33). A nonlinear optical technique, i.e., second harmonic generation, can provide detailed picture of interfaces such as molecular orientation at the ITIES (34-36). More recently, scanning electrochemical microscopy (SECM) has emerged as a powerful tool for investigating CT processes at the ITIES (37-39). This technique allows one to separate IT from ET and is relatively insensitive to the resistance effects associated with conventional electrochemical measurements.

Our knowledge of the ITIES has significantly increased over the last two decades. Those advances have been summarized in several comprehensive reviews (1-2, 40-47). Nevertheless, some fundamental questions remain unanswered. In particular, the elucidation of the microscopic aspects of CT at the ITIES is still challenging. Obviously, a more realistic model of the interfacial structure has to be established, and more reliable experimental data are necessary for validating the developed theory.

1.2. Interfacial Structure and Adsorption of ions at ITIES

1.2.1. Interfacial Structure

The interpretation of many important interfacial phenomena, including CT reactions across the ITIES, is based on our understanding of the interfacial structure and potential distribution across the ITIES. For this reason, the interfacial structure has long been a primary concern of the electrochemical studies of ITIES.

The first theoretical study explaining the electrical double layer and potential distribution at the ITIES was introduced by Verwey and Niessen (VN) in 1939 (48). In their treatment, the ITIES was represented as two back-to-back diffuse layers on either side of the interface, one contains an excess of positive charge and the other an equal excess of negative charge. Each of these diffuse layers was described with the Gouy-Chapman theory (49) and the boundary between the two liquid phases was visualized as a mathematical plane separating the two space charge layers. The VN model was essentially an adaptation of the Gouy-Chapman model derived for the metal/electrolyte interface. Therefore, The limitation of the Gouy-Chapman model caused by assumptions that the ions are considered as point charges and the solvent is simply a dielectric continuum applies equally to the VN model.

The VN model was later modified by Gavach et al (50,51), who studied the ITIES formed between an aqueous solution of tetraalkylammonium bromide and nitrobenzene by measuring the interfacial tension with the drop weight method. According to this model, which is now often referred to as the modified Verwey-Niessen (MVN) model, the ITIES can be described as an inner layer composed of orientated solvent molecules separating the two space charge layers on both sides of the interface. Similar to the inner layer existing at the metal/solution interface, the inner layer at the ITIES separates the two planes of closest approach (Outer Helmoltz Plane, OHP) on both sides of the interface, as illustrated in figure 1.1.

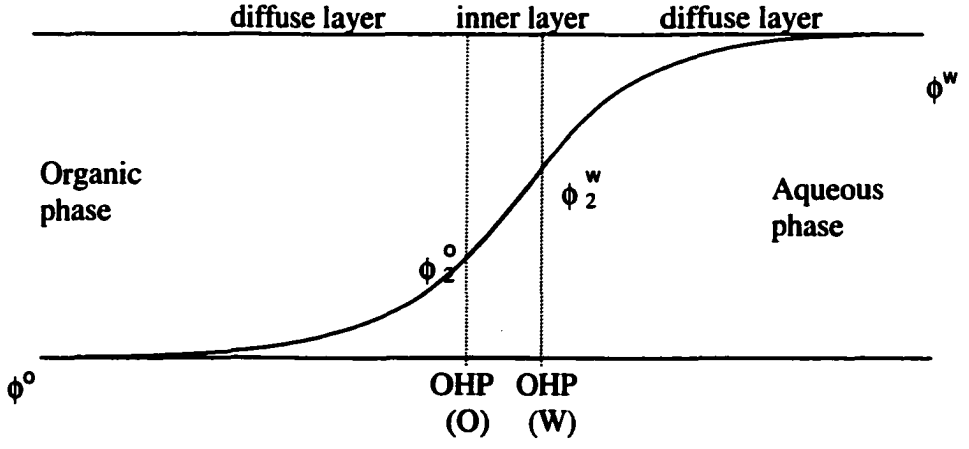

Figure 1.1. Modified Verwey-Niessen model of the ITIES.

In the MVN model, the overall potential difference between the aqueous phase (W) and the organic phase (O) has three components:

$$\Delta_o^w\phi = \phi^w - \phi^o = \Delta_{w2}^w\phi + \Delta_o^w\phi_{inn} - \Delta_{o2}^o\phi \qquad (1.1)$$

Where $\Delta_{w2}^w\phi = \phi^w - \phi_2^w$ is the potential difference between the bulk of aqueous phase (ϕ^w) and the OHP in aqueous phase (ϕ_2^w), $\Delta_{o2}^o\phi = \phi^o - \phi_2^o$ that between the bulk of organic phase (ϕ^o) and the OHP in organic phase (ϕ_2^o), and $\Delta_o^w\phi_{inn}$ is the potential difference cross the inner layer.

Gavach and coworkers found that the potential drop across the inner layer was negligible. This important conclusion was confirmed later by Buck et al who used similar experimental approach (52).

The MVN model was corroborated by Kakiuchi and Senda's research. They studied the interface between an aqueous lithium chloride and a nitrobenzene solution containing tetrabutylammonium tetraphenylborate (TBATPB) using a drop time method for the determination of interfacial tension (53-55). The researchers successfully explained their experimental results with the MVN model assuming that the inner layer of about 1 nm thickness is an ion-free layer consisting of laminated layers of water and nitrobenzene sandwiched between two diffuse layers. The potential difference across this inner layer was estimated to be about 20 mV at the potential of zero charge (pzc) but was found to vary with the surface charge density.

Around the same time, Samec et al. (56-59) measured double layer capacitance for different interfaces. Their work suggested the presence of the ion-free inner layer. They found that the MVN model could account for the experimental data. Again, their results confirmed that the potential drop across the inner solvent layer was negligible in the vicinity of the pzc. It is worth noticing that Samec and coworkers believe that ions are allowed to penetrate into the inner layer over some distance (60).

Compare to the metal/electrolyte interface, the inner layer capacity of an ITIES is rather high (54,59,60), and the values of the potential drop across the inner layer at the pzc are small (0 ~ 40 mV). These results were suggested to be due to ion interpenetration (45), which allows for a thinner inner layer. Surface tension measurements (62) and computer simulation (23,24) also suggested that interfacial solvent mixing and the penetration of ions into the inner layer are likely to occur.

Using a video technique to measure interfacial tension by the pendant drop method, Girault and Schiffrin studied the surface excess of water at the interface between aqueous electrolytes and pure organic solvents such as n-heptane, 1,2-dichloroethane, and nitrobenzene (61, 62). They observed that in the case of polar solvents, unlike at the air/electrolyte or metal/electrolyte interface, the surface excess of water was less than the equivalent of one monolayer. The negative adsorption of water at the interface suggested that ions penetrate the interfacial region. The measurements of water surface excesses also showed that the variation of the standard chemical potential is monotonic within the interface (62). Furthermore, their measurements of the pzc for the ITIES showed that the interfacial potential drop is negligible (63). All these findings led these authors to conclude that the interface region was not molecularly sharp, but comprised a mixed solvent layer (no more than two or three molecular diameter thick) where there was a gradual change in the solvent properties. An important implication of this model is that the interfacial potential difference is spread largely within the two back-to-back diffuse layers with a small potential drop across the mixed solvent layer (Figure 1.2).

The mixed solvent layer model considered the penetration of ions in the interfacial region, and postulated that the penetration of ions is directly correlated to their lipophilicity (63). The model has been corroborated by measurements of the adsorption of alkali metal cations at both the water/1,2-dichloroethane (DCE) and the water/nitrobenzene interfaces (64). The results suggested that the main origin of adsorption is interfacial ion-pairing between cations of one phase and anions of the other and that the ions may penetrate the mixed solvent layer to varying extends depending on the Gibbs energy of ionic hydration for a particular ion.

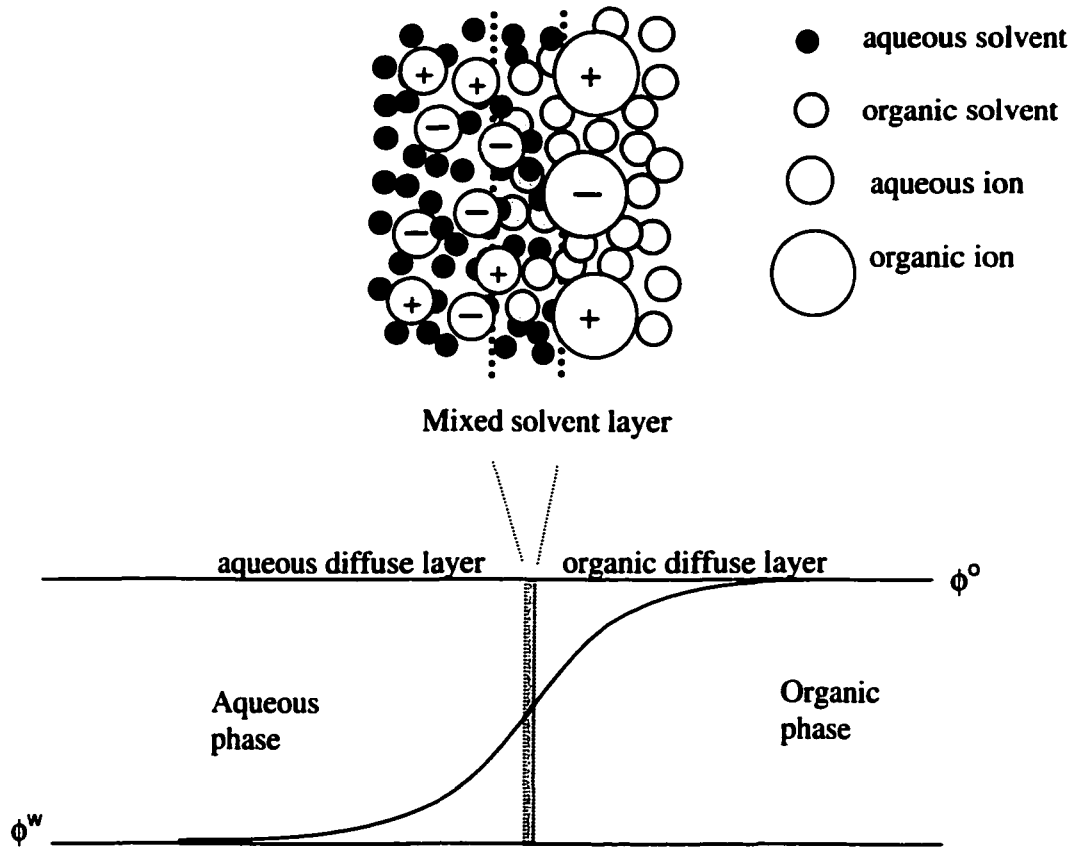

Figure 1.2. Mixed solvent layer model for a polarizable ITIES and schematic potential profile across the interfacial region.

More detailed microscopic pictures of the ITIES have been obtained recently by molecular dynamics and Monte Carlo computer simulations (26,27, 65). These studies show that the interface is molecularly sharp. However, thermal fluctuations of the solvents give rise to an apparent interfacial roughness, which is timescale dependent. With regard to pure solvents, the interfacial zone is within 10 Å at the picosecond time scale (23). The roughening of the interface may significantly affect the CT processes at the ITIES.

1.2.2. Interfacial Adsorption

The interfacial structure and the CT properties can be changed significantly by the adsorption of ions at the interface. The adsorption of some ions at the ITIES has been studied by electrocapillary (66,67), impedance (67), and optical (68) measurements. Recently, theoretical studies of specific ion adsorption and the effect of the adsorption on the interfacial CT reactions have been reported (69-71). The adsorption can be caused by ion pair formation between ions in the aqueous phase and ions in the organic phase, or with penetration of the ions into the interfacial region (58,64,68). The 'true' specific adsorption may occur at liquid/liquid interfaces when amphiphilic species are located at the interface with the hydrophobic and hydrophilic part in the preferred solvents (72-75).

The adsorption of ionic species can markedly change the structure of the diffuse double layer and hence the interfacial potential distribution. For example, adsorption of hexadecyltrimethylammonium ion at the nitrobenzene/water interface introduced the inversion of the potential difference across the nitrobenzene space charge region from a negative to a positive value (66). The dramatic change in potential profile due to ion adsorption has significant implications in studies of the kinetics of CT processes.

Adsorption of phospholipids at the ITIES has been studied by several groups (72- 75), The lipid monolayer was formed either by adsorption of phospholipids from the organic phase to the interface or by directly spreading a known amount of phospholipid solution at the liquid/liquid interface. Phospholipid monolayers typically become saturated at concentrations above 20 μmol dm^{-3} in the organic phase.

Numerous experimental results showed a remarkable dependence of interfacial adsorption on the potential drop across the interface (64,66-68). The adsorption of phospholipids also strongly depends on the pH values of the aqueous phase, which determines the surface ionization of the polar head of the phospholipid molecule and hence the stability of the adsorbed layer of phospholipids. (72,76).

The phase transition from the expanded to the condensed monolayer was induced by Ca^{2+} and Mg^{2+} in the case of dipalmitoylphosphatidylserine. The critical concentration was found to be 2 mmol dm^{-3} for both Ca^{2+} and Mg^{2+} to realize the phase transition (77). Some experimental results about the effect of lipid monolayer and its phase transitions on CT reactions at the ITIES will be shown in chapter 2.

1.3. Thermodynamic Aspects of CT at ITIES

1.3.1. Nernst Equations for the ITIES

In a liquid/liquid system, transferable species partition between the two immiscible solutions α and β. For a charged species i, the partition is determined by its electrochemical potential $\tilde{\mu}_i$ in each phase. The electrochemical potential, which represents the work required to transfer the ion *i* from the vacuum into a phase , can be divided into a chemical and an electrostatic part as:

$$\tilde{\mu}_i^{\alpha} = \mu_i^{\alpha} + z_i F \phi^{\alpha} \qquad (1.2)$$

where z_i is the charge of the ion, *F* is the Faraday constant, ϕ^{α} is the Galvani potential of the phase α, and μ_i^{α} is the chemical potential of the ion defined as:

$$\mu_i^{\alpha} = \mu_i^{0,\alpha} + RT \ln a_i^{\alpha} \qquad (1.3)$$

where $\mu_i^{0,\alpha}$ represents the standard chemical potential and a_i^{α} the activity of the ion in the phase α.

At constant pressure and temperature, the partition equilibrium is reached when the electrochemical potential is equal in both phases:

$$\tilde{\mu}_i^{\alpha} = \tilde{\mu}_i^{\beta} \tag{1.4}$$

The Galvani potential difference between the two phases can be derived by Substituting Eq. 1.2 and 1.3 into 1.4:

$$\Delta_{\beta}^{\alpha}\phi = \phi^{\alpha} - \phi^{\beta} = \Delta G_{tr,i}^{0,\alpha\to\beta} + \frac{RT}{z_i F}\ln(\frac{a_i^{\beta}}{a_i^{\alpha}}) \tag{1.5}$$

where $\Delta G_{tr,i}^{0,\alpha\to\beta}$ is the standard Gibbs energy of transfer, which represents the difference between the standard Gibbs energy of solvation of the ion in the respective phases:

$$\Delta G_{tr,i}^{0,\alpha\to\beta} = \mu_i^{0,\beta} - \mu_i^{0,\alpha} \tag{1.6}$$

Defining the standard ion transfer potential as:

$$\Delta_{\beta}^{\alpha}\phi_i^0 = \frac{\Delta G_{tr,i}^{0,\alpha\to\beta}}{z_i F} \tag{1.7}$$

an equation similar to the Nernst equation for the redox reactions at a metal/electrolyte interface can be obtained:

$$\Delta_{\beta}^{\alpha}\phi = \Delta_{\beta}^{\alpha}\phi_i^0 + \frac{RT}{z_i F}\ln(\frac{a_i^{\beta}}{a_i^{\alpha}}) \tag{1.8}$$

Eq. 1.8 is often referred to as Nernst equation for ion transfer at the ITIES. Since it is often more convenient to use the expression in terms of concentrations instead of activities, Eq. 1.8 can be rewritten in the form:

$$\Delta_{\beta}^{\alpha}\phi = \Delta_{\beta}^{\alpha}\phi_i^{0'} + \frac{RT}{z_i F}\ln(\frac{c_i^{\beta}}{c_i^{\alpha}}) \qquad (1.9)$$

where the standard transfer potential in Eq. 1.8 is replaced by the formal transfer potential $\Delta_{\beta}^{\alpha}\phi_i^{0'}$, which contains the activity coefficients γ_i :

$$\Delta_{\beta}^{\alpha}\phi_i^{0'} = \Delta_{\beta}^{\alpha}\phi_i^{0} + \frac{RT}{z_i F}\ln(\frac{\gamma_i^{\beta}}{\gamma_i^{\alpha}}) \qquad (1.10)$$

The Nernst equation for ET at the ITIES can be derived by considering a general ET process in a two-phase system schematically represented in Fig. 1.3.

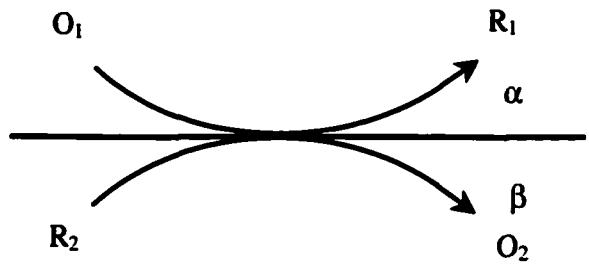

Fig. 1.3 The ET reaction at the ITIES.

Where O_1/R1 and R_2/O_2 represent the redox couples in the phases α and β, respectively. The ET reaction can be expressed as:

$$O_1^{\alpha} + R_2^{\beta} = R_1^{\alpha} + O_2^{\beta} \qquad (1.11)$$

The reaction Gibbs energy can be written in terms of the electrochemical potentials of the reactants and the products:

$$\Delta G_{tr,e^-}^{\beta\to\alpha} = \tilde{\mu}_{R_1}^{\alpha} + \tilde{\mu}_{O_2}^{\beta} - \tilde{\mu}_{O_1}^{\alpha} - \tilde{\mu}_{R_2}^{\beta} \tag{1.12}$$

From Eqs. 1.2 and 1.3, the following equation can be obtained:

$$\Delta G_{tr,e^-}^{\beta\to\alpha} = \tilde{\mu}_{R_1}^{0,\alpha} + \tilde{\mu}_{O_2}^{0,\beta} - \tilde{\mu}_{O_1}^{0,\alpha} - \tilde{\mu}_{R_2}^{0,\beta} - nF(\phi^{\alpha} - \phi^{\beta}) + RT\ln(\frac{a_{R_1}^{\alpha} a_{O_2}^{\beta}}{a_{O_1}^{\alpha} a_{R_2}^{\beta}}) \tag{1.13}$$

where n is the number of electrons transferred in reaction (1.11).

Introducing the standard reaction Gibbs energy ΔG^0:

$$\Delta G^0 = \tilde{\mu}_{R_1}^{0,\alpha} + \tilde{\mu}_{O_2}^{0,\beta} - \tilde{\mu}_{O_1}^{0,\alpha} - \tilde{\mu}_{R_2}^{0,\beta} \tag{1.14}$$

Eq. 1.13 can be rewritten as:

$$\Delta G_{tr,e^-}^{\beta\to\alpha} = \Delta G^0 - nF(\phi^{\alpha} - \phi^{\beta}) + RT\ln(\frac{a_{R_1}^{\alpha} a_{O_2}^{\beta}}{a_{O_1}^{\alpha} a_{R_2}^{\beta}}) \tag{1.15}$$

ΔG^0 of reaction 1.11 is connected with the standard potentials $E_{O1/R1}^{0,\alpha}$ and $E_{O2/R2}^{0,\beta}$ of the redox couple O_1/R_1 in the phase α and the redox couple O_2/R_2 in the phase β (both related to the same reference electrode) (78-80):

$$\Delta G^0 = nF(E_{O_2/R_2}^{0,\beta} - E_{O_1/R_1}^{0,\alpha}) \tag{1.16}$$

Substituting Eq. 1.16 into Eq. 1.15 yields

$$\Delta G_{tr,e^-}^{\beta\to\alpha} = nF(E_{O_2/R_2}^{0,\beta} - E_{O_1/R_1}^{0,\alpha}) - nF(\phi^{\alpha} - \phi^{\beta}) + RT\ln(\frac{a_{R_1}^{\alpha} a_{O_2}^{\beta}}{a_{O_1}^{\alpha} a_{R_2}^{\beta}}) \tag{1.17}$$

An important conclusion that can be drawn from Eq. 1.17 is that both the interfacial Galvani potential difference $\Delta_\beta^\alpha\phi$ and the difference between the standard potentials of the two redox couples (ΔE^0) could contribute to the driving force for the interfacial ET reaction. This is the main difference from homogeneous ET reactions in a single phase where ΔE^0 is the primary driving force. The difference is understandable considering the fact that the two-phase system has an extra degree of freedom for controlling the potential drop across the ITIES, provided that none of the species involved can partition to the opposite phase (80).

When ET reaction 1.11 is at equilibrium, $\Delta G_{ir,e^-}^{\beta\to\alpha}$ become zero. Thus, the Nernst equation for ET at the ITIES can be derived from Eq. 1.17:

$$\Delta_\beta^\alpha\phi = \Delta_\beta^\alpha\phi^0 + \frac{RT}{nF}\ln\left(\frac{a_{R_1}^\alpha a_{O_2}^\beta}{a_{O_1}^\alpha a_{R_2}^\beta}\right) \tag{1.18}$$

where $\Delta_\beta^\alpha\phi^0$ is the standard electron transfer potential defined as:

$$\Delta_\beta^\alpha\phi^0 = E_{O_2/R_2}^{0,\beta} - E_{O_1/R_1}^{0,\alpha} \tag{1.19}$$

1.3.2. Polarisability of the ITIES

Analogous to metal/electrolyte interface, an ITIES can be polarizable or non-polarizable. An ITIES at which no charge transfers across the interface, regardless of the potential imposed by an outside source of voltage, is called an ideal polarizable ITIES. The potential region in which the condition applies is called the "potential window" for the ITIES.

In practice, an ITIES can be polarized if the aqueous and the organic electrolytes are respectively very hydrophilic and very hydrophobic (e.g. LiCl in water, TBATPB in nitrobenzene or 1,2-

dichloroethane), as illustrated in the following electrochemical cell:

$$\text{Re1} \mid A_1B_1\,(O) \parallel A_2B_2\,(W) \mid \text{Re2} \qquad \text{Cell (1.1)}$$

where $A_1B_1$is a strongly hydrophobic 1:1 electrolyte dissolved in an organic phase, A_2B_2 is a strongly hydrophilic 1:1 electrolyte dissolved in an aqueous phase, the symbol $\parallel$ stands for the liquid/liquid interface, and Re1 and Re2 are the reference electrodes, which are reversible to either cation (A_1 or A_2) or anion (B_1 or B_2).

In terms of potential, the system cab be described by the following equations:

$$\Delta_o^w\phi_{A1}^0 << 0 \text{ and } \Delta_o^w\phi_{B1}^0 >> 0 \qquad (1.20)$$

$$\Delta_o^w\phi_{A2}^0 >> 0 \text{ and } \Delta_o^w\phi_{B2}^0 << 0 \qquad (1.21)$$

Under this conditions, $\Delta_o^w\phi$ is controlled by the electric charge in the double layer , which can be supplied from an external source. The potential window of a realistic system like Cell (1.1) is limited by the transfer of the electrolyte ions.

A non-polarizable ITIES is composed of two phases containing a common ion which is transferable across the interface:

$$\text{Re1} \mid A_1B_1\,(O) \parallel A_1B_2\,(W) \mid \text{Re2} \qquad \text{Cell (1.2)}$$

In case the transfer of both anions B_1 and B_2 is negligible, i.e.,

$$\Delta_o^w\phi_{B1}^0 >> 0 \quad \text{and} \quad \Delta_o^w\phi_{B2}^0 << 0 \qquad (1.22)$$

the potential difference between two phases is determined practically only by the activities of A_1 in both phases according to Eq. 1.8 if the concentrations of the salts In each phase are comparable (42).

A non-polarizable ITIES is characterized by the fact that a high current can pass through the interface without giving rise to a deviation of the interfacial potential from the equilibrium value. For this reason, it is usually employed as a reference electrode to define the potential of the organic phase. Recently, the non-polarizable ITIES has been used to study ET processes at the ITIES (81,82).

1.4. Kinetics of CT at ITIES

1.4.1. Electron transfer

Similar to CT processes at metal-electrolyte interfaces, an ET reaction at the ITIES

$$O_1^w + R_2^o = R_1^w + O_2^o$$

is composed of a series of elementary steps, including the mass transfer from bulk phase to the interface and the ET reaction at the interface. Extending the formalism for ET in homogeneous phase, the ET process at the ITIES has been describe by the pre-encounter model which involves the formation of a precursor complex followed by ET reaction (20,80,83):

$$O_1^w + R_2^o \leftrightarrows O_1^w|R_2^o \leftrightarrows \{O_1^w|R_2^o\} \overset{\nu}{\leftrightarrows} \{R_1^w|O_2^o\} \leftrightarrows R_1^w|O_2^o \leftrightarrows R_1^w + O_2^o$$

where $O_1^w|R_2^o$ and $R_1^w|O_2^o$ represent the precursor and the successor complexes respectively. $\{O_1^w|R_2^o\}$ is the precursor reorganized to a configuration appropriate for ET and $\{R_1^w|O_2^o\}$ is the reorganized successor before relaxation to the successor complex. ν is the effective electron hopping frequency. The phenomenological second order ET rate constant k_{obs} can be expressed as:

$$k_{obs} = Z \exp(-\Delta G_{act}/RT) \qquad (1.23)$$

where Z is the preexponential factor related to the geometric position of the precursor at the interface, ΔG_{act} is the activation energy determined by the reorganization energy λ, the formal Gibbs energy for the elementary electron transfer $\Delta G^{0'}$, and the work terms for precursor formation (w_r) and successor dissociation (w_p):

$$\Delta G_{act} = w_p + (\lambda + \Delta G^{0'} + w_p - w_r)^2/4\lambda \qquad (1.24)$$

By developing a formalism first introduced by Samec in 1979 (83), Girault and Schiffrin derived the equation of the potential dependence of ET rate constant based on the fact that the potential drop across the interfacial mixed solvent layer is negligible near the pzc (80):

$$k_{obs} = k_{obs}^{pzc} \exp(\frac{-z_{O1}F\Delta_w^a\phi - z_{R2}F\Delta_o^b\phi}{RT}) \exp(\frac{-\alpha nF\Delta_b^a\phi}{RT}) \qquad (1.25)$$

where a and b refer to the position of the reaction planes located in the aqueous and organic phase respectively, n is the charge transferred in the ET reaction, α is the transfer coefficient, $\Delta_a^b \phi$ is the potential distribution across the reaction planes, $\Delta_w^a \phi$ and $\Delta_o^b \phi$ are the potential differences across the space charge regions in aqueous and organic phase respectively, and k_{obs}^{pzc} is the rate constant measured at the pzc, which involves a number of parameters including the reorganization energy λ (80).

The Galvanic potential difference can affect the rate constant of an outer sphere electron-transfer reaction in two different ways: it can change the concentration of the reactants near the interface or the

free energy of the elementary step. The two mechanisms correspond to diffusion layer effect (or the so-called concentration polarization) and Butler-Volmer kinetics, respectively. Eq. 1.25 separates both of them. The first exponential term in Eq.1.25 reflects the effect of Galvanic potential on the work term (w_r), which corresponds to diffusion layer effect, while the second describes Butler-Volmer relationship (80).

Since the potential drop across the reaction region represents only a fraction of the Galvanic potential difference, i.e., $\Delta_a^b\phi$ is small, it is clear from Eq. 1.25 that the potential dependence of k_{obs} is mainly determined by the first exponential term in Eq. 1.25, implying that the concentration polarization phenomenon is predominant.

This result is supported by the lattice-gas modeling performed by Schmickler (28). Adopting the mixed solvent layer model for the ITIES, Schmickler calculated the particle distribution at the ITIES as a function of Galvanic potential difference and derived an explicit description of the effect of the Galvanic potential difference on the observed ET rate constant. These calculations indicated that a change in the potential drop across the ITIES has little effect on the free energy of the ET reaction as long as the Debye lengths in each electrolyte solution are larger than the width of the interface. In this case, the potential dependence of k_{obs} is caused mainly by changes in the interfacial concentration of reactants.

Extending the theory of homogeneous ET reactions and heterogeneous ET reactions at metal-electrolyte interfaces to liquid/liquid system, Marcus derived the general kinetic equation for ET reactions at a sharp liquid/liquid interface (20-22):

$$k_{obs} = 2\pi(a_1+a_2)(\Delta R)^3\kappa\nu \exp(-\Delta G_{act}/RT) \qquad (1.26)$$

where a_1 and a_2 correspond to the molecular radii of the reactants in the aqueous and organic phase

respectively; ΔR is a parameter relating ET rates to separation distance between the reactants and is typically 0.1 nm; κ is the transmission coefficient. ΔG_{act} is given by Eq. 1.24.

In order to fully evaluate Eq. 1.26, reorganization energy λ must be calculated. λ is classically defined as the sum of the solvent reorganization energy, λ_0, and the vibration energy, λ_i. For outer-sphere electron transfer reactions where no substantial changes in the structure of the redox species occur, λ_0 is predominant. Based on the continuum dielectric model, the expression for λ_0 was established (20,84):

$$\lambda_0 = \frac{(\Delta e)^2}{2a_1}\left(\frac{1}{\varepsilon_1^{op}} - \frac{1}{\varepsilon_1^{s}}\right) + \frac{(\Delta e)^2}{2a_2}\left(\frac{1}{\varepsilon_2^{op}} - \frac{1}{\varepsilon_2^{s}}\right) - \frac{(\Delta e)^2}{4d_1}\left(\frac{\varepsilon_2^{op} - \varepsilon_1^{op}}{\varepsilon_1^{op}(\varepsilon_2^{op} + \varepsilon_1^{op})} - \frac{\varepsilon_2^{s} - \varepsilon_1^{s}}{\varepsilon_1^{s}(\varepsilon_2^{s} + \varepsilon_1^{s})}\right)$$
$$- \frac{(\Delta e)^2}{4d_2}\left(\frac{\varepsilon_1^{op} - \varepsilon_2^{op}}{\varepsilon_2^{op}(\varepsilon_1^{op} + \varepsilon_2^{op})} - \frac{\varepsilon_1^{s} - \varepsilon_2^{s}}{\varepsilon_2^{s}(\varepsilon_1^{s} + \varepsilon_2^{s})}\right) - \frac{2(\Delta e)^2}{R}\left(\frac{1}{\varepsilon_1^{op} + \varepsilon_2^{op}} - \frac{1}{\varepsilon_1^{s} + \varepsilon_2^{s}}\right) \qquad (1.27)$$

where Δe is the charge transferred, ε^{op} *and* ε^{s} are the optical and static dielectric constants for both media, d_i is the perpendicular distance from the center of the reactant to the interfacial boundary, and R is the center-to-center distance between the two reactants.

Marcus also obtained an expression which relates k_{obs} to the rate constants of the two half reactions at the metal/electrolyte interface k_1^{el} and k_2^{el} (22). Assuming the liquid/liquid interface is a sharp boundary, the expression is given by Eq.1.28:

$$k_{obs} = [2\pi(a_1+a_2)\ \Delta R/\kappa v]\ k_1^{el}\ k_2^{el} \qquad (\Delta_o^w\phi = \Delta_o^w\phi^{0'}) \qquad (1.28)$$

In the case of an interfacial mixed layer rather than a sharp interfacial boundary, the expression becomes:

$$k_{obs} = [4\pi(a_1+a_2)^2 L/ \Delta R\kappa v]\, k_1^{el}\, k_2^{el} \qquad (\Delta_o^w\phi = \Delta_o^w\phi^{0'}) \qquad (1.29)$$

where L represents the thickness of the mixed layer.

Based on Eq. 1.28 and 1.29, Marcus estimated the value of k_{obs} and compared it with the experimental rate constant for the reaction between the $Fe(CN)_6^{4-/3-}$ couple in water and the $Lu(PC)_2^{+/2+}$ (hexacyano-ferrate-lutetium biphthalocyanine) couple in DCE. Although the model based on the mixed layer yielded a k_{obs} in better agreement with the experimental value, no definitive conclusion could be drawn due to the uncertainties in the k^{el}'s.

Unlike homogeneous ET and ET at the metal/solution interface where the well-established theory has been validated by numerous experiments, experimental data necessary for testing the theory of ET at the ITIES are sparse. Furthermore, the few experimental developments have been rather controversial.

A more conventional approach that has been used to study ET kinetics is based on application of external voltage across a polarizable interface employing four-electrode potentiostats. The applied voltage provides the driving force for an ET reaction. The thermodynamics and kinetics of such a reaction can be evaluated from the current vs. voltage curves (e.g., cyclic voltammograms). The first system that has been studied with this approach is ferrocene in nitrobenzene in contact with hexacyanoferrate (III) in water (78). The kinetic parameters of this ET reaction were evaluated by means of convolution potential sweep voltammetry, and the apparent rate constant was found to be almost independent of the potential and equal to $k \approx 4\times10^{-2}$ M^{-1} cm s^{-1}. However, the use of ferrocene as the organic redox species presents some problems due to the possible interfacial transfer of the ferricenium ion in the experimental conditions used and hence coupling of ET and IT may occur in this case.

By using cyclic voltammetry, Schiffrin and coworkers (85-87) studied the ET between the redox couple $Fe(CN)_6^{3-}/Fe(CN)_6^{4-}$ in water, and bis(pyridine)-*meso*-tetraphenylporphyrinato-iron (II) or rethenium (III) (86) and lutetium (III) and tin(IV) (87) diphthalocyanines in DCE. An essential advantage of these systems is that none of the reactants or products can cross the interface and interfere with the ET reaction. The concentration of the aqueous redox couple was much higher, thus the pseudo-first order ET reactions could be analyzed using Nicholson method (88). The apparent standard rate constant of the order of 10^{-3} cm s^{-1} was obtained (85-86). Some features of the apparent kinetic behavior of these ET reactions have been conformed by ac impedance measurements (89-90). The formal ET rate constants obtained with the ac technique were roughly of the same order as in the voltammetric measurements (85-86). Although the accuracy of the ac-impedance analysis far exceeds the previous studies based on cyclic voltammetry, the limited frequency range available for liquid-liquid interfaces (less than 1 kHz) imposes severe restriction for its application.

In contrast to the conventional studies of the ITIES at externally biased polarizable interfaces, the SECM experiments of ET have been carried out at a non-polarizable ITIES where two immiscible liquids contain a common ion. The interfacial potential drop ($\Delta_w^o\phi$) in this case is governed by the ratio of common ion concentration in water and in organic phase. With SECM one can quantitatively separate interfacial ET from IT processes and minimize resistive potential drop and double-layer charging effects. The SECM experiments at liquid/liquid interfaces have principally involved the determination of the steady-state tip current (i_T) as a function of the separation between the tip and the interface (d). The kinetic parameters of the interfacial ET reaction can be extracted by analyzing the i_T -d curves (the approach curves) with the theory developed previously (91-92).

Wei and coworkers first used SECM in 1995 (93) to investigate the ET reaction between ferrocene in nitrobenzene and FcCOONa in water. Tetraethylammonium perchlorate was applied in both phases as the potential determining electrolyte. When the bulk concentration of the reactant in phase 2 is in excess of the reactant in the phase containing the tip (phase 1) to exclude the possibility of diffusion

limitation in phase 2 (the constant composition approximation), the bimolecular ET rate constant, k_{12}, was found to be 0.2-0.6 M^{-1} cm s^{-1}.

With the same approach, Tsionsky et al. studied the potential dependence of the ET rate for the reaction between aqueous $Ru(CN)_6^{4-}$ and the oxidized form of zinc porphyrin (ZnPor) in benzene (81). In their study, ClO_4^- was used as the potential determining ion. Because the measured transfer coefficient, α, was about 0.5, it was concluded that conventional Butler-Volmer theory was applicable to heterogeneous ET at an ITIES.

Liu and Mirkin subsequently studied the oxidation of ZnPor in benzene by $Ru(CN)_6^{3-}$ in water (95). The ET rate was found to be essentially independent of the potential drop across the interfacial boundary, but dependent on the driving force contributed by the difference between standard potentials of the two redox couples (i.e., ΔE^0). The results were explained by the diffuse double layer effect predicted by known models of the liquid/liquid interface.

The SECM measurements of the interfacial ET between $ZnPor^+$ in benzene and $Fe(CN)_6^{4-}$ in water also showed a strong blocking effect of phospholipids adsorbed at the ITIES (82,94). The extent of the blocking effect depended on the driving force for ET and the fraction of the interface area covered with lipid. For complete monolayers of phospholipids, the ET rate constant was a function of the length of the hydrocarbon chain in the lipid molecule.

Recently (96), Barker et al. have extended the analysis of concentration profiles beyond the constant composition approximation preciously used for SECM studies, which allows measurements of very fast processes that would otherwise appear as diffusion controlled. For instance, when this approach was used to study the ET between $ZnPor^+$ in benzene and $Fe(CN)_6^{4-}$ in water, a reaction appearing to be diffusion-controlled in previous SECM studies (82), the analysis of the approach curves gives a unique rate constant, k_{12} = 91 cm s^{-1} M^{-1} (96). In addition to expending the range of rate constants that can be studied, the use of relatively low concentrations of the reactant in the second phase causes the

approach curves in the fast kinetic limit to be more readily distinguished from one another.

Studies of ET at micro-ITIES are scarce. Solomon and Bard first observed the ET between TCNQ in DCE and ferrocyanide in water at a micro-ITIES supported by micropipettes (97). The pipette was used as a SECM probe for electrochemical imaging.

Quinn et al. studied ET at micro-ITIES supported by micropipettes or microholes (98). The studied systems involved ferri/ferrocyanide redox couple in aqueous phase and ferrocene, dimethylferrocene, or TCNQ in either DCE or o-nitrophenyl octyl ether. Sigmoidal, steady state voltammograms were obtained for ET at the water/DCE interface. The semi-logarithmic plot of E versus $\log[(I_d-I)/I]$ was linear with the slope of 61 mV/decade, i.e., similar to the Nernstian value, 59 mV/decade, and the pipette resistance was too high for accurate kinetic measurements. An attempt was made to use the deviations from the reversible behavior to estimate kinetic parameters using the method previously developed for UMEs (99-100). However, the shape of measured voltammograms was imperfect, and the slope of the semi-logarithmic plot observed was much lower than expected from the theory. It was concluded that voltammetry at micro-ITIES is not suitable for ET kinetic measurements because of insufficient accuracy and repeatability (98). Those experiments may have been affected by reactions involving the supporting electrolytes, ion transfers, and interfacial precipitation. It is also possible that the data was at variance with the Butler-Volmer model because the overall reaction rate was only weakly potential-dependent (95) and/or limited by the precursor complex formation at the interface (80).

The progress in experimental and theoretical studies of ET at the ITIES has been developing swiftly in past 15 years. Techniques such as ac impedance, modulated and time-resolved spectroscopy, SECM, and photoelectrochemical measurements greatly extended our knowledge of the dynamics of heterogeneous electron transfer. For instance, the accessible values of the rate constant k_{12} have been increased from the order of 10^{-1} M^{-1} cm s^{-1} to the order of 10^{2} M^{-1} cm s^{-1}. One of the key issues remaining to be fully understand is the effect of the Galvanic potential difference on the ET rate

constant.

1.4.2. Ion transfer

Over the last two decades, much research work has been devoted to the measurements of the rate constants of IT across liquid/liquid interfaces. Classical galvanostatic or potentiostatic techniques, such as chronopotentiometry (101, 102), chronocoulometry (103), cyclic voltammetry (104), convolution potential sweep voltammetry (78) have been used in the measurements (104,105). The early kinetic measurements were performed without the proper ohmic drop compensation. As a result, rather low values of the standard rate constant were obtained ($10^{-3} - 10^{-4}$cm s^{-1}) (14,102,106,107).

Larger values of the standard rate constant ($10^{-2} - 5 \times 10^{-1}$ cm s^{-1}) were obtained if the ohmic drop was either numerically subtracted (101) or compensated (78,103, 108) with the help of the positive feedback.

Later on, ac polarography (109, 110) and the equilibrium impedance measurements (111-113) were used to study the kinetics of IT. The rate constants obtained by the ac impedance analysis are of the order of 0.1 cm s^{-1}, much higher than those obtained by techniques based on the passage of a direct current through the interface.

A micro-ITIES has been used to measure rapid heterogeneous IT kinetics. No steady-state theory for kinetically controlled heterogeneous IT has been developed for micropipettes. For a thin-wall pipette (e.g., RG ≤ 2, RG is the ratio of the glass radius to the aperture radius, r) the micro-ITIES is essentially uniformly accessible. When IT occurs via one-step first-order heterogeneous reaction governed by Butler-Volmer equation, steady-state voltammetric response can be calculated as (114)

$$i = i_d/(\theta + 1/\kappa) \qquad (1.30)$$

where i_d is diffusion limiting current, $\theta = 1 + \exp[(\Delta_o^w\varphi - \Delta_o^w\varphi^{o'})zF/RT]D_o/D_w$, and $\kappa = \exp[-\alpha(\Delta_o^w\varphi - \Delta_o^w$

$\varphi^{o'})$ zF/RT]k°/m, k° and α are the standard rate constant and the transfer coefficient, respectively, and m = AD/πr is the effective mass-transfer coefficient. The value of the factor A depends on RG. A similar kinetic equation derived for a microdisk electrode (99) should be more suitable for thick-wall pipettes (i.e., RG >> 1).

Girault et al. employed steady-state voltammetry at micropipettes to study facilitated transfer of potassium from aqueous phase to organic phase by dibenzo-18-crown-6 (DB18C6) (18b):

$$K^+ (w) + DB18C6 (O) \rightarrow [K^+DB18C6] (O) \qquad (1.31)$$

The semi-logarithmic plot (i.e., $\ln(I/(I_d - I))$ vs. potential) yielded a straight line with a slope of 39.9 V^{-1}. This number was very close to the 39.2 V^{-1} slope expected from the theory for a fully reversible charge transfer process at 23 °C. Both the slope and the half-wave potential were independent of the tip radius down to r = 0.6 μm. Thus, it was concluded that the transfer of potassium assisted by DB18C6 is essentially reversible under the experimental conditions. Using the theory developed by Oldham et al. for ultramicroelectrodes (UMEs) (99), the lower limit for the standard rate constant of that IT reaction was estimated to be 3 cm/s assuming hemispherical geometry of the micropipette-supported ITIES.

The assisted ion transfer of potassium and a few simple IT reactions at both micropipettes and microhole-supported ITIES (e.g., the transfer of tetramethylammonium (TMA^+) ion from water to DCE) were investigated by ac impedance technique (115). All experimental points for the TMA^+ transfer reaction yielded the k° values between 1.6 cm/s, and 32 cm/s (the latter value seems to be higher than the upper limit for the measurable rate constant under the conditions of ref.115). Thus the lower limit for the IT rate constant in ref. 115 is at least 1.6 cm/s, i.e., much higher than the k° values of the order of 0.1 cm s^{-1} measured previously at large ITIES. Similarly, for assisted transfer of potassium by DB18C6 the results of impedance measurements fit the theory for a fully reversible

process. The apparent standard rate constant is too high to be measured by ac impedance technique at micrometer-sized ITIES.

To increase the mass-transfer rate, Tokuda et al. (116,117) carried out normal and differential pulse voltammetry at micropipettes with the diameter from 3 to 10 μm. With this technique, they studied the transfer of some alkali and alkaline earth metal ions across water/nitrobenzene and water/DCE interfaces facilitated by two different crown ethers (DB18C6 and DB24C8). The rate constant values within the range from 0.009 to 0.2 cm/s were measured for facilitated transfers of Li^+, Na^+, Ca^{2+}, Sr^{2+} and Ba^{2+} to nitrobenzene (NB). The assumption of $\alpha = 0.5$ for all IT reactions and the use of iR-drop compensation may have affected the accuracy of those results. The upper limit for the measurable rate constant was about 0.5 cm/s, too slow to probe facilitated transfer of potassium ion.

It was shown later that a mass-transfer rate sufficiently high to measure the rate constant of potassium transfer (reaction 1.31) under steady-state conditions can be obtained using nm-sized pipettes ($r < 250$ nm) (114). Assuming uniform accessibility of the ITIES, the standard rate constant (k°) and transfer coefficient (α) were found by fitting the experimental data to Eq. (1.30). (Alternatively, the kinetic parameters of the interfacial reaction can be evaluated by the three-point method, i.e., the half-wave potential, $E_{1/2}$, and two quartile potentials, $E_{1/4}$ and $E_{3/4}$ (100,114)). A number of voltammograms obtained at 5- to 250-nm pipettes yielded similar values of kinetic parameters, $k^\circ = 1.3 \pm 0.6$ cm/s, and $\alpha = 0.4 \pm 0.1$. Importantly, no apparent correlation was found between the measured rate constant and the pipette size. The mass-transfer coefficient for a 10-nm-radius pipette is ≥10 cm/s (assuming $D = 10^{-5}$ cm^2/s). Thus, the upper limit for the determinable heterogeneous rate constant is at least 50 cm/s.

Alternatively, a higher rate of mass transport in steady-state measurements with a larger UME can be obtained by using it as a tip in SECM. SECM has typically been employed for probing interfacial ET reactions (91). Recently, micropipettes have been used as SECM probes to study IT reactions

(118,119). Although the possibility of probing simple and assisted IT at the ITIES by this technique was demonstrated, no actual kinetic measurements have yet been reported.

The effect of the formation of lipid monolayers at the liquid/liquid interface on the kinetics of interfacial IT was studied by several groups (76,77,120-122), and was discussed in several reviews (123-124). Those studies are important in elucidating the mechanism and kinetics of ion transport across a bilayer lipid membrane (BLM).

Both activation model and transport model have been proposed to describe the mechanism of the ion transfer across the ITIES. According to the former (109,112,125,126), certain activation energy is required for the ion to jump from one side of the inner layer to the other side over the potential energy barrier. This model indicates that the potential dependence of the transfer current should follow classical Butler-Volmer relationship, and that the apparent charge transfer coefficient, α_{app}, is around 0.5. However, the result is in conflict with what is expected based on the prevailing structure model of the ITIES (i.e., the mixed solvent layer model). Since the potential drop across the mixed layer is very small (1), any variation of the applied Galvani potential difference will induce tiny variation of the potential drop across the mixed layer. Therefore, the apparent charge transfer coefficient should be negligibly small if the potential gradient is the driving force of the IT reactions.

It could be argued that the potential dependence of the rate constant can be due to the diffuse layer effect similar to Frumkin effect at metal electrodes. Indeed, it has been proposed (127) that the true rate constant, k_t, which is the apparent rate constant corrected for the double layer effect, is potential independent and the Galvani potential difference only results in the variation of the surface concentration of the transferring ion. The data in the earliest kinetic analysis indicated that k_t was practically independent of the Galvani potential difference (78,101). However, more accurate measurements of the picrate ion transfer revealed a systematic change in k_t (108,111). The effect was reexamined for the Cs^+ ion transfer with a similar result (128).

The transport model considers the interfacial region as an inhomogeneous phase through which the solvent properties and salt concentrations of the adjoining phases vary continuously (129-133). This model does not assume the existence of an activation barrier. The expression for the IT rate was obtained by integrating the Nernst-Planck equation across the interfacial region under steady-state conditions. An important result of this analysis is that the transport model can explain the nonlinear current-voltage characteristics and a value close to 1/2 for the charge transfer coefficient was predicted, which was corroborated by experimental measurements. This model also related the standard rate constant, k^0, to the diffusion coefficient of the transferring ion across the interfacial region, D^{IL}, and the thickness of the interfacial layer, δ^{IL} :

$$k^0 = D^{IL}/\delta^{IL} \qquad (1.32)$$

Contrary to ET reactions where theories have been well established, the theories of IT kinetics at the ITIES remain rather controversial. Neither of the two models discussed above is able to account for all experimental results. The mechanism of the IT across the ITIES is still unclear, which reflects the general lack of our understanding of the molecular mechanism involved in ionic motion in liquids. Kinetic analysis strongly depends on the interfacial structure model. The mechanistic uncertainty of IT is largely due to the disputable interfacial structure models that have been used in developing the kinetic theories of IT. It is necessary to perform systematic studies to work out the accurate structure model of the liquid/liquid interface. The major issues to address also include determining the limiting step in the transfer of an ion across the ITIES and the potential dependence of the ion transfer rate.

1.5. Principles of SECM/ITIES Measurements

The theory, methodology, and instrumentation in SECM have been reviewed [91,92]. SECM has different operation modes. The feedback mode has been one of the most widely used SECM techniques applicable to the study of ET at the ITIES. The principle of this mode is illustrated in figure 1.4.

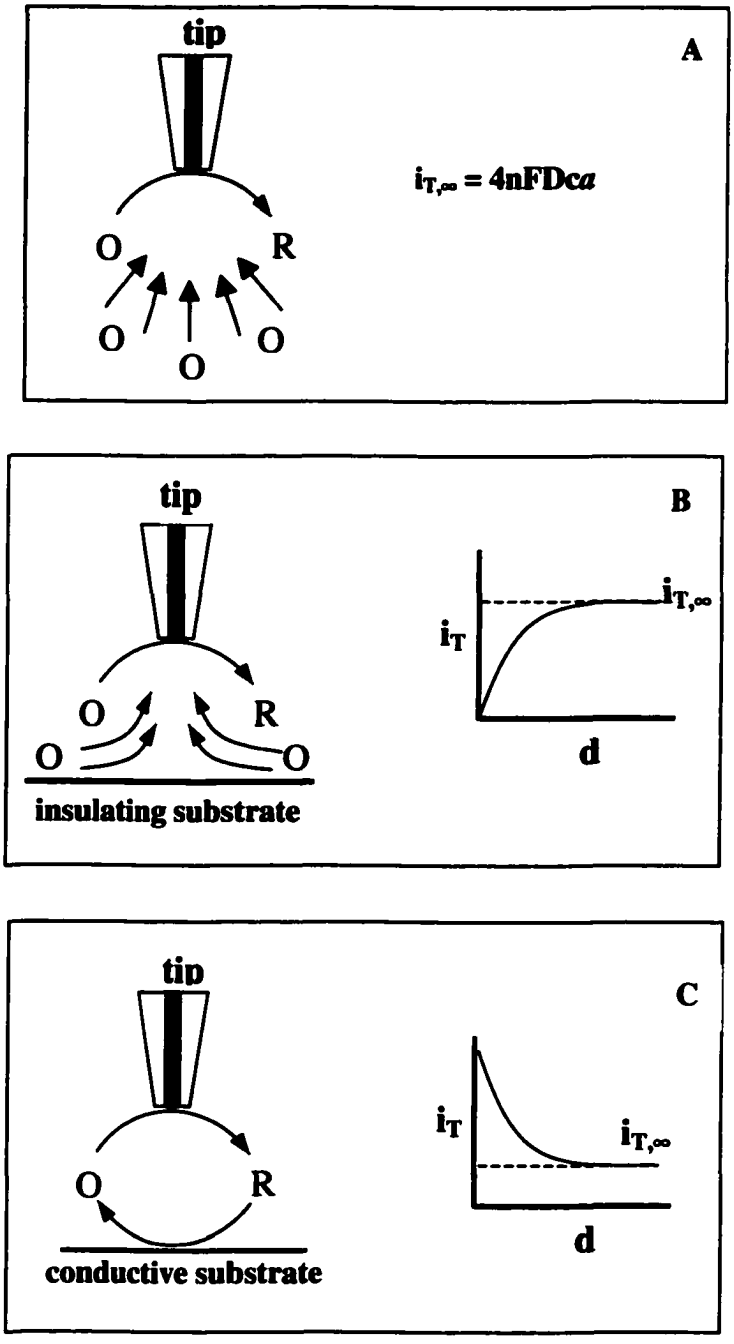

Fig. 1.4. The Feedback mode of SECM. (A) The tip is far from the substrate, diffusion leads to a steady-state current $i_{T,\infty}$; (B) The tip is near an insulating substrate, hindered diffusion leads to $i_T < i_{T,\infty}$; (C) The tip is near a conductive substrate, feedback diffusion leads to $i_T > i_{T,\infty}$.

When an ultramicroelectrode tip is far from the substrate, $d > 10a$, where d is the tip-substrate distance and a is the tip radius, a steady-state current, $i_{T,\infty}$, is rapidly established due to hemispherical diffusion of the redox species (O in Fig.1.4 A). The diffusion-controlled steady-state current is given by

$$i_{T,\infty} = 4nFDca \qquad (1.33)$$

where n is the number of electrons involved in the electrode reaction, F is the Faraday constant, D is the diffusion coefficient of species O and c the bulk concentration of O. As the tip is brought close to an electrically insulating substrate, the diffusion of O to the tip becomes hindered and the steady-state current, i_T, decreases compared to $i_{T,\infty}$ (Fig.1.4B). The decrease in current with distance is called negative feedback. The dependence of the $i_T/i_{T,\infty}$ ratio on d can be calculated theoretically (91). Thus, current measurements with mediators that do not interact at the substrate can be used to determine d.

When the tip is brought close to an electrically conductive substrate where the product of the tip reaction can be oxidized back to O, a flux of O from substrate to tip occurs in addition to the hindered mass transport of O to the tip from the bulk solution, which leads to $i_T > i_{T,\infty}$ (Fig.1.4C). The increase in current with distance is called positive feedback. In SECM, the curve of i_T versus tip-interface separation, d, is called an approach curve. The shape of an approach curve depends on the tip geometry and the reactivity at the substrate. Thus, by fitting an experimental approach curve to theoretical ones (see Eqs. 1.35 -1.38 below), the rate constant of the heterogeneous ET reaction at the interface can be obtained, which is the basis of using SECM to investigate ET across the ITIES.

Most SECM experiments are conducted with amperometric tips, yet the SECM measurement can be carried out in the potentiometric mode (134). In the potentiometric mode, an ion-selective microelectrode is used as the SECM tip. The potentiometric SECM measurement yields the potential of the tip electrode, E, as a function of the tip/target separation, d. By using a calibration curve which related E to the concentration of the determining ion, c, one can transform the E vs. d dependence to

the c vs. d dependence. In this way, the concentration profile of the determining ion around the target can be measured. The potentiometric mode has been used for monitoring corrosion, enzymatic reactions, and other heterogeneous processes (38,134). In the present work, the potentiometric mode was used for pH mapping of individual living cells (chapter 4).

In the SECM measurement of ET processes at the ITIES, an ultramicroelectrode tip is placed in the upper liquid phase containing either oxidized form O_1 or reduced form R_1 of a redox species (R_1 in Fig. 1.5). The bottom phase contains another redox couple R_2/O_2. The tip is biased at a potential where the oxidation of R_1 to O_1 is diffusion-controlled.

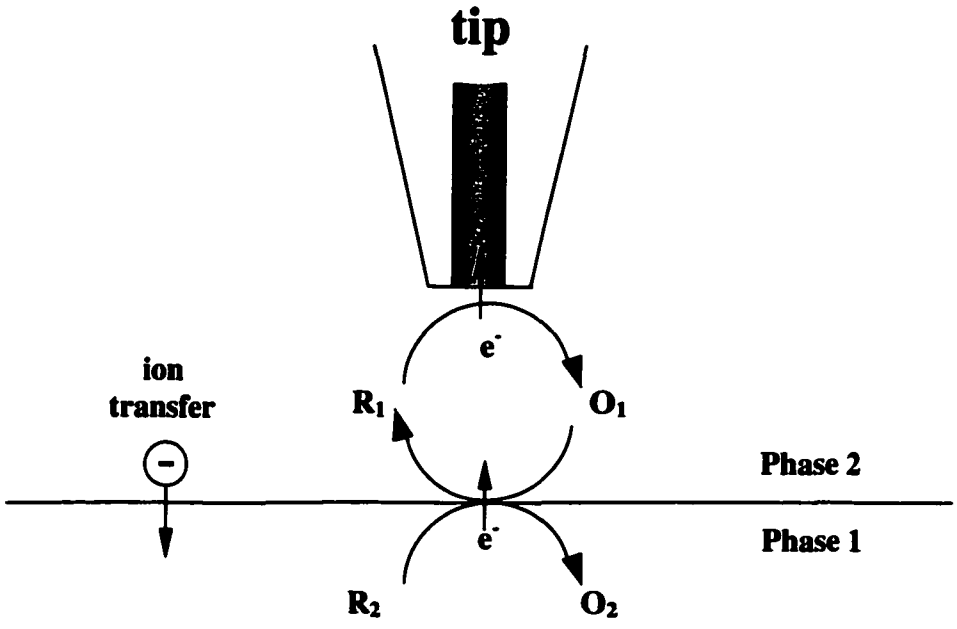

Fig. 1.5 Schematic diagram of the feedback mode SECM measurements of the kinetics of ET at the ITIES. Electroneutrality was maintained by transfer of common ions shown as negative charges.

When the tip approaches the ITIES, the tip-generated species (O_1) diffuses from the tip surface to the liquid/liquid interface. If the mediator can be regenerated at the interface via bimolecular redox reaction between O_1 in the upper phase and R_2 in the bottom phase:

$$R_1 - e \rightarrow O_1 \quad \text{(tip)} \qquad (1.34a)$$

$$O_1 + R_2 \rightarrow R_1 + O_2 \text{ (the ITIES)} \qquad (1.34b)$$

a feedback mode will be established in the same way as ET at solid substrates. As discussed above, the tip current will be larger than that seen in the negative feedback situation, depending on the rate of the interfacial ET reaction.

To maintain electroneutrality in both phases the transfer of common ions (either anions or cations or both) occurs simultaneously with ET reaction. Thus, the overall charge transfer reaction at the ITIES consists of several steps:

- mediator diffusion in phase 1
- mediator diffusion in phase 2
- ET between phase 1 and phase 2
- Transfer of the common ion (negative charge in Figure 1)

In principle, any of these steps can be rate-limiting. When IT and mediator diffusion in the bottom phase are not rate limiting, the following equations can be used to extract the first-order effective heterogeneous ET rate constant from approach curves [93]:

$$I_T^k = I_S^k (1 - I_T^{ins}/I_T^c) + I_T^{ins} \qquad (1.35)$$

$$I_S^k = 0.78377/L(1 + 1/\Lambda) + [0.68 + 0.3315\exp(-1.0672/L)]/[1 + F(L, \Lambda)] \qquad (1.36)$$

Where I_T^c, I_T^k, and I_T^{ins} represent the normalized tip currents for diffusion-controlled regeneration of redox mediator, finite substrate kinetics, and insulating substrate (i.e., no mediator regeneration), respectively, at a normalized tip-substrate separation, $L = d/a$; I_s^k is the kinetically controlled substrate current; $\Lambda = kd/D_R$, where k is the apparent heterogeneous rate constant (cm/s), and $F(L,\Lambda) = (11 + 2.3\Lambda)/[\Lambda(110 - 40L)]$. These currents are normalized by the tip current at an infinite tip-substrate separation, $i_{T,\infty}$. The analytical approximations for I_T^c and I_T^{ins} are [93]:

$$I_T^c = 0.78377/L + 0.3315\, exp(-1.0672/L) + 0.68 \quad (1.37)$$

$$I_T^{ins} = 1/(0.15 + 1.5358/L + 0.58\, exp(-1.14/L) + 0.0908\, exp[(L - 6.3)/(1.017L)]) \quad (1.38)$$

1.6. The scope of the present work

The purpose of the present work was mainly to study the kinetic and the mechanistic aspects of charge transfers (ET and IT) across the liquid/liquid interfaces using microelectrochemical techniques. The results were used to test the ET theory. Another objective was to apply the developed methodologies to the studies of the redox activities of living cells, in which interfacial electron and ion transfers are of great importance.

This thesis is organized as follows:

Chapter 2 describes the SECM measurements of the rate constants of ET reactions at the liquid/liquid interface and long-rang ET across phospholipid monolayers. Fundamental issues such as potential dependence of the ET rate constants and the effects of solvent dynamics, ionic adsorption, electrolyte concentration, and spacer length on the reaction rate are discussed.

Chapter 3 shows that the rates of IT across the phase boundary can be measured using a dual-pipet electrochemical technique. The possible application of dual-pipette electrodes to gas sensing is also

described in this chapter.

In chapter 4, the application of SECM to probe the redox activity of individual living cells is described. The possibilities of measuring the rate and investigating the pathway of transmembrane charge transfer are demonstrated. By this approach, the differences in the redox responses given by normal human breast epithelial cells, breast cells that overexpress protein kinase Cα and metastatic breast cancer cells were investigated. The correlation between redox activity and cellular metastasis was explored. Finally, the amperometric feedback and potentiometric modes of SECM were used to image the topography and map redox and acid-base activities in single mammalian cells.

Chapter II

SECM Studies of Electron Transfer at the ITIES

2.1 Introduction

The emerging interest in studies of electron transfer (ET) processes at the interface between two immiscible electrolyte solutions (ITIES) during last several years is due to its fundamental importance and a number of novel applications from artificial photosynthesis (1) to liquid redox extraction (2). Several recently developed electrochemical (3-5), and spectro-electrochemical (6,7) techniques allow kinetic measurements and mechanistic studies of this process which were problematic just a few years ago (8). As expected from theory (9-11), the probed reactions were found to be of the first order in both organic and aqueous redox species and the effective heterogeneous rate constants were strongly dependent on the difference between standard potentials of two redox couples (ΔE°). Perhaps the most controversial point in this area is the contribution of the interfacial potential drop to the driving force for ET reaction.

Following the approach of Schiffrin and co-workers (12), in many recent experimental studies one phase contained concentrated redox species and was considered metal-like. Similar to metal/solution electrochemistry, heterogeneous ET was assumed to be driven by the potential drop across the interfacial boundary (for the ITIES this is the difference of Galvani potentials of the organic and aqueous phases, $\Delta_w^o \phi$ (8)). Accordingly, the dependence of the ET rate constant on $\Delta_w^o \phi$ should be exponential (Butler-Volmer kinetics) at low overpotentials and level off at much higher overpotentials according to Marcus theory (9-11). This was either an explicit (12,13) or an implicit (9,11) assumption in most theoretical and experimental studies.

One should notice that the Butler-Volmer equation is applicable only if most of the interfacial potential drop occurs between the reacting redox moieties. This assumption is in conflict with a widely accepted mixed layer model of the ITIES (14-16) proposed by Girault and Schiffrin and further developed by Schmickler. According to this model, the ET rate constant is essentially potential-independent because the potential drop across the mixed-solvent layer separating aqueous and organic redox species is small

(14,16,17). The apparent dependence of the ET rate on $\Delta_w^o \phi$ is due to the diffuse layer effect similar to Frumkin effect at metal electrodes (18), which may result in either accumulation or depletion of a reactant species in the proximity of the phase boundary (mostly on the organic side (14,16,17)). Deviations from Butler-Volmer equation at the ITIES have been observed experimentally (6,7,13). However, only one group has previously reported potential-independent ET rate at the ITIES (19) and those results are somewhat less reliable because of the transfer of ferrocenium ion that could occur simultaneously with ET (8,12).

Recently, scanning electrochemical microscopy (SECM) has been employed to probe ET at the non-polarizable (20-23), and polarizable (24) ITIES. Those studies identified the experimental conditions under which interfacial electron transfer can be probed and demonstrated that ET can be quantitatively separated from ion transfer processes. In one of those experiments (3,4) the ultramicroelectrode (UME) tip was positioned in the top, benzene (BZ), layer containing zinc porphyrin (ZnPor) and approached the bottom, aqueous, layer containing $Ru(CN)_6^{4-}$. The redox reactions at the tip and the ITIES were as follows:

$$ZnPor - e \rightarrow ZnPor^+ \qquad \text{(tip in benzene)} \qquad (2.1a)$$

$$ZnPor^+ (o) + Ru(CN)_6^{4-} (w) \xrightarrow{k_f} ZnPor (o) + Ru(CN)_6^{3-} (w) \text{ (ITIES)} \qquad (2.1b)$$

The ET rate constant of reaction 2.1b was evaluated from the tip current vs distance curves. To probe the potential dependence of the rate constant, $\Delta_w^o \phi$ was varied by changing the concentration of the common ion in the aqueous phase ($[ClO_4^-]_w$). For reaction (2.1b), the $\ln k_f$ vs. $\Delta_w^o \phi$ dependence was linear with a transfer coefficient, $\alpha = 0.5$. Thus, it was proposed that the ET kinetics can be described by Butler-Volmer model, and the driving force for the interfacial ET reaction is the sum of the $\Delta_w^o \phi$ term and the difference of standard potentials of the organic and aqueous redox mediators (3,4):

$$\Delta G^{\circ} = -F(\Delta E^{\circ} + \Delta_W^O \phi) \qquad (2.2)$$

However, the results of ref (3) do not allow one to unambiguously distinguish between the predictions of two models. According to Schmickler's model (17), the observed increase in ET rate with the $\Delta_W^O \phi$ can be attributed to accumulation of $ZnPor^+$ at the interface rather than to increasing driving force for ET.

Our work aimed to clarify the origin of the apparent potential dependence of the ET rate by measuring the kinetics of the reverse ET reaction. In this case the tip UME is positioned in the aqueous phase containing $Ru(CN)_6^{4-}$ and approaches the organic layer containing ZnPor:

$$Ru(CN)_6^{4-} - e \rightarrow Ru(CN)_6^{3-} \qquad \text{(tip in water)} \qquad (2.3a)$$

$$Ru(CN)_6^{3-}(w) + ZnPor(o) \xrightarrow{k_b} ZnPor^+(o) + Ru(CN)_6^{4-}(w) \quad \text{(ITIES)} \qquad (2.3b)$$

Unlike interfacial reaction 2.1b, the electron acceptor in reaction 2.3b is anionic and the electron donor is a neutral species. If the Butler-Volmer model is operating, the k_b should increase exponentially when the organic phase is made more negative. However, the concentration of the neutral ZnPor at the interface is potential-independent, and the interfacial concentration of negatively charged $Ru(CN)_6^{3-}$ decreases with increasing negative value of $\Delta_W^O \phi$. Since almost all interfacial voltage drops within the diffuse layer in organic solvent (7) the effect of $\Delta_W^O \phi$ on surface concentration of $Ru(CN)_6^{3-}$ is small. Therefore, Schmickler's model predicts that the rate of the reaction 2.3b is practically independent of $\Delta_W^O \phi$.

Another objective of this work is to compare the kinetics of long-range ET across monolayers of different phospholipids adsorbed at the ITIES. Our interest in studying ET across phospholipid films at the ITIES is twofold. First, A liquid/liquid interface covered with a phospolipid monolayer is a better model for biological membranes than a clear ITIES (25,26). Studying ET reactions across lipid films will help us to better understand similar CT processes in living cells (see Chapter IV). On the other hand, by separating the electron donor and acceptor with a well-defined spacer one can slow down the ET rate and carry out

measurements at high overpotentials in order to check the ET theory (27-29).

An earlier SECM study (4) showed that adsorption of symmetric saturated lipids (1,2-dicacyl-*sn*-glycero-3-phosphocholine) with a different number of methylene groups in a hydrocarbon chain (n) on the water/BZ interface results in a formation of a compact monolayer. The defect density in the film was too low to produce detectable feedback current. Although the redox reactants (i.e., $ZnPor^+$ in BZ and $Fe(CN)_6^{4-}$ in water) were separated by the lipid film, and the rate of ET decreased markedly with the increasing length of the spacer, the analysis of distance dependence of the rate constant suggested partial penetration of $ZnPor^+$ into the lipid layer. This prevented quantitative interpretation of the k_f vs. n results.

In this work we explore the possibility of improving the blocking properties of a spacer by using another family of saturated symmetric phospholipids, i.e., 1,2-diacyl-*sn*-glycero-3-phospho-L-serines. An interesting feature of phosphatidylserine films is that their structure can be easily and predictably changed. The liquid expanded monolayers formed by these lipids at the ITIES at room temperature (30,31) undergo a sharp phase transition and become solid upon addition of a low concentration of a divalent cation (e.g., Ca^{2+} or Mg^{2+}) (31). Such films are supposed to be tightly packed and may not be permeable for large porphyrin molecules.

Several other factors affecting the rate of ET reactions at the non-polarized ITIES were also investigated in this work. Those factors include the solvent effect, ionic adsorption, and electrolyte concentration.

2.2 Experimental Section

2.2.1 Chemicals

5,10,15,20-tetraphenyl 21H, 23H- porphine zinc (ZnPor), Benzene (spectrophotometric grade), 1,2-dichloroethane (99.8% HPLC grade), $NaClO_4$ and NaCl from Aldrich (Milwaukee, WI), and $Na_4Fe(CN)_6$ (Fisher Scientific, Fair Lawn, NJ) were used as received. $Na_4Ru(CN)_6$ was synthesized as reported previously (3,32), recrystallized several times from methanol:water and dried under vacuum overnight at 50 °C. Tetrahexylammonium perchlorate ($THAClO_4$; Johnson Matthey, Ward Hill, MA) was recrystallized

twice from an ethylacetate:ether (9:1) mixture and dried under vacuum overnight at room temperature. Tetrabutylammonium chloride (TBACl), and nitrobenzene (>99%) were from Fluka Chemika, Switzerland. 7,7,8,8-Tetracyanoquinodimethane (TCNQ) from Aldrich was recrystallized twice from acetonitrile. Tetrabutylammonium hexafluorophosphate ($TBAPF_6$) from Fluka Chemika was recrystallized twice from ethyl acetate. All organic solutions were washed with a larger volume of Milli-Q water several times before measurements to remove impurities from the organic phase. All other chemicals were ACS reagent grade.

Chloroform solutions of symmetric saturated synthetic lipids (1,2-dicacyl-*sn*-glycero-3-phosphocholine and 1,2-diacyl-*sn*-glycero-3-[phospho-L-serine]) with different numbers of methylene groups in a hydrocarbon chain (n = 10, 12, 16; the abbreviations C-10, C-12, etc., will be used to designate different phospholipids) from Avanti Polar Lipids, Inc. (Alabaster, AL) were stored at –20 °C. Before an experiment, a flow of nitrogen was passed above a small volume (~40 μL) of phospholipid solution in chloroform for complete evaporation of solvent. The precipitated lipid was then redissolved in BZ to prepare a 500 μM stock solution, which also contained ZnPor and supporting electrolyte. The mixture of the lipid stock solution and BZ solution containing the same concentrations of ZnPor and $THAClO_4$ served as the organic phase.

2.2.2 Electrodes and Electrochemical Cells

The preparation of ultramicroelectrodes was similar to that reported previously (33). A Pt, Au, or carbon wire of the desired radius (1 ~ 12.5 μm) is sealed at one end of a Pyrex glass tube (2 mm o.d. and 1 mm i.d.) which is about 10 cm long. The sealed end of the tube is heated with a coiled nichrome wire. At the same time, the open end of the tube is connected to a vacuum line to remove any impurities from capillary. One end of the wire is then sealed in glass by increasing the heating coil temperature. After the glass has cooled, the electrode is inspected with a microscope to make sure that the wire is completely sealed at the tip and that there are no trapped air bubbles. The sealed end of the tip is ground with sandpaper, until the wire cross section is exposed. Next, the tip is polished on a polishing wheel successively with 15-, 6-, 3-, and 1-μm diamond paste and finally with 0.05-μm alumina (Buehler, Lake Bluff, IL) until the surface looks mirror smooth. Electric connection to the unsealed end of the wire is made with silver epoxy (Epotek H20E, Epoxy Technology, Inc., Billerica, MA) to a Cu wire. The epoxy is inserted into the glass tube with

a disposable syringe and is cured at 100 °C for two hours. A small amount of Torr Seal epoxy (Varian Vacuum Technology, Lexington, MA) is then put into the open end of the glass tube so that the electric wire is completely embedded.

The glass wall surrounding the Pt or Au or carbon wire is then conically sharpened with emery paper (Grit 600, Buehler) and 6-μm diamond paste. Finally, the tip is checked by measuring the approach curve on an electrically insulating substrate or a liquid/liquid interface with the bottom phase containing no mediator. The tip current decreases as the tip approaches the interface because of negative feedback. For a good tip, the value of the normalized tip current ($i_T/i_{T,\infty}$) should decrease down to 0.1 or smaller at the closest distance between the tip and the interface.

A 5-mL vial mounted on a vibration-isolated horizontal stage was used as the electrochemical cell for SECM measurements. A three-electrode setup was employed with a 12.5-μm-radius Pt UME tip, a Pt wire as the counter electrode and a Ag/AgCl reference electrode; all three electrodes were placed in the top liquid phase. The UME tip was rinsed with ethanol and water and then polished with 0.05-μm alumina and dried before each measurement. When the top phase was organic, an ionic bridge containing a solution of NaCl and $NaClO_4$ (or TBACl) was placed between the Ag/AgCl reference electrode and organic solution.

To measure the rate of reaction 2.1b, the top phase contained a solution of 0.25 M $THAClO_4$, 0.5 mM ZnPor, and 0–100 μM lipid in BZ; and the bottom phase contained a solution of 7 mM of $Na_4Ru(CN)_6$ or $Na_4Fe(CN)_6$, 0.1 M NaCl, and 0.01–2 M $NaClO_4$. To measure the rate of reaction 2.3b, the top phase contained a 0.1 mM solution of $Na_4Ru(CN)_6$, 0.1 M NaCl, and 0.01–2 M $NaClO_4$ or 5 - 100 mM TBACl; and the bottom (organic) phase contained a solution of 2 mM ZnPor, 1 - 100 mM $THAClO_4$, or 10 - 200 mM $TBAPF_6$ in DCE or NB or BZ. The steady-state voltammograms of ZnPor in solutions containing TBA^+ (Figure 2.1) were very similar to those obtained in perchlorate solutions (Figure 2.2). The voltammogram of ZnPor consists of two well-defined waves corresponding to two one-electron oxidations of ZnPor to $ZnPor^+$ and then to $ZnPor^{2+}$ (3). The electrochemical cell designed to keep a lower density liquid phase (e.g., BZ) under a heavier liquid (e.g., water) was described previously (34).

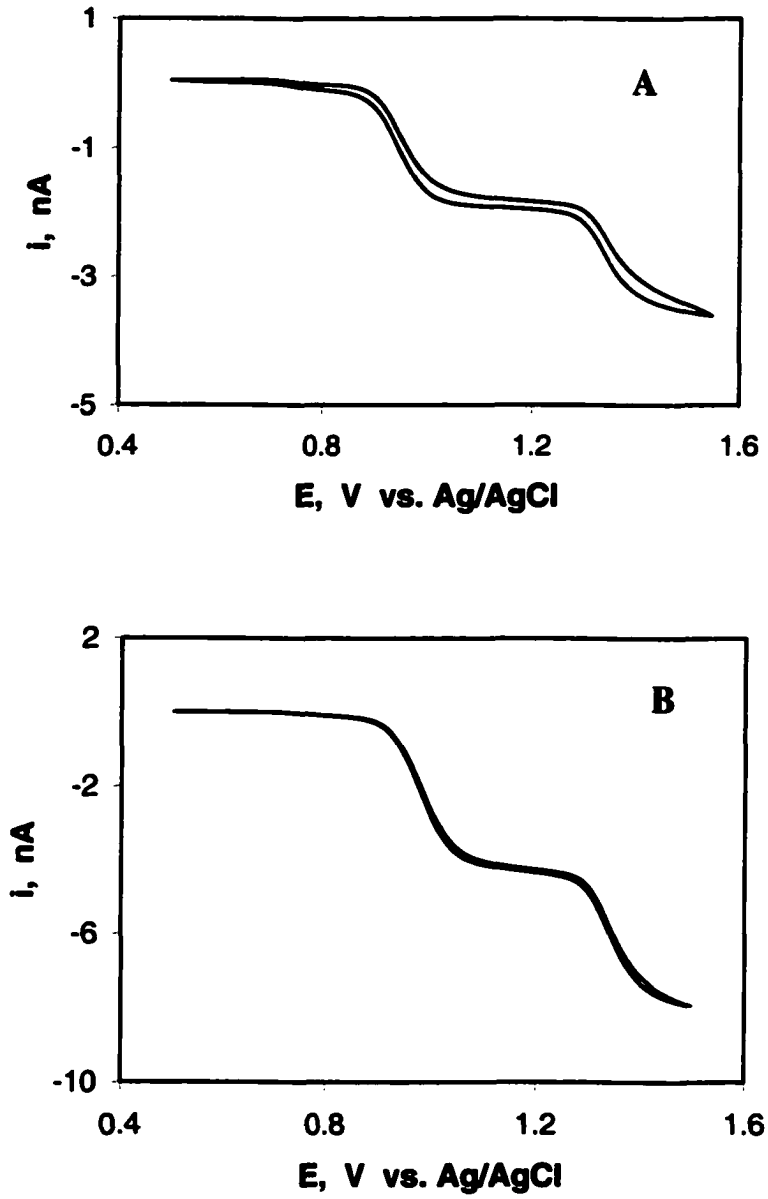

Fig. 2.1 Steady-state voltammograms of 2 mM ZnPor at a 25-μm diameter Pt disk electrode in (A) NB and (B) DCE containing 25 mM $TBAPF_6$. Scan rate was 5 mV/s.

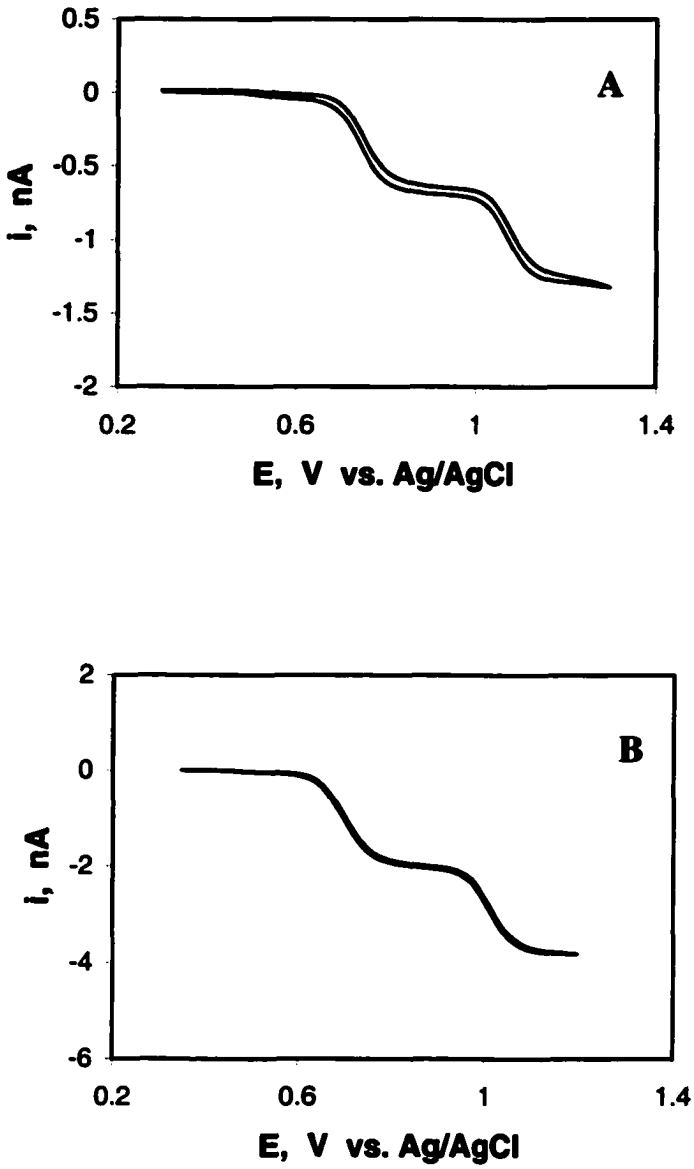

Fig. 2.2 Steady-state voltammograms of 2 mM ZnPor at a 10-μm diameter Pt disk electrode in (A) NB and (B) DCE containing 50 mM $THACIO_4$. Scan rate was 20 mV/s.

2.2.3 SECM Apparatus and Procedure

The schematic diagram of SECM instrument used in this work is shown in Fig. 2.3. Before SECM measurements, the tip electrode was positioned in the top phase. The tip was biased either at a potential corresponding to the plateau current of $Ru(CN)_6^{4-}$ oxidation in water or to the plateau current of the first oxidation wave of ZnPor in organic phase.

The approach curves were obtained by moving the tip toward the liquid/liquid interface and recording the tip current (i_T) as a function of the tip/ITIES separation distance (d). The coordinate of the liquid/liquid interface ($d = 0$) was determined from the sharp change in i_T that occurred when the tip touched the ITIES.

The concentration of ZnPor in organic phase ($\leq$ 5 mM) was limited by its solubility. When an organic solvent was used as a bottom phase, the concentration of aqueous redox species was not higher than $[ZnPor]_o/20$ to avoid diffusion limitations in the bottom layer (3-5,22,35). Here, $[ZnPor]_o$ represents the concentration of ZnPor in the organic phase.

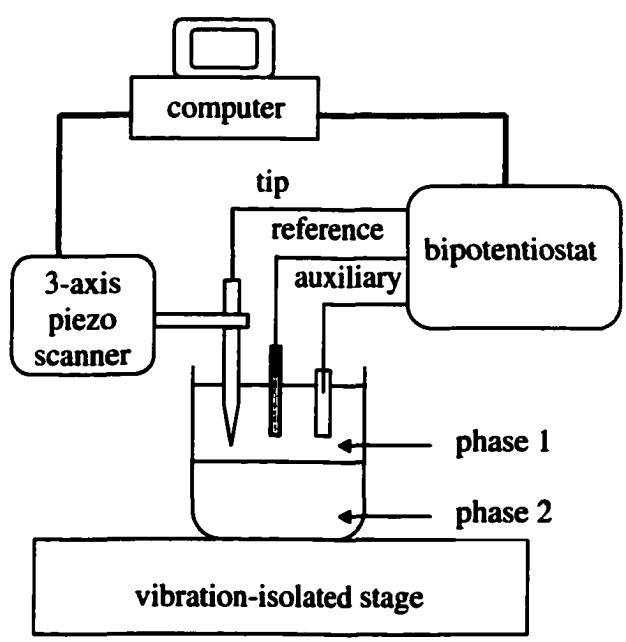

Fig. 2.3 Block diagram of the instrumentation for SECM measurements at the ITIES.

2.2.4 Potential Drop across the ITIES

In SECM measurements, the interfacial potential drop across a nonpolarizable ITIES ($\Delta_w^o \phi$) is governed by the ratio of common ion (i.e., ClO_4^- or TBA^+) concentration in the organic and aqueous phases:

$$\Delta_w^o\phi = \Delta_w^o\phi^0_{ClO_4^-} - 0.059 \log \frac{[ClO_4^-]_w}{[ClO_4^-]_o} \qquad (2.4)$$

$$\Delta_w^o\phi = \Delta_w^o\phi^0_{TBA^+} + 0.059 \log \frac{[TBA^+]_w}{[TBA^+]_O} \qquad (2.5)$$

The $\Delta_W^O \phi$ value was varied either by changing the concentration of the common ion in water (i.e., $[ClO_4^-]_w$ or $[TBA^+]_w$) at a constant concentration of that ion in organic phase (typically, 10 - 100 mM), or vice versa, the common ion concentration was changed in the organic phase and kept constant in the aqueous phase.

The driving force for ET reaction was expressed as $\Delta E^\circ + \Delta_W^O \phi$, which approximately equals to the difference of two reversible half-wave potentials obtained from the steady-state voltammograms of organic and aqueous redox species (with respect to the same Ag/AgCl reference electrode) (3-5,35).

2.3 Results and Discussion

2.3.1 Concentration dependencies of $\Delta_W^O \phi$

Although $\Delta_W^O \phi$ could not be found without an extrathermodynamic assumption, the relative values of $\Delta_W^O \phi$ can be obtained from cyclic voltammograms of either ZnPor (Fig. 2.1, 2.2) or TCNQ (Fig. 2.4) at a microdisk electrode in either NB, or DCE as described earlier (3). The reversible half-wave potential of either redox couple was measured with respect to the Ag/AgCl electrode connected to the organic solution by an ionic bridge. The cell 2.1 and 2.2 were used to measure the potential drop across the ITIES with ClO_4^- as the common ion:

Ag/AgCl/H_2O, 3 M KCl/ H_2O, 0.1 M NaCl, 0.01 – 1.0 M $NaClO_4$//organic solvent, 50 mM $THAClO_4$, 2 mM ZnPor/Pt Cell 2.1

Ag/AgCl/ H_2O, 3 M KCl/ H_2O, 0.1 M NaCl, 0.1 M $NaClO_4$//organic solvent, 1 -100 Mm $THAClO_4$, 2 mM TCNQ/Pt Cell 2.2

The organic solvent used in cell 2.1 or 2.2 was either DCE or NB.

In cell 2.1, $[ClO_4^-]_o$ was maintained constant. Thus, $\Delta_W^o \phi$ was governed by $[ClO_4^-]_w$. In cell 2.2, $[ClO_4^-]_w$ was maintained constant, and $\Delta_W^o \phi$ was governed by $[ClO_4^-]_o$. From Eq. 2.4, the slope values for the concentration dependencies of $\Delta_W^o \phi$ should be a constant of 59 mV/decade. Accordingly, the half-wave potential of any redox couple in the organic phase, measured with respect to the aqueous reference electrode, should shift by 59 mV to more negative (positive) with a decade increase in $[ClO_4^-]_w$ ($[ClO_4^-]_o$).

The measured dependence of half-wave potentials of ZnPor or TCNQ in NB or DCE on the concentration of ClO_4^- in water or organic phase is shown in Fig. 2.5.

By replacing $NaClO_4$ and $THAClO_4$ in cell 2.1 and 2.2 with TBACl and $TBAPF_6$ respectively, the cells can be used to measure the potential drop across the ITIES with TBA^+ as the common ion. The concentration dependence of half-wave potentials of ZnPor with TBA^+ as the common ion is shown in Fig. 2.6.

The experimentally determined slope values are summarized in Table 2.1. In all cases, the $\Delta_W^o \phi$ vs. log[common ion] dependence was linear with high correlation coefficients (>0.99). As discussed previously (36), ZnPor is not suitable for measuring $\Delta_W^o \phi$ vs. log $[ClO_4^-]_o$ relationship. Very small S values are obtained in such experiments because of extensive ion pairing between ClO_4^- and a cationic form of redox species. In contrast, using TCNQ as a redox probe, the slope values close to 59 mV/decade were

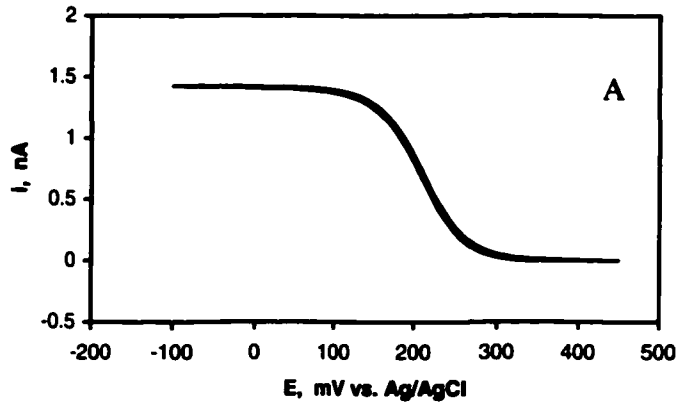

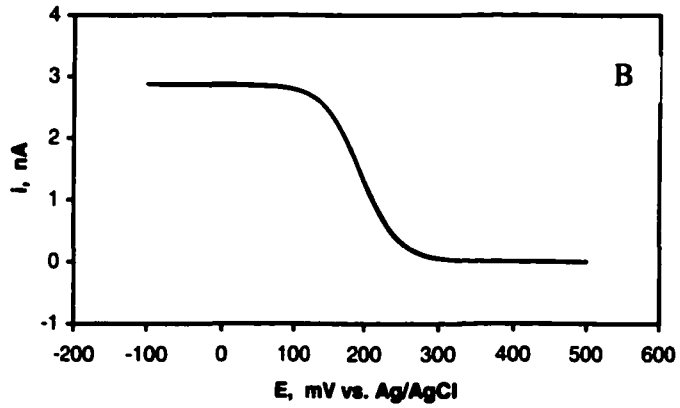

Fig. 2.4 Steady-state voltammograms of 2 mM TCNQ at a 10-μm diameter Pt disk electrode in (A) NB and (B) DCE containing 0.1 M THAP. Scan rate was 10 mV/s.

obtained for both DCE and NB (Table 2.1). The almost Nernstian slope values obtained by varying the common ion concentration in either aqueous or organic solution indicate that ion pairing of supporting electrolyte in either phase does not affect the interfacial potential drop.

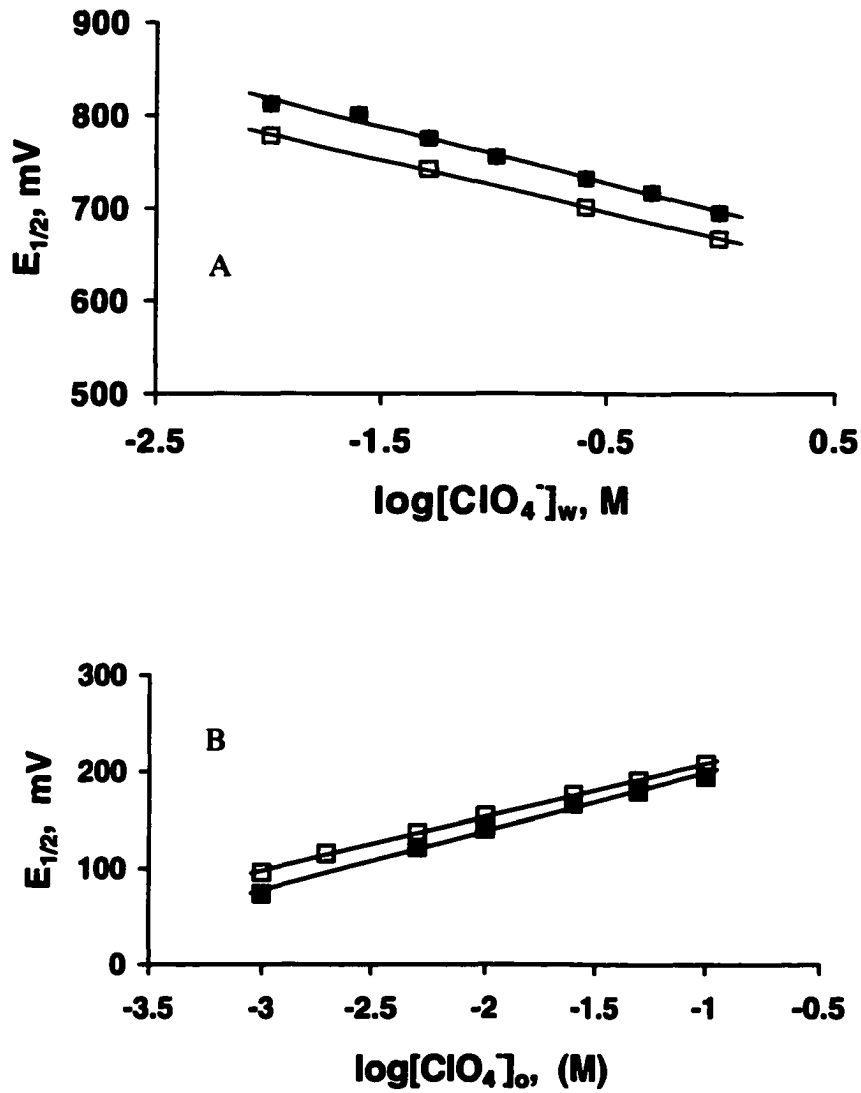

Fig. 2.5 Dependence of the half-wave potentials for the oxidation of ZnPor (A) and reduction of TCNQ (B) in DCE (■) or NB (□) on $[ClO_4^-]_w$ or $[ClO_4^-]_o$. The compositions of both aqueous and organic phase are shown in Cell 2.1 and Cell 2.2.

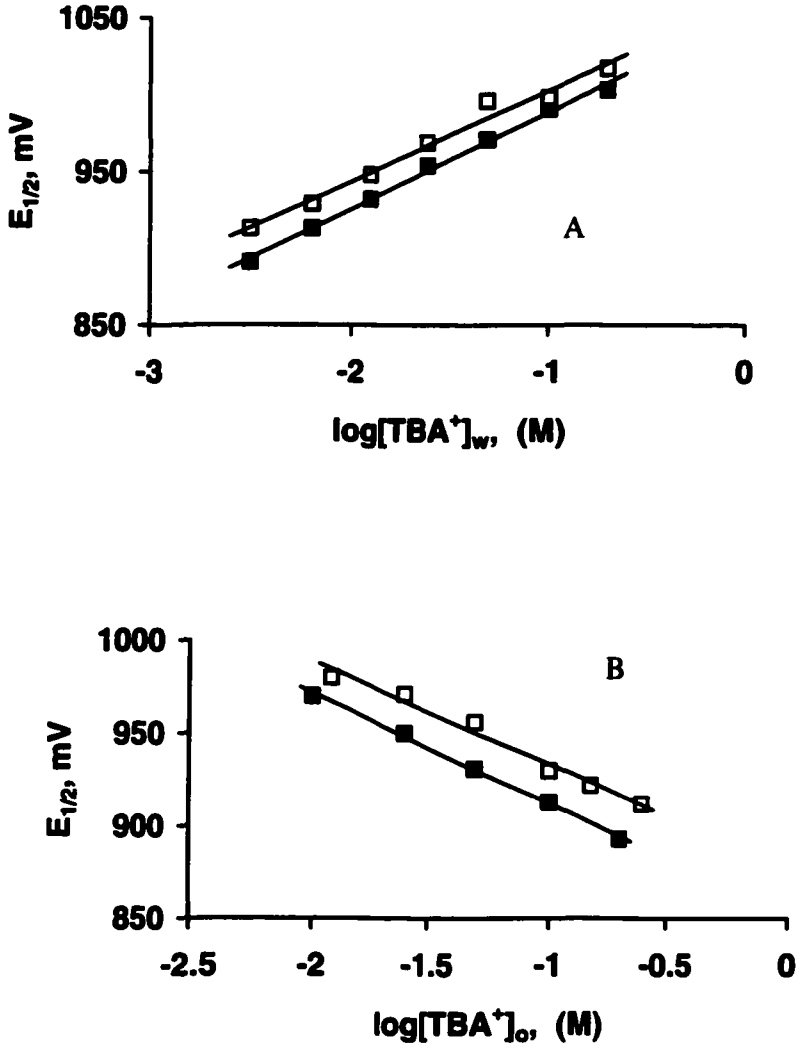

Fig. 2.6 Dependence of the half-wave potential for the oxidation of ZnPor in DCE (■) or NB (□) on [TBA^+]$_w$ (A) or [TBA^+]$_o$ (B). The organic phase contained 50 mM TBACl in (A); The aqueous phase contained 10 mM $TBAPF_6$ in (B).

Table 2.1 Slope values (S) for the concentration dependencies of $\Delta_W^O \phi$ measured at the DCE/water and NB/water interfaces.

Concentration varied	Organic solvent	S, mV/decade
$[ClO_4^-]_w$	DCE	60
$[ClO_4^-]_o$	DCE	60
$[ClO_4^-]_w$	NB	56
$[ClO_4^-]_o$	NB	55
$[TBA^+]_w$	DCE	63
$[TBA^+]_o$	DCE	55
$[TBA^+]_w$	NB	60
$[TBA^+]_o$	NB	59

2.3.2 Effects of $\Delta_W^O \phi$ and ΔE° on the Interfacial ET Rate

We first investigated the potential dependence of the rate constant of reaction 2.3b. The schematic diagram of SECM measurements of the kinetics of reaction 2.3b is shown in Fig. 2.8.

Typical approach curves are shown in Fig. 2.8 from which the rate constant of the ET reaction can be extracted.

As discussed in section 2.1, Schmickler's model predicts that the rate of the reaction 2.3b is practically independent of $\Delta_W^O \phi$ since the diffuse layer effect (concentration polarization) is negligible in this reaction system. On the other hand, if the Butler-Volmer model is operating, the k_b should increase exponentially when the organic phase is made more negative.

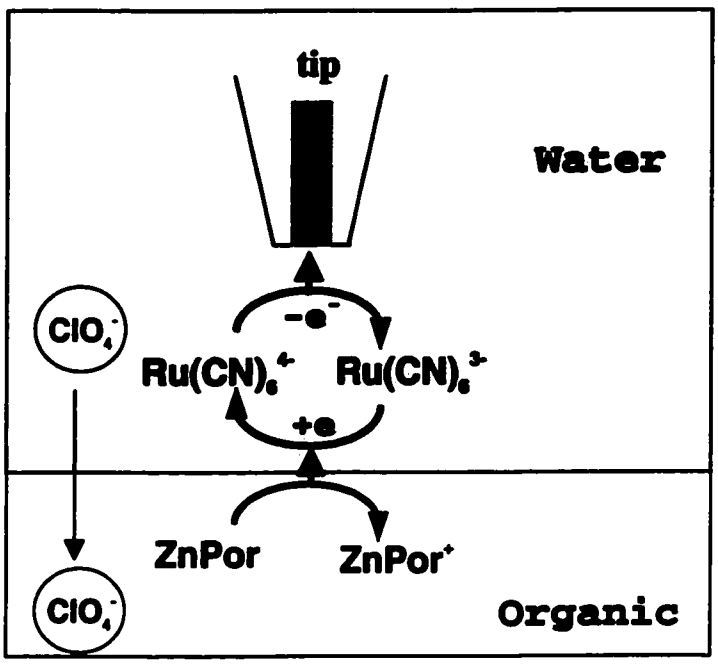

Fig. 2.7 Schematic diagram of SECM measurements of the kinetics of ET between ZnPor in organic phase and $Ru(CN)_6^{3-}$ in aqueous phase.

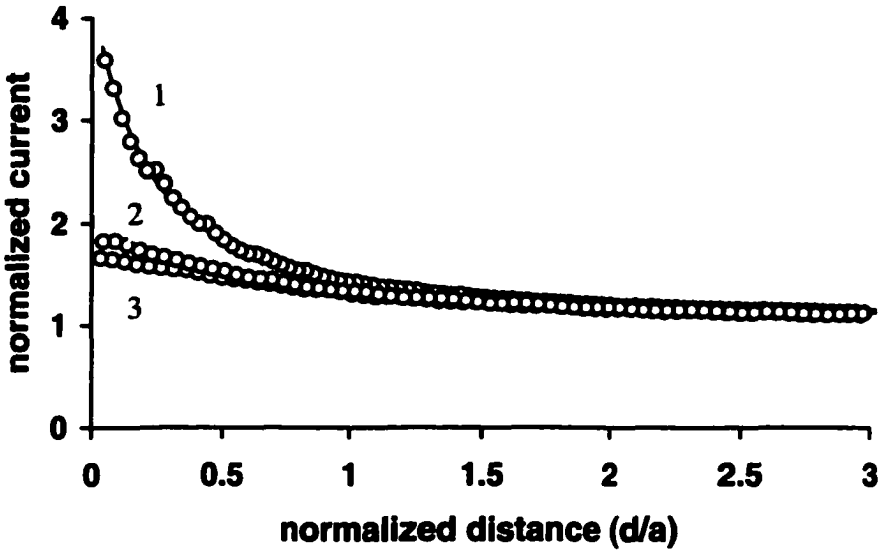

Fig. 2.8 SCEM current-distance curves for a 12.5-μm-radius Pt tip in the top aqueous phase approaching the ITIES. The bottom phase was either DCE (1) or NB (2) or benzene (3). The aqueous phase contained 0.1 mM $NaRu(CN)_6$, 0.1 M NaCl, and 50 mM $NaClO_4$. The organic phase contained 2 mM ZnPor and 50 mM $THAClO_4$; The tip was biased at a potential corresponding to the plateau current of the oxidation wave of $Ru(CN)_6^{4-}$ (0.8 V vs Ag/AgCl).The tip was scanned at 1 μm/s. (o) experimental points; (–) theoretical curves.

An experimental $\ln k_b$ vs. $\Delta_W^O \phi$ dependence obtained for reaction 2.3b at the BZ/water interface (curve 1 in Figure 2.9) fully confirms the prediction of the Schmickler's model. The k_b remained essentially constant within the limit of experimental error when the $\Delta_W^O \phi$ was changed by about 120 mV. In contrast, the rate of the reverse reaction 2.1b increased more than 10 times over the same potential range (curve 2 in Figure 2.9 (3,4)). Both plots can be extrapolated to zero driving force ($\Delta E^\circ + \Delta_W^O \phi$) at which k_b and k_f should be equal in the absence of the double layer effect. The actual k_b/k_f ratio (~ 20) represents the magnitude of the diffuse layer effect on the ET rate constant at this potential.

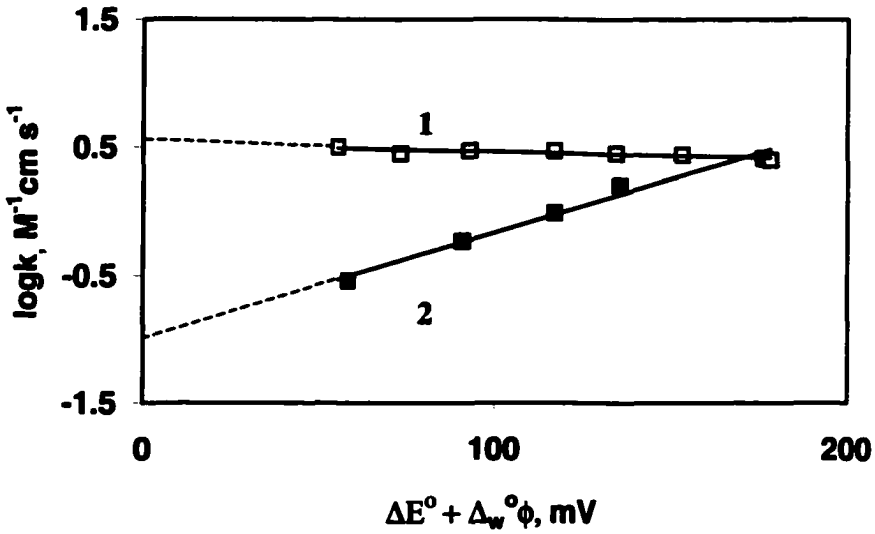

Fig. 2.9 Potential dependence of the ET rate between ZnPor in BZ and $Ru(CN)_6^{3-}$ in water (curve 1) and an analogous dependence for the reverse ET reaction (curve 2, replotted from ref 3,4). BZ contained (1) 2 mM ZnPor and 50 mM $THAClO_4$; and (2) 0.5 mM ZnPor and 0.25 M $THAClO_4$. The aqueous solution contained 0.01-2.0 M $NaClO_4$, 0.1 M NaCl and (1) 0.1 mM $Ru(CN)_6^{4-}$ or (2) 7 mM $Ru(CN)_6^{4-}$. The bimolecular rate constant, k, equals k_b/[ZnPor] for reaction 2.3b and k_f/[$Ru(CN)_6^{4-}$] for the reverse reaction 2.1b. ΔE° is the difference between standard potentials of two redox couples.

While k_b is virtually independent of $\Delta_w^o \phi$ it is expected to be a function of ΔE° similarly to rate constants of homogeneous ET reactions (9-11). Since the opposite observation was reported recently (37), we checked the dependence of the k_b on $\Delta_w^o \phi$ by replacing $Ru(CN)_6^{4-}$ with $Fe(CN)_6^{4-}$. Because the formal potential of the $Fe(CN)_6^{3/4-}$ couple is ~ 500 mV less positive, the replacement should result in about 4 orders of magnitude decrease in k. Accordingly, the interfacial reaction between ZnPor and $Fe(CN)_6^{3-}$ was immeasurably slow under our experimental conditions.

Attributing the Butler-Volmer-type dependence of k vs $\Delta_w^o \phi$ for ET involving charged organic redox species (3) to the diffuse layer effect may be surprising because of the very small dielectric constant of BZ (~ 2.2). Under these conditions most $ZnPor^+$ species should be ion paired. However, this may not be so in the interfacial region. A recent work by Eisenthal and co-workers (38) showed that the polarity of the liquid/liquid interface is the arithmetic average of the polarities of two immiscible solvents. Thus, the BZ/water interface is much more polar than the bulk BZ, and the extent of ion pairing at the phase boundary should be significantly smaller. The observed dependence of the rate constant on $\Delta_w^o \phi$ reflects the work of bringing the charged reactant species to the interface (w_p), according to (14)

$$k_{obs} = Z \exp\left(-\frac{w_p}{RT}\right) k_{et} \qquad (2.6)$$

where k_{obs} is the observed rate constant, Z is the preexponential factor, and k_{et} is the first-order rate constant of the ET reaction within the precursor formed at the interface.

In contrast, the observation of the Marcus inverted region for long-range ET across a phospholipid monolayer (4) suggests the true potential dependence of the rate constant. The difference is that the long-chain lipid molecules prevented ZnPor from coming very close to the phase boundary, and therefore interfacial potential dropped mostly between redox reactants.

In previously reported SECM experiments (3-5), it was possible (albeit unlikely) that $ZnPor^+$ species produced at the tip was transferred into the aqueous solution in which ET occurred via a homogeneous bimolecular reaction. The apparent potential dependence of the rate constant in this case would represent ion transfer rather than ET reaction. Such a complication is excluded in the present work since the organic reactant (ZnPor) is a neutral species practically insoluble in water.

2.3.3 Solvent Effect on the ET Rate

To investigate the effects of organic solvent on interfacial ET the k_b vs $\Delta_W^O \phi$ dependencies were obtained in BZ, NB, and DCE (Figure 2.10). For each of these solvents k_b is almost potential-independent. The slope of each k_b vs $\Delta_W^O \phi$ curve reflects the competition between the concentration effect in water (i.e., depletion of $Ru(CN)_6^{3-}$ at the ITIES at higher [$NaClO_4$] corresponding to more negative $\Delta_W^O \phi$) and change in driving force for ET produced by a small fraction of interfacial voltage dropping within the mixed layer. A very small negative slope for BZ/water interface indicates that diffuse layer effect in the aqueous phase in this case is very weak. This is not surprising because almost all $\Delta_W^O \phi$ drops in BZ diffuse layer (for more polar DCE this fraction is about 95% (7); for less polar BZ this fraction should be even larger) (14,17). With more polar DCE, the concentration effect in the aqueous phase is strong enough to counterbalance minor decrease in ET rate constant caused by a slightly smaller driving force at more positive $\Delta_W^O \phi$. Hence a virtually zero slope of the k_b vs $\Delta_W^O \phi$ curve. The diffuse layer effect on the aqueous side of the NB/water interface predominates and results in a small positive slope of the potential dependence.

The nature of organic solvent can affect the value of the ET standard rate constant at the ITIES in two ways: (i) through the Pekar factor, $1/\varepsilon_{op} - 1/\varepsilon_s$, where ε_{op} and ε_s are the optical and static dielectric constants of organic phase; and (ii) through longitudinal solvent relaxation time, τ_L. Solvent effects have previously been reported for homogeneous and electrochemical ET reactions (39,40) but not for ET at the ITIES. The Pekar factor values are similar for NB and DCE (41) (Table 2.2). In contrast, the relaxation time for DCE is significantly smaller (Table 2.2) and the measured rate constant is about three times higher, as can be expected from the theory (9-11,39,40). A direct comparison of this results to those obtained in BZ is difficult because for the latter solvent ε_{op} and ε_s are similar and no relaxation data is available.

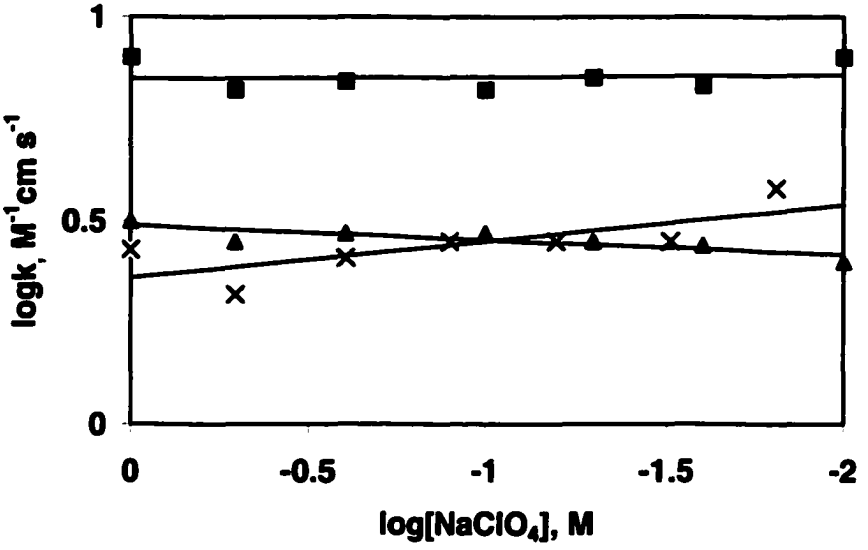

Fig. 2.10 Solvent effect on the ET rate constant. The ET rate constants ($k = k_b$/[ZnPor] for the reaction 2.3b) were measured at the interface between aqueous solution and BZ (▲), NB (×), and DCE (■). See Figure 2.10, curve 1 for compositions of the aqueous and organic phases. $\Delta_W^O \phi$ is expressed in terms of log $[ClO_4^-]_w$.

Table 2.2 Optical (ε_{op}) and Static (ε_s) Dielectric Constants and Longitudinal Relaxation Times (τ_L) of NB and DCE (41)

Solvent	ε_{op}	ε_s	$1/\varepsilon_{op} - 1/\varepsilon_s$	τ_L, ps
NB	2.40	34.8	0.388	5.3
DCE	2.08	10.4	0.385	1.6

2.3.4. Effect of the common ion adsorption

The adsorption of ZnPor at the ITIES recently observed by Girault's group (42) can be the other reason for the potential-independent rate of ZnPor oxidation. To check this hypothesis, we probed the kinetics of reaction 2.3b with TBA^+ used as a surface active common ion (Figure 2.11). Reid et al. (43) observed rapid decrease in surface tension at the liquid/liquid interface with increasing concentration of TBA^+ in aqueous phase. More recently, the adsorption of TBA^+ at the water/NB interface from aqueous bromide

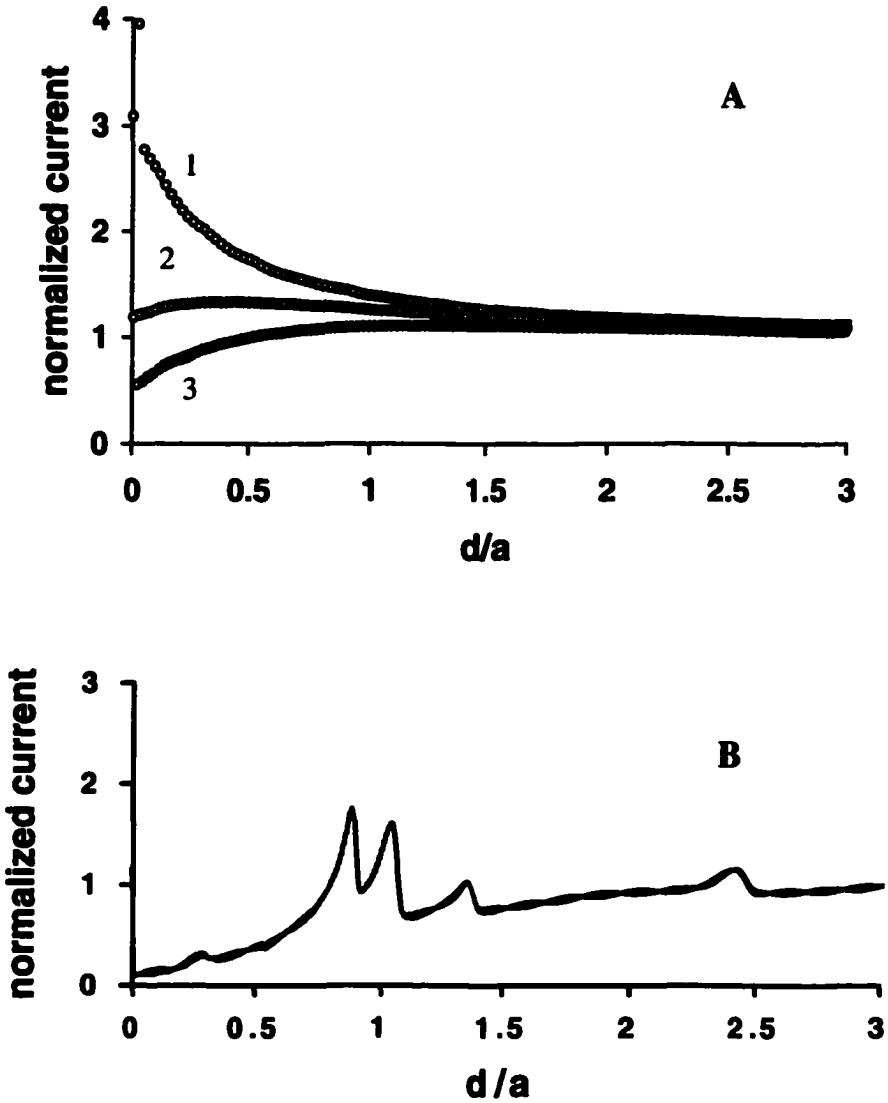

Fig. 2.11 Current – distance curves for a 12.5-μm-radius Pt tip approaching water/DCE interface. (A) Aqueous phase contained 0.1 mM $Na_4Ru(CN)_6$, 0.1 M NaCl, and 3.1 (1), 12.5 (2), and 50 (3) mM TBACl. DCE was 2 mM in ZnPor and 50 mM in $TBAPF_6$. Symbols – experimental data; solid lines – theory. (B) Current oscillations caused by the film formation at [TBACl] = 100 mM.

and chloride solutions was reported by Uchiyama et al (44). In our experiments, at lower concentrations of TBA^+ in water (e.g., $[TBA^+]_w < 25$ mM), the interface formed a meniscus in the glass cell (i.e., the organic phase is convex), but at higher concentrations, the interface became flat. Moreover, at high $[TBA^+]_w$ (i.e., > 0.1 M for DCE/water and > 0.2 M for NB/water), a film forms at the interface. Although the film could not be seen by the naked eye, the appearance of abnormal peaks on the current-distance curves (Figure 2.11B) points to the multi-layer film formation at the ITIES (3). In contrast, perchlorate is not strongly adsorbed at the ITIES. Zhang et al. showed recently that the adsorption of ClO_4^- (if any) does not significantly affect the kinetics of interfacial ET (36).

The SECM approach curves obtained at different concentrations of TBA^+ in the aqueous phase (Figure 2.11A) show the lower tip current at higher $[TBA^+]_w$. The apparent heterogeneous rate constants (k_b) of reaction 2.3b at the DCE/water interface extracted from the approach curves using previously developed SECM theory (5) exhibit strong dependence on $[TBA^+]_w$ (Figure 2.12A). The apparent transfer coefficient (α) extracted from this plot is 0.56. Similar result was obtained by Zhang et al. in their experimental studies of ET between $Fe(CN)_6^{3-}$ in water and decamethyl ferrocene in DCE (36). The ET rate constant were found to depend strongly on the interfacial potential drop, with an apparent transfer coefficient of 0.38 when TBA^+ was used as the common ion.

The TBA^+ adsorption at the NB/water interface was less pronounced at $[TBA^+]_w < 50$ mM (the interfacial shape did not change greatly when the TBA^+ concentration was < 50 mM). Accordingly, the log k_b vs. $[TBA^+]_w$ dependence in this concentration range was relatively weak ($\alpha = 0.1$). However, the k_b value decreased markedly at higher $[TBA^+]_w$ (Figure 2.12B).

These findings are in a sharp contrast with the results of our previous experiments, in which the k_b of reaction 2.3b was independent of $[ClO_4^-]_w$ when perchlorate was used as a common ion. Since neither perchlorate nor TBA^+ is expected to strongly interact with redox reactants, the major difference between k_b vs. $\Delta_w^o \phi$ dependences observed with those common ions is likely to be due to adsorption of TBA^+ at the interface. The adsorbed TBA^+ species can displace ZnPor from the interfacial region, thus increasing the

distance between the redox reactants and decreasing the ET rate. The specific adsorption of the bulky TBA^+ (3.85 Å radius) at the ITIES should result in a thicker mixed solvent layer (45). This effect may also contribute to the increase in the distance between the aqueous and organic reactants. The larger separation distance in turn increases the fraction of the interfacial voltage dropping between the aqueous and organic reactants, so that the true dependence of the k_b on $\Delta_w^o \phi$ (i.e., Butler-Volmer kinetics) should appear when TBA^+ is used as a common ion. Thus, the decrease in the k_b with increasing $[TBA^+]_w$ can be caused by two concomitant and interrelated effects – the increasing separation between redox species and the decreasing driving force of ET (the increase in $[TBA^+]_w$ shifts $\Delta_w^o \phi$ to more positive values). These two factors can be separated by probing the dependence of the rate constant on $[TBA^+]_o$.

2.3.5. Effect of common ion concentration in organic phase

In previous SECM experiments (3-5,22,35,36,46-48), the concentration of the common ion in organic solvent was kept constant to avoid complications, which might be caused by changes in the diffuse layer thickness and the extent of ion pairing. As shown in Table 2.1, $\Delta_w^o \phi$ dependences on $[TBA^+]_o$ and $[ClO_4^-]_o$ are essentially Nernstian for both DCE/water and NB/water interfaces. Two $\log k_b$ vs. $\log[TBA^+]_o$ dependencies obtained for reaction 2.3b at the water/DCE interface at $[TBA^+]_w$ = 10 mM (curve 1) and $[TBA^+]_w$ = 50 mM (curve 2) are shown in Figure 2.13A. While at a lower $[TBA^+]_w$ value the ET rate is independent of $[TBA^+]_o$ ($\alpha = 0.0$), at $[TBA^+]_w$ = 50 mM the linear $\log k_b$ vs. $\log[TBA^+]_o$ dependence can be seen ($\alpha = 0.21$). At NB/water interface (Figure 2.13B), the picture is even more clear – the apparent α value changes from 0.03 at $[TBA^+]_w$ = 10 mM (curve 1) to 0.34 at $[TBA^+]_w$ = 50 mM (curve 2) and to 0.58 at $[TBA^+]_w$ = 100 mM (curve 3).

Kakiuchi's treatment of ionic adsorption at the ITIES (49) is useful for understanding of these results. According to that model, at any given $\Delta_w^o \phi$ the adsorption of a common ion occurs either from organic or from the aqueous side of the interface. Furthermore, the model predicts that at a given $\Delta_w^o \phi$ if the adsorption of an ion from aqueous side is favorable, the adsorption of the ion from organic side will be

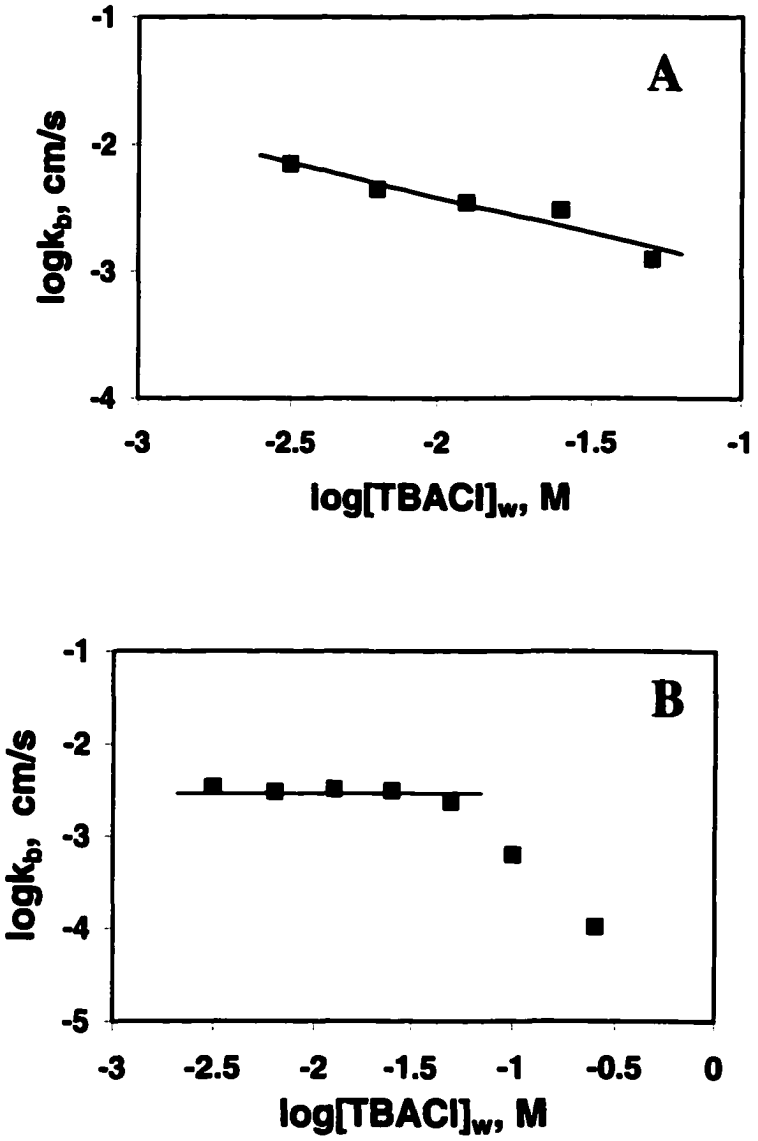

Fig. 2.12 Dependence of the rate of ET between ZnPor and $Ru(CN)_6^{3-}$ on TBACl concentration in aqueous phase. In addition to TBACl, aqueous solution contained 0.1 mM $Na_4Ru(CN)_6$ and 0.1 M NaCl. The organic phase was DCE (A) or NB (B) containing 2 mM ZnPor and 50 mM $TBAPF_6$.

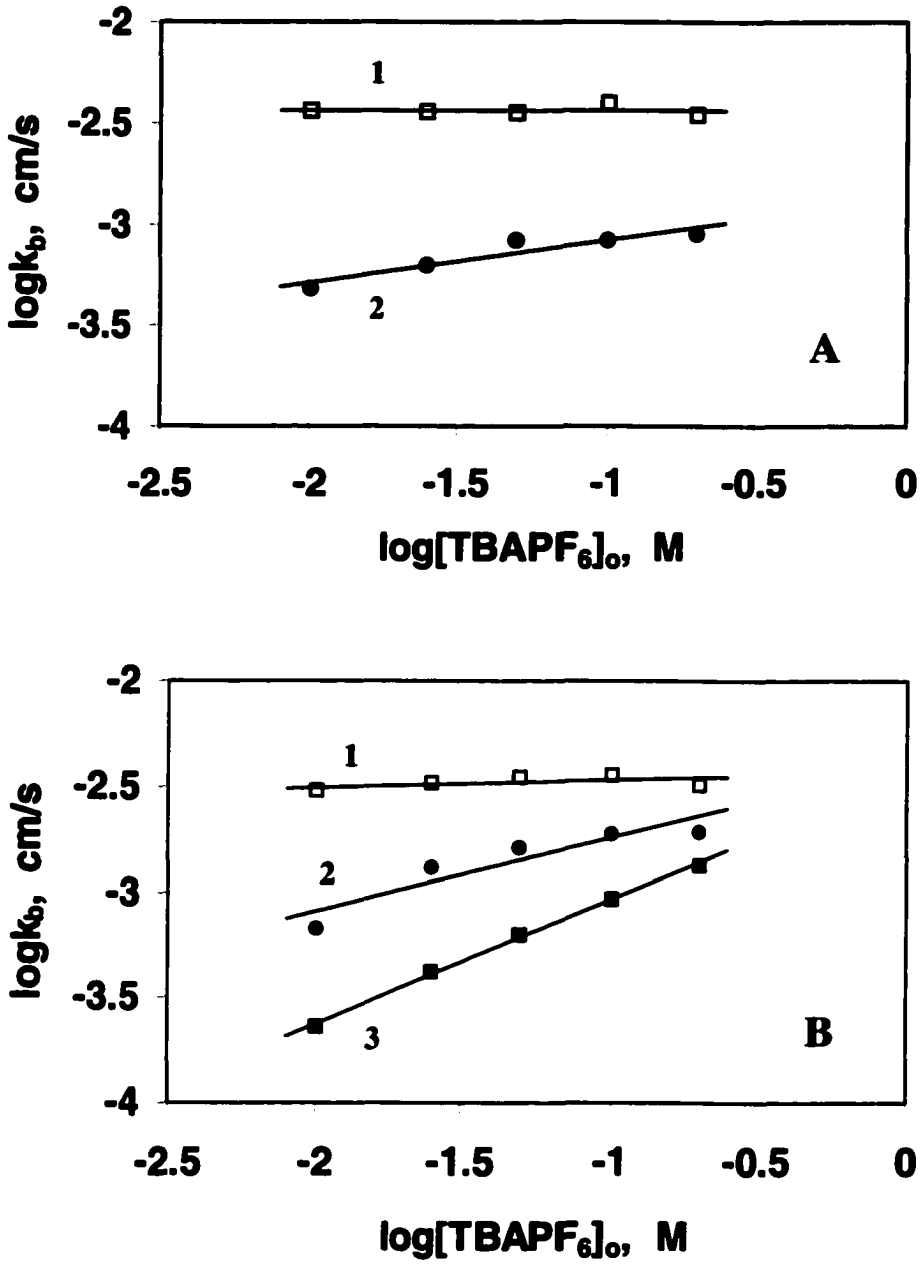

Fig. 2.13 Dependence of the rate of ET between ZnPor and $Ru(CN)_6^{3-}$ on $TBAPF_6$ concentration in organic phase. The organic phase was DCE (A) or NB (B) containing 2 mM ZnPor. The aqueous phase contained 0.1 mM $Na_4Ru(CN)_6$, 0.1 M NaCl and 10 mM (curve 1), 50 mM (curve 2), or 100 mM (curve 3) TBACl.

unfavorable. Because in our experiments the interfacial voltage was varied within a narrow range (~100

mV), and the experimental results showed in the last section indicate strong adsorption of TBA^+ from aqueous phase, one can expect that the adsorption of TBA^+ from organic phase is weak. This assumption is supported by essentially same shape of the interfacial meniscus observed for wide range of $[TBA^+]_o$, between 10 and 200 mM, and by the absence of a multilayer interfacial film at high $[TBA^+]_o$ Thus, at low concentrations of TBA^+ in water, its surface concentration is also low, and ZnPor remains adsorbed on the ITIES. Under these conditions, the ET rate constant is essentially potential-independent (curve 1 in Figs. 2.13A and 2.13B). At higher $[TBA^+]_w$, ZnPor gets displaced from the interface, and the rate constant of reaction 2.3b depends strongly on $[TBA^+]_o$ (curves 2 and 3 in Fig. 2.13).

One should notice that the k_b values in Fig. 2.13 increase with increasing $[TBA^+]_o$. Unlike the k_b vs. $[TBA^+]_w$ dependences in Fig. 2.12, which represent the combination of the effects of ZnPor desorption and the true potential dependence of the ET rate, the k_b vs. $[TBA^+]_o$ dependences reflect only the true potential dependence of the ET rate (the increase in $[TBA^+]_o$ shifts $\Delta_w^o \phi$ to more negative values, thus leads to a increasing driving force of ET). The increase in the apparent α value with $[TBA^+]_w$ can be explained by increasing fraction of the overall interfacial voltage dropping between ZnPor and $Ru(CN)_6^{3-}$ species. The diffuse double layer effect in water cannot be responsible for the observed increase in ET rate with $[TBA^+]_o$ because the increase in $[TBA^+]_o$ shifts $\Delta_w^o \phi$ to more negative values and causes the depletion (rather than accumulation) of negatively charged $Ru(CN)_6^{3-}$ at the interface.

Changing the electrolyte concentration in organic solution could affect the interfacial ET rate in different ways. The ion pairing effect discussed recently by Quinn and Kontturi (50) is less important in our system because the organic reactant (ZnPor) is a neutral species. To check the possibility that the observed potential dependence of ET rate is caused by diffuse layer effect in organic phase (51), the $\log k_b$ vs. $\log[ClO_4^-]_o$ dependences were obtained using perchlorate as a common ion (Figure 2.14). Very small a values (i.e., 0.05 at the DCE/water and 0.07 at the NB water interface) extracted from Fig. 2.14 indicate the organic diffuse layer effect on the rate of reaction (2.3b) is negligibly small.

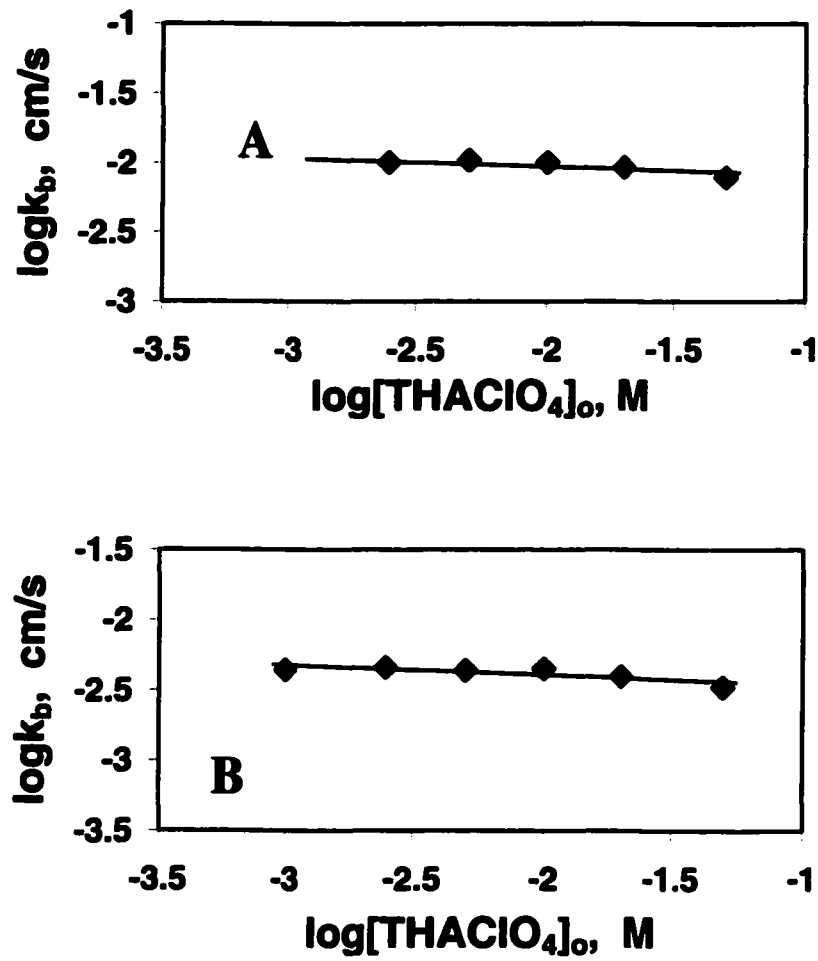

Fig. 2.14 Dependence of the rate of ET between ZnPor and $Ru(CN)_6^{3-}$ on $THACIO_4$ concentration in organic phase. The organic phase was DCE (A) or NB (B) containing 2 mM ZnPor. The aqueous phase contained 0.1 mM $Na_4Ru(CN)_6$, 0.1 M NaCl and 100 mM $NaClO_4$.

2.3.6. Long-distance ET across phosphatidyl serine monolayers

Similarly to the previous experiments with phosphatidyl choline (PC) lipids (4), the formation of a molecular monolayer of a long-chain phosphatidyl serine (PS) lipid impeded ET across the liquid/liquid interface. After the addition of a lipid stock solution to the organic phase, the measured rate constant decreased rapidly and within 15 – 20 min reached the limiting value (corresponding to a specific concentration of lipid in organic phase). The diffusion-controlled adsorption of PS is slightly faster than PC adsorption, which required 30–40 min to come to equilibrium (4).

In this work, SECM was employed to probe ET reactions between $Ru(CN)_6^{4-}$ or $Fe(CN)_6^{4-}$ in water and $ZnPor^+$ in benzene (reaction 2.1b) at the ITIES modified by a monolayer of PS (Figure 2.15).

Several dependences of ET rate constant (k_f) vs. lipid concentration obtained for the two different aqueous redox species and three different lipids C-10, C-12, and C-16 are shown in Figure 2.16. As discussed earlier (4), the decrease in ET rate with increasing lipid concentration points to the increasing fraction of the interfacial area covered with lipid. At higher concentrations of any lipid (i.e., $\geq 50\ \mu M$), the ET rate between $Ru(CN)_6^{4-}$ and $ZnPor^+$ across a complete monolayer of any lipid with a number of methylene groups, $n \geq 10$, is immeasurably slow (filled symbols in Fig. 2.6). This shows that the lipid films are sufficiently compact to make the current through defects negligibly small under our experimental conditions. For the $Ru(CN)_6^{4-}/ZnPor^+$ reaction, the effective heterogeneous rate constant can be related to the fraction of the ITIES area covered with lipid (θ) (4,52,53):

$$k_f(\theta) = (1-\theta)\, k_f(0) \qquad (2.7)$$

where $k_f(0)$ is the rate constant at the lipid-free ITIES. Thus, Fig. 2.16 essentially represents the θ vs. [lipid] dependence, which can be fit to the Langmuir isotherm, as it was shown for PC adsorption in ref. 4.

When $Ru(CN)_6^{4-}$ is replaced with $Fe(CN)_6^{4-}$ (for which ΔE° is about 0.5 V larger), the k_f decreases markedly with increasing concentration of lipid, but does not vanish at higher concentrations (open symbols in Fig. 2.16). Instead, it reaches a limiting value at about 50 μM and does not change at higher

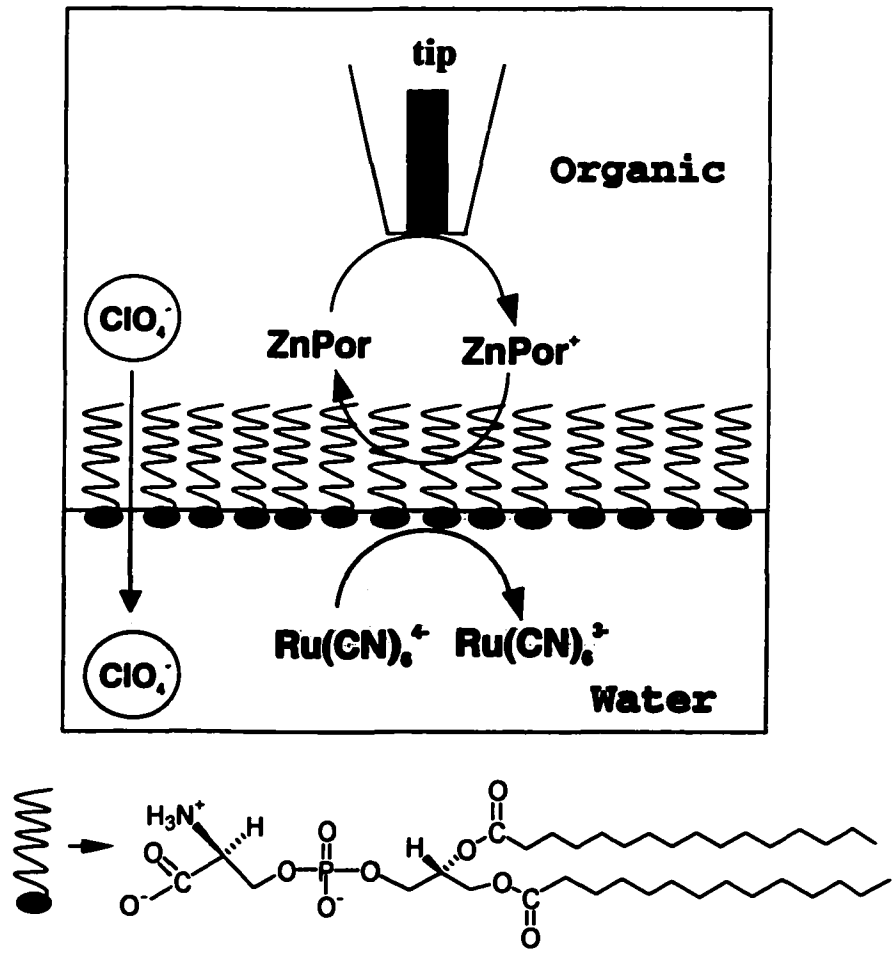

Fig. 2.15 The schematic diagram of ET across a lipid monolayer and the structure of synthetic saturated phosphatidyl serine lipid.

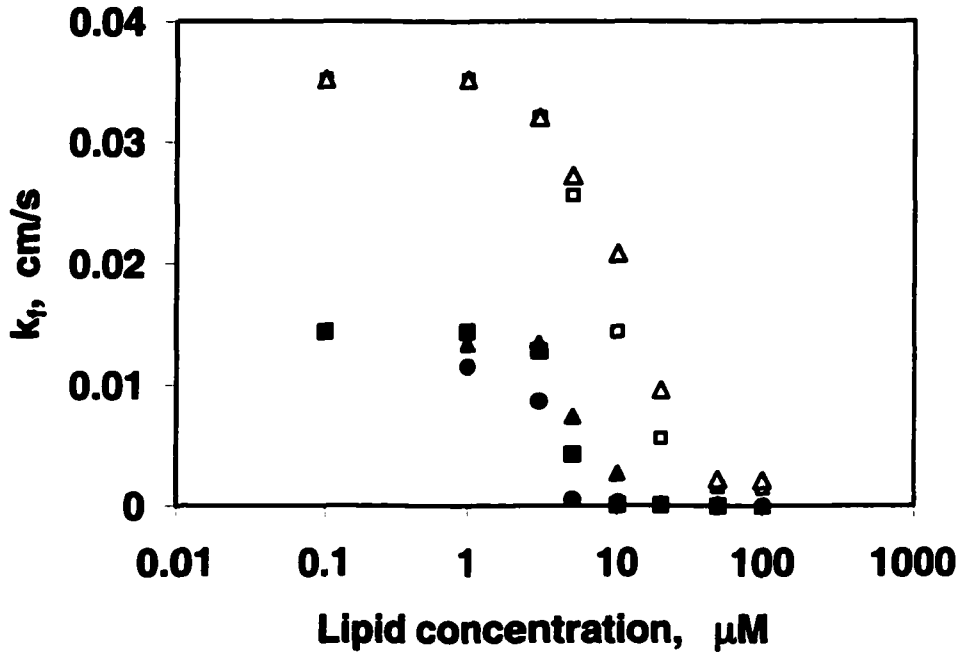

Fig. 2.16 Dependence of the rate constant of ET between $ZnPor^+$ and $Ru(CN)_6^{4-}$ (filled symbols) or $Fe(CN)_6^{4-}$ (open symbols) on lipid concentration in benzene. The number of methylene groups in the lipid hydrocarbon chain was: 10 (triangles), 12 (squares), and 16 (circles). The organic phase contained 0.25 M $THAClO_4$, 0.5 mM ZnPor, and lipid. The water phase contained 0.1 M NaCl, 0.1 M $NaClO_4$, and 7 mM $Ru(CN)_6^{4-}$ or $Fe(CN)_6^{4-}$. Rate constants were obtained by fitting experimental approach curves to the theory (5).

Table 2.3 Rate constants of long-range ET between $ZnPor^+$ and $Fe(CN)_6^{4-}$ across phosphatidyl serine (PS) and phosphatidyl choline (PC) monolayers adsorbed at the BZ/water interface

PS	$k_f \times 10^3$, cm/s	PC	$k_f \times 10^3$, cm/s (from ref. 4)
C-10	1.9	C-10	12
C-12	1.4	C-12	4.8
C-16	0.3	C-16	1.6 to 6.5

lipid concentrations. This saturation points to the formation of a complete phospholipid monolayer at the ITIES. In the same concentration range (i.e., [lipid] ≥ 20 μM), the formation of compact PS monolayers was observed previously at the water/nitrobenzene interface (31,54).

The ET between $Fe(CN)_6^{4-}$ and $ZnPor^+$ occurs at a measurable rate via tunneling through the monolayer. Kakiuchi et al (31) reported that the differential capacity of the ITIES covered with a PS monolayer was similar to that obtained with an analogous PC lipid. They concluded that at room temperature both families of lipids form liquid-expanded monolayers at the NB/water interface. Thus, similar blocking of interfacial ET by both types of lipid films can be expected. However, the rate constants of reaction 2.1b across different PS monolayers turned out to be significantly lower than the rate constants across PC spacers (with the same number of methylene groups) measured under the same experimental conditions (Table 2.3). This cannot be explained by smaller penetration of $ZnPor^+$ into the lipid phase. If PS films were less permeable to $ZnPor^+$ than PC films, a strong distance dependence of the ET rate would be observed. On the contrary, the ET rates across a C-10 and a C-12 monolayers were almost identical (Fig. 2.16), and the rate constant for C-16 was only ~5 times lower than that for C-10.

Unlike phosphatidyl cholines, which are neutral, phosphatidyl serine lipids are negatively charged at pH 7 (55). The differences in ET rates across PS and PC films can be related to the repulsion of anionic $Fe(CN)_6^{4-}$ species by negatively charged heads of the PS lipid surfactants. Such a repulsion may result in both the decreased interfacial concentration of $Fe(CN)_6^{4-}$ and the larger separation of the redox reactants. The PS films can be rendered neutral by decreasing the aqueous phase pH to <5. This should produce two opposite effects. A neutral PS film is expected to be more compact than a charged film because of lower electrostatic repulsion between lipid molecules and thus should block ET stronger. Apparently, this effect is counterbalanced by the elimination of $Fe(CN)_6^{4-}$ repulsion discussed above, and the net effect of the pH change on the ET rate is small (e.g., $k_f = 1.8 \times 10^{-3}$ cm/s at pH 4 vs. 2.2×10^{-3} cm/s at pH 6.5 for a complete C-10 monolayer under the same conditions).

The weak distance dependence of ET rate (table 2.3) may be caused by partial penetration of $ZnPor^+$ into the lipid monolayer, which prevents any quantitative analysis of the k_f vs n results in terms of distance

dependence of ET. An attempt was made to improve the blocking properties of the spacer by solidifying lipid monolayers. Liquid-expanded PS monolayers formed at the ITIES at room temperature can be converted to liquid-condensed state or even made solid by addition of a low concentration of a divalent cation (e.g., Ca^{2+} or Mg^{2+}) (31,56). Three approach curves for the $Fe(CN)_6^{4-}$ /ZnPor ET across a C-12 monolayer in the absence (1) and presence (2,3) of Ca^{2+} in the aqueous phase are presented in Figure 2.17. While the lower feedback current in the presence of calcium is expected (curve 2), the increase in i_T upon addition of calcium to the aqueous phase (curve 3) is surprising. The higher value of the effective rate constant (i.e., 0.0042 cm/s from curve 3 vs. 0.0014 cm/s from curve 1 in Fig. 2.17) points to a weaker blocking effect exerted by a solidified lipid film. This observation suggests that the addition of calcium ion results in a significantly higher defect density in the lipid film. This observation is not in conflict with low values of differential capacity of PS monolayers measured in the presence of Ca^{2+} (31). Even a small number of pinholes greatly increase the ET rate across a blocking monolayer film, while the combined area of those defects (which affects the interfacial capacitance) can be very small (28,52,53,57).

To investigate the film uniformity, the tip was scanned above the monolayer in the x-y plane parallel to the interface. (In this way micrometer-sized domains of different reactivity have previously been detected in monolayers consisting of two different lipids (35)). When the tip was scanned above the interface covered with C-10 lipid and no calcium was added to the solution, the i_T was practically constant and independent of the (x,y) position of the tip (curve 2 in Figure 2.18). The interface appears to be flat and smooth. Major fluctuations of the current appeared after the addition of 20 μM of Ca^{2+} to aqueous layer (curve 1 in Figure 2.18). Two different kinds of micrometer-sized domains can be seen in curve 1 corresponding to a lower i_T (i.e., smaller k_f value) and to a higher current response (i.e., larger k_f value) as compared to curve 2. We take the former to correspond to domains of solidified lipid monolayer that produces a stronger blocking effect on the ET reaction. Clearly, a μm-sized zone, which produces a higher feedback current, cannot be completely free of lipid (if this were the case, the $Fe(CN)_6^{4-}$ /ZnPor ET reaction at such a domain would be diffusion-controlled, and the measured feedback current would be much higher). A more plausible explanation is that the pinhole defects in the monolayer are clustered within such domains. The highest feedback current in Fig. 2.17 (curve 3) apparently corresponds to such a domain.

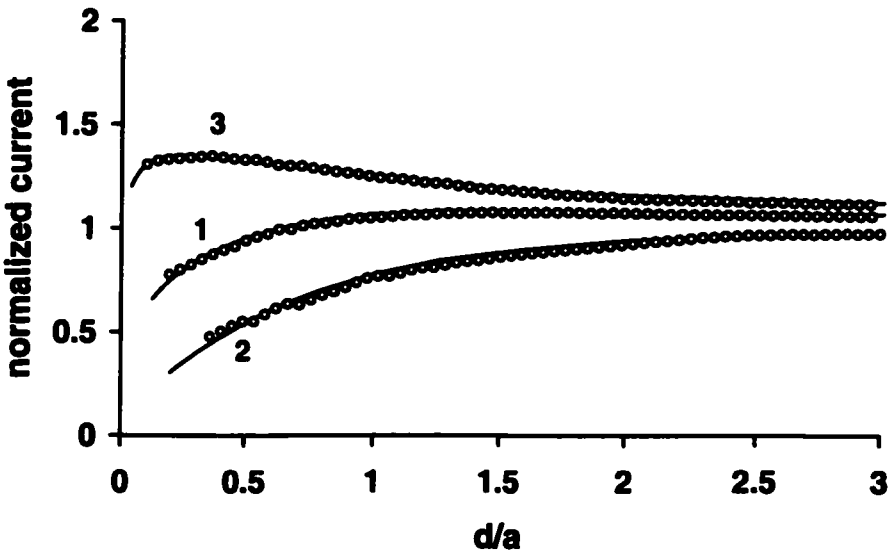

Fig. 2.17 Approach curves for a full monolayer (100 μM lipid in benzene) of C-12 in the absence (1) and presence (2,3) of Ca^{2+} in the aqueous phase. Curves 2 and 3 were obtained with a tip approaching different areas of the interface. The effective rate constant values found from the theoretical fit (solid lines) to the experimental points (symbols) were (1) 0.0014 cm/s, (2) 0.00038 cm/s, and (3) 0.0042 cm/s. The tip approached at 1 μm/s. Aqueous phase contained 7 mM $Na_4Fe(CN)_6$, 0.1 M NaCl, 0.1 M $NaClO_4$, and 20 μM $CaCl_2$ (2,3). BZ was 0.5 mM in ZnPor and 0.25 M in $THAClO_4$.

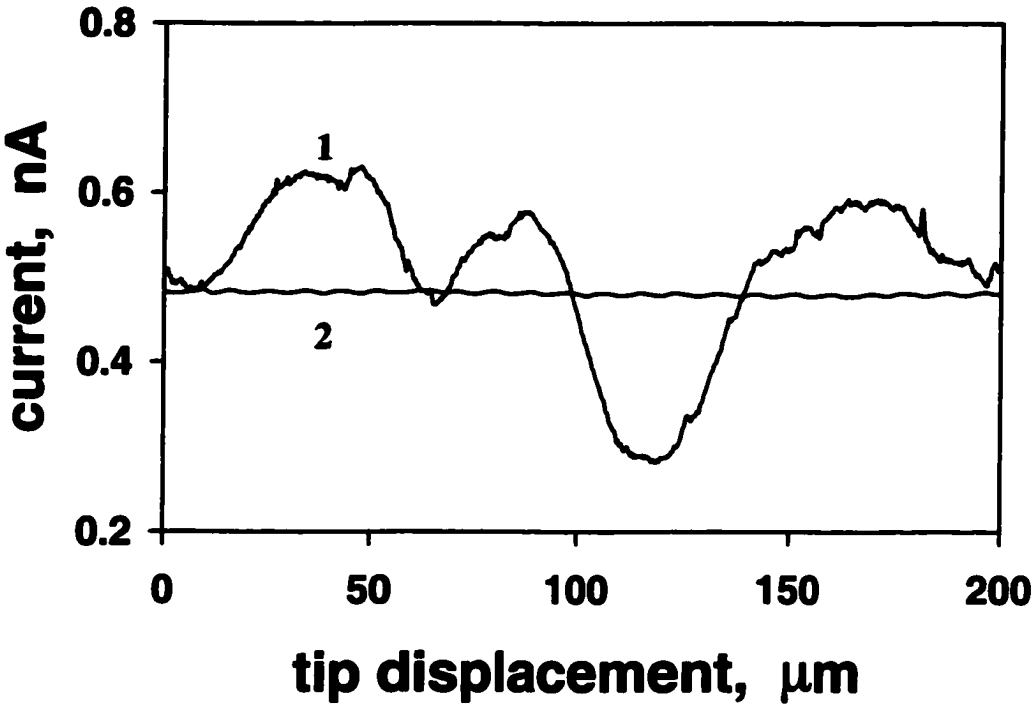

Fig. 2.18 Images of the lipid films adsorbed at the BZ/water interface obtained by scanning a 12.5-μm-radius tip along one axis parallel to the phase boundary. The ITIES was covered with a complete monolayer of PS lipid (C-10). Aqueous phase contained 10 mM $Na_4Fe(CN)_6$, 0.1 M NaCl, and 0.1 M $NaClO_4$. BZ was 0.5 mM in ZnPor and 0.25 M in $THAClO_4$. The lipid concentration in BZ was 100 μM. The concentration of Ca^{2+} in the aqueous phase was (1) 20 and (2) 0 μM. The tip/ITIES distance was ~4 μm.

The stability of the domains on the phase boundary was checked using forward (Figure 2.19, curve 1) and reverse (curve 2) scans at the same spot of the interface. Although the forward and reverse scans are not completely retraceable and some interfacial features change on the experimental timescale (~2 min), the essential features of the imaged domains are reproducible. Interestingly, the distribution of defects in the

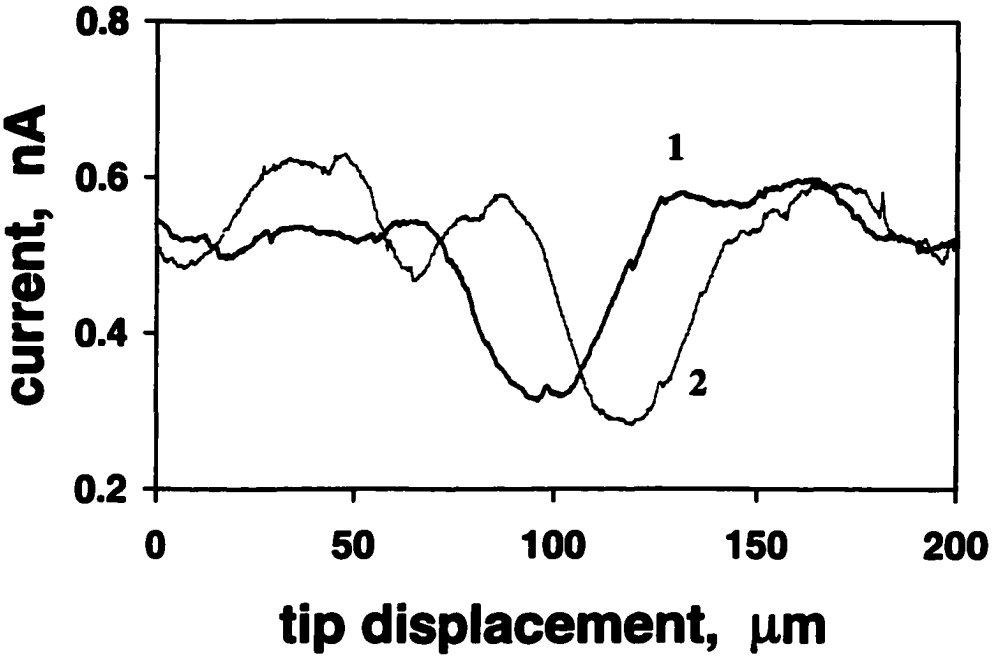

Fig. 2.19 Forward (curve 1) and reverse (curve 2) scans of an SECM tip above the same area of the lipid film formed in the presence of calcium ion in the water phase. For parameters, see Fig. 2.18.

monolayer depends greatly on the way those defects were nucleated. Figure 2.20 shows the data obtained at a PS (C-10) monolayer, which was adsorbed at the ITIES with no divalent cation present in the aqueous solution. After the PS monolayer was formed, 20 μM Ca^{2+} was added into the aqueous solution. The feedback current increased significantly after the addition of Ca^{2+} to the water phase (cf. curve 1 in Fig. 2.18). However, no domain structure was detected when the tip was scanned horizontally (in x-y plane) above the interface (Fig. 2.20). Thus, the exposure of a preformed PS monolayer to calcium results in the formation of pinhole defects, which are uniformly distributed on the interface, and a consistently increased ET rate across the film.

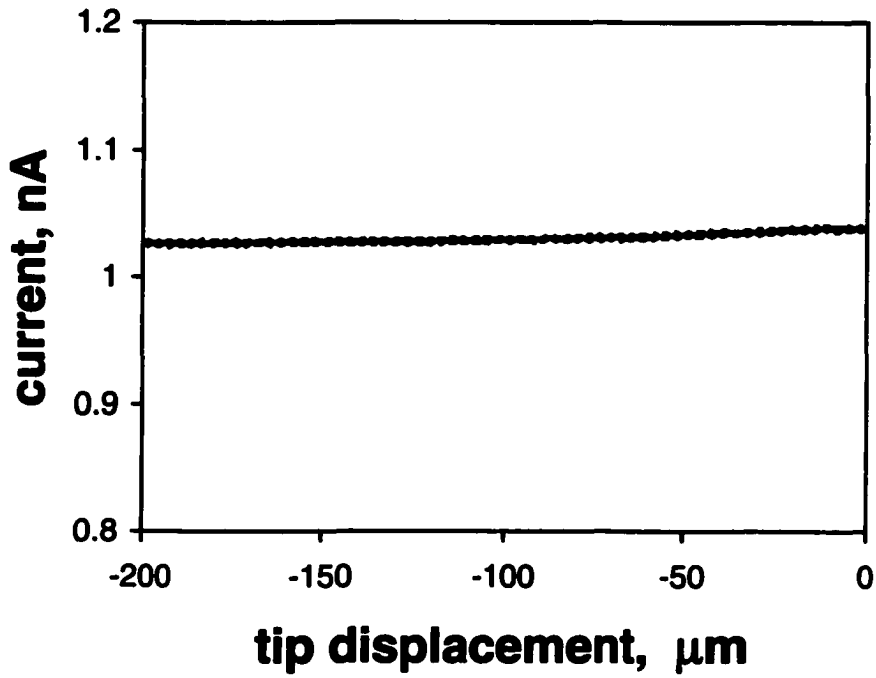

Fig. 2.20 An SECM tip was scanned in x-direction above a C-10 monolayer adsorbed at the BZ/water interface one hour after the addition of 20 μM Ca^{2+} to the aqueous phase. Other conditions are the same as for curve 2 in Fig. 2.18.

2.4 Conclusions

The rate constant of ET across the ITIES is essentially independent of interfacial potential drop in the absence of interfacial adsorption of the common ion when the organic redox reactant is a neutral species. This result is in agreement with the widely accepted three-layer model of the ITIES (14,16,17). The Butler-Volmer-type dependence of k vs $\Delta_w^o \phi$ for ET involving charged organic species may be attributed to the diffuse layer effect. However, when a spacer (e.g., a molecular monolayer of a long-chain lipid) prevents

the reactants from coming very close to the phase boundary, the interfacial voltage drops between the aqueous and organic redox species, and the true potential dependence of the rate constant can be observed.

The solvent dynamics effect on ET at the ITIES was observed for the first time. The rate of the ET from ZnPor to $Ru(CN)_6^{3-}$ at the DCE/water interface was about three times as fast as the analogous reaction at the NB/water interface.

When a surface active common ion (e.g., TBA^+) is added to the ZnPor/$Ru(CN)_6^{3-}$ system, it can displace ZnPor from the interface. Under these conditions, the ET rate exhibits strong dependence on the interfacial potential ($\Delta_w^o \phi$). The desorption of ZnPor apparently increases the fraction of the interfacial voltage dropping between the reactants and in this way increases the potential dependence of the ET rate. A strong dependence of k_b on $\Delta_w^o \phi$ observed for ET involving neutral redox species dissolved in organic phase suggests that the potential drop across a mixed-solvent layer may be larger than a few mV value suggested previously (14,16,17).

Long-range ET was probed across 1,2-diacyl-sn-glycero-3-phospho-L-serine monolayers. The blocking properties of these films turned out to be similar to those previously reported for phosphatidyl choline monolayers (4). A relatively weak distance dependence of ET rate points to partial penetration of $ZnPor^+$ into the lipid monolayer. An attempt to solidify phosphatidyl serine films by adding calcium ions to the aqueous phase resulted in a formation of two types of domains in the monolayer. Although micrometer-sized domains in lipid monolayers often form under the increased surface pressure and also in the mixed films, the observation of a domain structure in a monolayer formed from a single lipid at the ITIES is not common. The properties of the film depend dramatically on the adsorption conditions, thus indicating the importance of nucleation phenomena for the formation of the domains.

Chap III

Probing Ion Transfer Reactions by Dual-Pipet Techniques

3.1 Introduction

IT reactions across interfacial boundaries are common in chemical and biological systems. They are of great important for natural and artificial membranes, conductive polymers, sensors and separation processes [1-3]. Many methods of metal/liquid electrochemistry can be employed for studies of IT at the ITIES [4-7]. However, fast measurements at the ITIES (e.g., fast-scan cyclic voltammetry, short-time chronoamperometry, and pulse experiments) are problematic because of inherently high resistance and capacitance. Probing rapid IT and homogeneous reactions coupled with ion transfer at the ITIES is difficult.

The problems arising from uncompensated resistance and charging current can be diminished by placing one of two liquid phases in a micropipet to create a micro-ITIES [8]. Micropipet voltammetry introduced by Taylor and Girault [9] has been successfully used to probe kinetics and thermodynamics of various IT processes [4-7]. However, micropipet techniques have not been widely employed for investigating multistep mechanisms involving IT and homogeneous ionic reactions. Although a vast literature concerning different types of ionic reactions (e.g., S_N2-type processes [10,11], various organic transformations involving charged metal complexes [12], and ion binding to polyelectrolytes [13] and DNA [14]) exists, relatively few electrochemical studies of such reactions have been reported.

Another alternative to fast perturbation measurements is using steady-state generation/collection (G/C) techniques. These methods, including well-known rotating ring-disk electrodes [15], closely spaced arrays of microelectrodes [16-19], and scanning electrochemical microscopy (SECM) [20], have been successfully employed for studying complicated mechanisms and probing charge/mass transport in various media. The concept common for all these methods is generation of electroactive species at one

electrode ("generator") and detection of the resulting flux at the second electrode ("collector"). Both generator (i_g) and collector (i_c) currents as well as collection efficiency (i.e., the ratio of two currents, $\eta = i_c/i_g$) can be used to investigate charge transport and chemical reactions occurring in the gap between two electrodes.

The present work aimed to develop a new electrochemical generation/collection (G/C) technique based on the use of dual-pipet (or θ-pipet) electrodes for studying heterogeneous IT reactions and homogeneous chemical reactions involving ionic species [21,22]. This technique allows quantitative separation of different charge transfer processes simultaneously occurring at the liquid/liquid interface (e.g., simple transfer of potassium, facilitated transfer of the same ion with a crown ether and IT of supporting electrolyte). Such parallel processes often impair the studies of charge transfers at the liquid/liquid interface [4]. Another advantage of this technique is the possibility to overcome potential window limitations and study numerous important reactions occurring at high positive or negative potentials (e.g., transfers of alkali metals from water to organic media).

A θ-pipet consists of two micrometer- or submicrometer-sized pipets (usually filled with aqueous solutions) separated by a submicrometer-thick band of glass. In a simple IT experiment, one of the pipets "generator") contains a cation (or an anion) that can be transferred to the outer (usually organic) solution by biasing this pipet at a positive potential, E_g, with respect to the external reference electrode. A significant fraction of ejected cations reach the negatively biased second pipet ("collector") and get transferred back into the aqueous phase (Figure 3.1A). If the collector potential (E_c) is sufficiently negative for the transfer reaction to be controlled by diffusion, the collection efficiency reaches its maximum value, which is determined by device geometry and is essentially independent of E_g [21,22].

An ion ejected from the generator pipet may participate in a homogeneous chemical reaction. When such a reaction affects the collection efficiency, its kinetics and/or thermodynamics can be probed. If the reaction product does not contribute to the collector current (i.e., either it cannot be transferred into

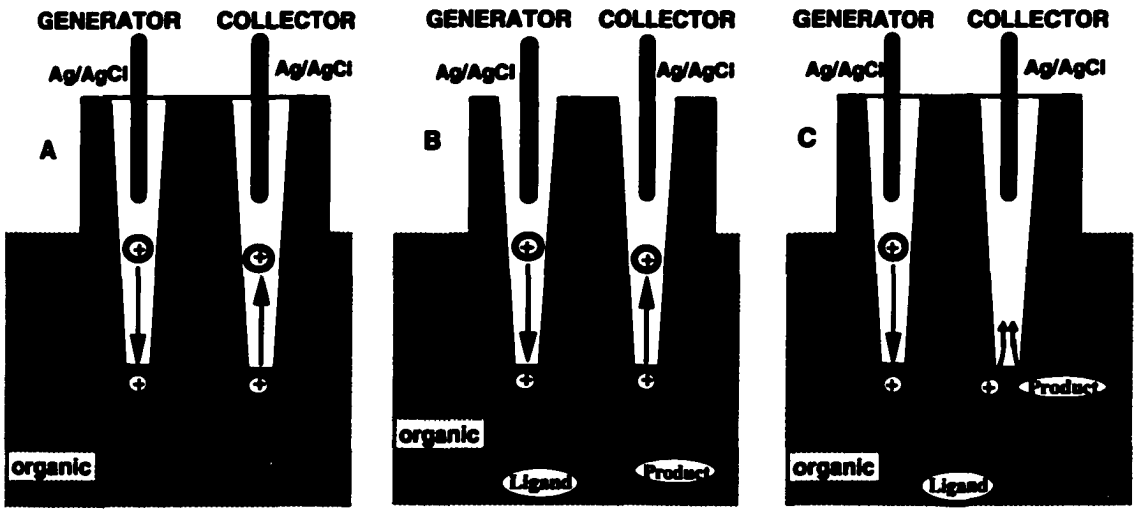

Figure 3.1. Probing ionic reactions with a dual-pipet device. (A) Simple transfer of a cation, (B, C) IT is followed by a chemical reaction in solution. (B) The reaction product is not transferred into the collector pipet. (C) Both the cation and the reaction product are collected.

water or its diffusion coefficient is too small. Ion binding to high molecular weight DNA is a typical example of the latter), the collection efficiency decreases with increasing rate of coupled homogeneous reaction (Figure 3.1B). If the reaction product is charged and can be transferred to water (Figure 3.1C), the collector voltammogram consists of two waves occurring at different potentials and corresponding to the product and cation transfers. A number of metal ion complexation reactions belong to the this class, e.g., potassium transfer from water into 1,2-dichloroethane (DCE) facilitated by dibenzo-18-crown-6 (DB18C6):

$$K^+ (w) + DB18C6 (DCE) \rightarrow K^+DB18C6 (DCE) \text{ (generator pipet)} \quad (1a)$$

$$K^+DB18C6 (DCE) \rightarrow K^+ (w) + DB18C6 (DCE) \text{ (collector pipet)} \quad (1b)$$

The facilitated transfer of potassium to DCE expressed by eq 1a occurs at significantly less positive potentials than a simple transfer of K^+

$$K^+ (w) \rightarrow K^+ (DCE) \text{ (generator pipet)} \qquad (2a)$$

Conversely, the reverse transfer of potassium from DCE into the aqueous phase via interfacial dissociation (reaction 1b) occurs at significantly more negative E_c than the simple transfer (reaction 2b)

$$K^+ (DCE) \rightarrow K^+ (w) \text{ (collector pipet)} \qquad (2b)$$

Here, we use this model experimental system to show the possibility of quantitative separation of different IT processes from each other and from the transfer of supporting electrolyte and explore the possibility of mechanistic analysis of a complex process using θ-pipets.

Using a θ-pipet device one also can perform measurements in a thin liquid film formed on the surface of glass separating two pipets. In this way, voltammetry can be carried out "in the air", i.e., in the absence of the external liquid macrophase. Three different possibilities are outlined in Figure 3.2. In Figure 3.2A one of the pipets (e.g., a generator) is filled with an aqueous solution and the second one (e.g., a collector) with an organic solution. An ion ejected from the generator pipet can travel through the liquid film and be transferred into the collector pipet. This process is driven by external voltage applied between two internal reference electrodes inserted into the θ-pipet. Alternatively, two barrels of the θ-pipet can be filled with the same phase (e.g., organic) and separated by a thin film of the second (e.g., aqueous) phase acting as a liquid membrane (Figure 3.2B).

Finally, a θ-pipet device can be used as a sensor for water-soluble (or organic) gaseous species that can change the composition and ionic conductivity of the thin liquid layer (Figure 3.2C). Amperometric

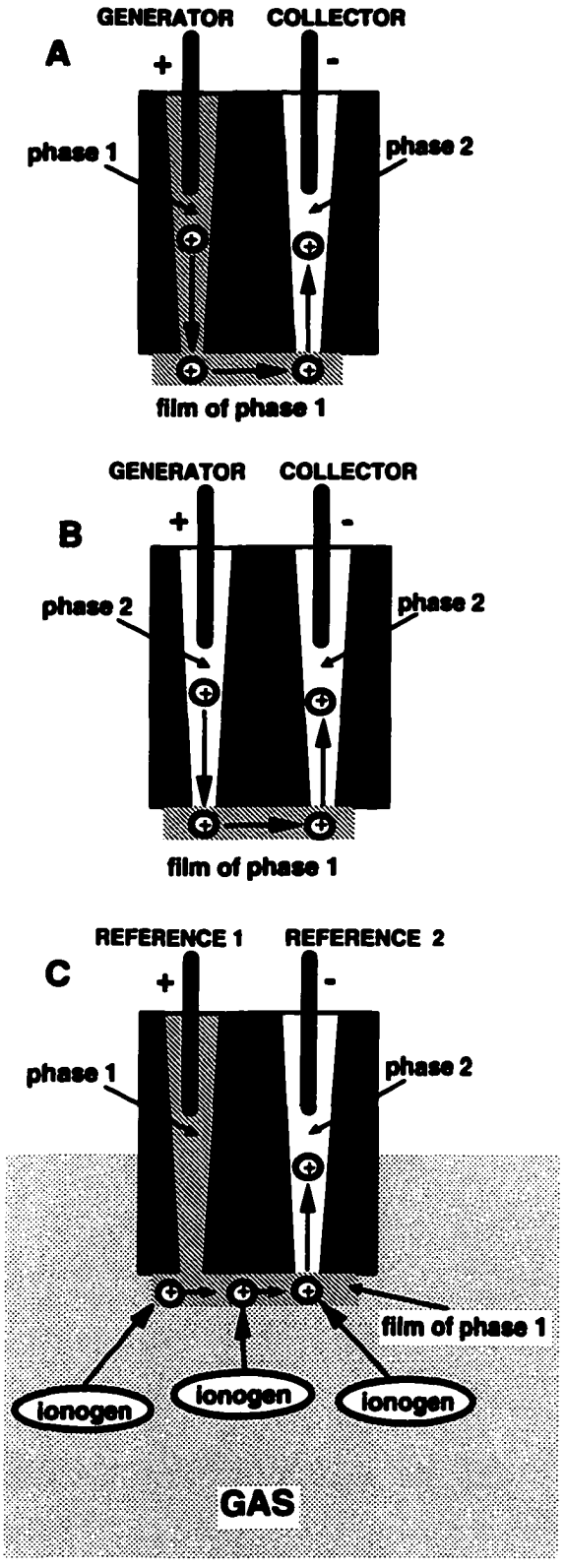

Figure 3.2. Voltammetry "in air" (A, B) and gas sensing (C) using θ-pipets.

measurements at solid electrodes "in air", i.e., without bulk solution phase, have been reported earlier [23-26]. The presence of a thin liquid film on the electrode surface is essential for such measurements [24]. Because the liquid films spontaneously forming on solid electrode surfaces are extremely thin and resistive [26], the obtained voltammograms were poorly shaped and distorted by resistive potential drop. A somewhat thicker and less resistive film linking two barrels of the θ-pipet yields higher quality voltammetric response suitable for qualitative and quantitative analytical determinations.

3.2 Experimental section

3.2.1 Chemicals

Tetrahexylammonium perchlorate ($THACIO_4$) and LiCl from Johnson Mathey (Ward Hill, MA), $MgCl_2$ from Fisher (Fair Lawn, NJ), dibenzo-18-crown-6 from PCR Research Chemicals (Gainesville, FL), 1,2-dichloroethane (99.8% HPLC grade), tetrabutylammonium chloride (TBACl), potassium tetrakis(4-chlorophenyl)borate (KTPBCl) and KCl from Aldrich (Milwaukee, WI) and trimethylchlorosilane (Hüls America, Inc., Bristol, PA) were used as received. Tetrabutylammonium tetrakis(4-chlorophen-yl) borate (TBATPBCl) was prepared as described previously [27] and served as a supporting electrolyte for the organic phase. All aqueous solutions were prepared from deionized water (Milli-Q, Millipore Corp.).

3.2.2 Instrumentation

The EI-400 bipotentiostat (Ensman Instruments, Bloomington, IN) was employed to control the potentials of two pipets serving as working electrodes with respect to the organic reference electrode and record cyclic voltammograms. Voltammograms "in air" were obtained using a BAS 100B electrochemical workstation (Bioanalytical Systems, West Lafayette, IN). All prepared pipets were inspected before measurements using an Olympus BH2 optical microscope (×100 - ×1000 magnification).

3.2.3 Pipets and Electrochemical Cells

Dual-pipet electrodes were made from borosilicate θ-tubing (OD = 1.5 mm, Sutter Instrument Co.) using a Sutter model P-2000 laser-based puller. The shape of a pulled θ-pipet is determined by the choice of laser puller parameter values. These values are specific for a given puller, i.e., two different pullers of the same type (e.g., P-2000) may require significantly different programs to produce similar pipets. Moreover, the performance of each puller changes slightly with time, so the pulling program has to be modified. Hence it is impossible to specify a program that would allow reproducible fabrication of pipets with the desired properties. Such a program has to be found by a trial-and-error method. A proper choice of pulling parameters yielded two very similar closely spaced pipets. Unless there is a special need for two halves of the θ-pipet to be different, the similarity of the two radii is advantageous because the symmetry of the device can somewhat simplify the data analysis. Since the ohmic resistance of a pipet is largely determined by the length of the narrow shaft leading to the orifice [28,29], a pulling program was developed to produce short (patch-type) pipets. Both the orifice radii and the thickness of the pipet wall were measured microscopically.

The pipets were filled with either aqueous or organic solutions from the back using a small (10-25 μL) syringe. A 0.125 mm silver wire coated with either AgCl (for aqueous filling solution) or AgTPBCl (for organic filling solution) was inserted into each pipet from the back.

The outer glass wall was silanized to prevent the formation of an aqueous film between two pipets and mixing of the filling solutions. This was done by dipping the pipet tip into trimethylchlorosilane for 1-2 min while the flow of argon (sufficiently fast to produce small bubbles) was passed through the pipet from the back to avoid silanization of the inner wall of a pipet. This was crucial because the outer organic solvent gets drawn inside a pipet if its inner surface is hydrophobic [30].

Voltammetric experiments with micropipets were carried out in a 5 mL vial inside a Faraday cage. Using a bipotentiostat, the voltage was applied between the reference electrode inside each barrel of the θ-pipet and the reference electrode in the outer solution. All experiments were carried out at room temperature (25 ± 2 °C).

3.2.4 Voltammetry in the Gaseous Phase

Voltammetric experiments without external solution were carried out using a θ-pipet with one barrel filled with an aqueous solution and the second barrel filled with organic phase. In a two-electrode setup, voltage was applied between Ag/AgCl and Ag/AgTPBCl reference electrodes inserted in two barrels. The glass surface was not silanized, and the pipet orifices were linked by a thin aqueous film formed on the outer pipet wall (Fig 3.2C) [30]. In this arrangement, water sometimes flows into the second barrel and forms a micrometer-thick aqueous layer, which can be seen microscopically. Such pipets have been discarded. Only dual pipets with no detectable amount of water inside the second barrel were employed in our experiments. Thus the liquid/liquid interface was confined to the orifice of the organic-filled capillary.

To measure concentrations of gaseous compounds, a θ-pipet was introduced in a 20 mL vial through its airtight stopper. The vial contained a ~2 mL solution of a volatile substance (e.g., ammonia or nitric acid), and the distance between the pipet tip and the solution surface was ~1 cm. Several voltammograms were recorded during a few minute period. The experiment was carried out until the pipet response stabilized, so the successive voltammograms were virtually identical. Then the pipet was introduced in the next vial containing a higher concentration of the substance of interest.

3.3 Results and discussion

3.3.1 Characterization of θ-Pipets

Similar to conventional, single-barrel pipets, the size and shape of θ-pipets can be changed by varying the pulling parameters. In particular, the radius of each of two orifices can be either on a micrometer or a submicrometer scale. If the device is micrometer-sized, it can be characterized by optical microscopy. The θ-pipet in Figure 3.3 has two similar micrometer-sized apertures separated by a submicrometer-thick glass wall. An air bubble trapped in one of the barrels can be removed by gently knocking on the outer wall. Unlike single-barrel pipets whose orifice is typically disk-shaped, the apertures of a dual pipet look like two halves of an ellipse separated by a very thin line of glass. An

advantage of such geometry compared to a more symmetrical group of two coplanar disks is a somewhat higher collection efficiency. The theory developed recently for two identical coplanar disk electrodes acting as a generator and a collector predicts the maximum steady-state collection efficiency of about 36% for a close spacing of two electrodes (i.e., the edge-to-edge distance is much smaller than the disk radius) [31]. While η as high as ~50% was obtained with θ-pipets (see next section). However, simulating mass transfer in such a system is challenging, and no exact theory is currently available for θ-pipets.

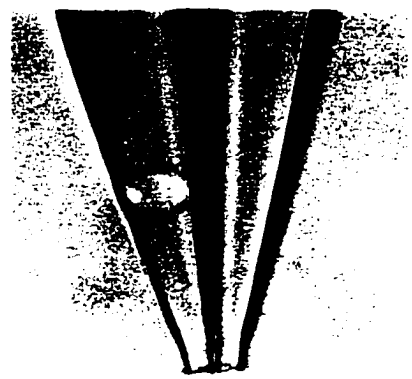

Figure 3.3. Photomicrograph of the θ-pipet filled with an aqueous solution. A thin (≤ 1 μm thick) glass wall separates two barrels, one of which is blocked by an air bubble. Both orifices are ~ 4.5 μm radius.

Two main objectives of electrochemical characterization of a dual pipet are to determine the effective radii and to check that each of two pipets can be independently polarized. The radius of each orifice can be evaluated from an IT voltammogram obtained at one pipet while the second one is disconnected. As discussed previously [30], the diffusion limiting current to a water-filled single pipet

with a sufficiently thick, silanized outer wall can be calculated from eq 3 where D and c respectively are the diffusion coefficient and concentration of species in the outer solution responsible for the interfacial charge-transfer reaction, a is the effective radius of the pipet orifice, F is the Faraday constant, and n is the transferred charge. The effective radius values calculated from eq 3 for both halves of the θ-pipet must be close to the values found from optical microscopy.

$$i_d = 4nFaDc \qquad (3)$$

Similar to single-barrel pipets [30], the outer surface of a water-filled dual pipet has to be silanized to prevent formation of an aqueous film. Such a film can short-circuit the θ-pipet by connecting its two halves. In the absence of a surface aqueous layer, the currents flow between each of two pipets and the external reference electrode. In contrast, when the liquid film connects two orifices, the current flows directly from one pipet to the other. Two simple experiments allowing the distinction between these two cases were carried out using the model reaction of facilitated potassium transfer (reaction 1a and 1b). The generator and collector pipets were as follows:

Cell 1:
(generator)
Ag/AgTPBCl/*x* mM DB18C6, 10 mM TBATPBCl, DCE//20 mM KCl, H_2O/AgCl/Ag
outer DCE solution generator pipet

(collector)
Ag/AgTPBCl/x mM DB18C6, 10 mM TBATPBCl, DCE//10 mM $MgCl_2$, H_2O/AgCl/Ag
outer DCE solution collector pipet

In the first experiment, both pipets are initially biased at the same potential (with respect to the external reference) at which no appreciable current flows at either pipet. Then the potential of the generator pipet (E_g) is scanned in a positive direction to induce ejection of potassium ions, while the collector potential (E_c) is kept constant. In the absence of an aqueous surface layer, two voltammograms, i.e.,

steady-state generator (curve 1 in Figure 3.4A) and collector (curve 2) voltammograms are obtained. These voltammograms correspond to the transfer of K^+ across the water/DCE interface (see section 3.3.2 below). In contrast, if the water film links two pipets, positive (generator) and negative (collector) currents of exactly the same magnitude are observed in an analogous experiment (Figure 3.4B). The current-voltage curves are linear because the current is controlled by resistance between two Ag/AgCl electrodes rather than by the interfacial IT rate. The large current represents the flow of supporting electrolyte between two pipets. The complete resistance of the generator/aqueous film/collector system calculated from Figure 3.4B using Ohm's law was R = 67 MΩ. Subtracting from this value the doubled value of the resistance of a ~ 5 μm diameter pipet filled with 0.01 M aqueous electrolyte (~ 10 MΩ [32]), one can evaluate the resistance of the aqueous layer to be ~ 50 MΩ. Since the width of the aqueous film (i.e., the distance between two orifices) is ≤ 1 μm, such a high ohmic resistance indicates that the layer is only a few nanometers thick.

The generator and collector voltammograms were recorded for all θ-pipets before they were used for probing IT reactions. The pipets showing the "short-circuit" type voltammograms (Fig. 3.4B) were discarded.

3.3.2 Probing Ion-Transfer and Homogeneous Ionic Reactions

Typical generator and collector voltammograms of potassium transfer (see cell 1) are shown in Figure 3.5A and 5B. The generator voltammogram (curve 1 in Figure 3.5A, the left-hand current scale) is due to facilitated transfer of K^+ into DCE (reaction 1a) and the corresponding steady-state collector voltammogram (curve 1 in Figure 3.5B, the left-hand current scale) represents the reverse transfer of K^+ into water (reaction 1b) [28,32,33]. As expected, the i_g is limited by diffusion of DB18C6 in DCE as long as its concentration, c_{DB18C6}, is much lower than the potassium concentration inside the generator pipet (in Figure 3.5, c_{DB18C6} = 0.5 mM and c_{KCl} = 20 mM) [28,32,33]. The pipet radius calculated from the limiting current (4.5 μm) was in agreement with the value found by optical

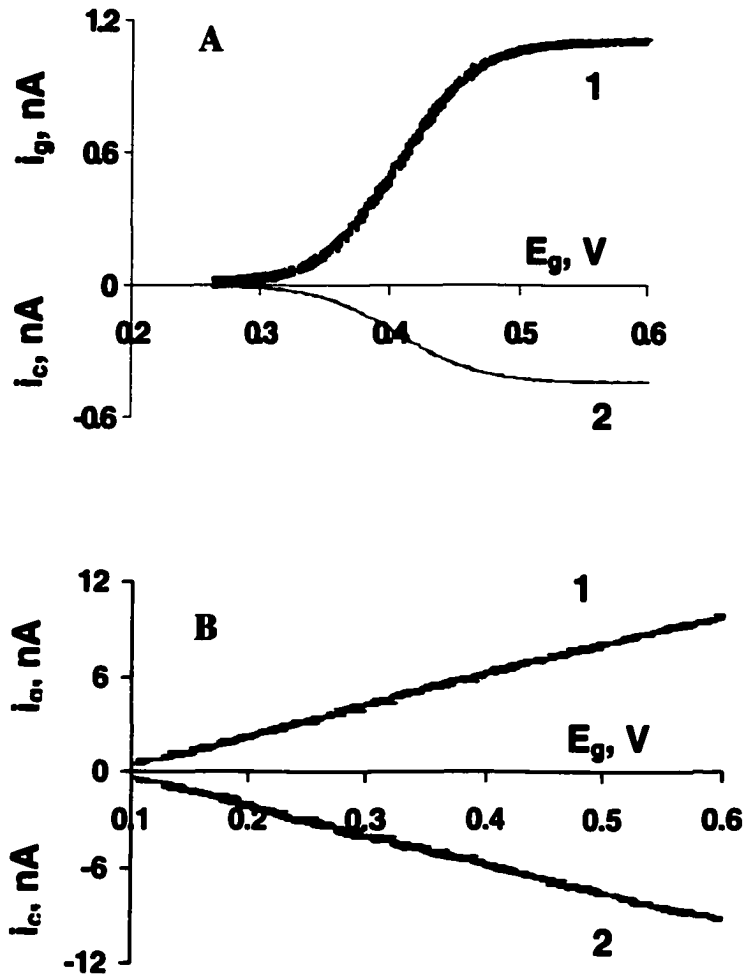

Figure 3.4. (A) Generator (1) and collector (2) voltammograms of the transfer of K^+ between water and DCE containing DB18C6. Solid line in curve 1 is the generator voltammogram reconstructed from the i_c vs E_g data as described in the text. (B) i_g vs E_g and i_c vs E_g curves obtained with an aqueous film linking two barrels of the θ-pipet. E_c was (A) 0.25 and (B) 0.1 V vs AgTPBCl. DCE contained 1 mM DB18C6. Generator potential was swept at (A) 20 and (B) 100 mV/s. The effective radii of the generator and collector pipets are $r_g \approx r_c \approx 5$ μm. For other parameters, see cell 1.

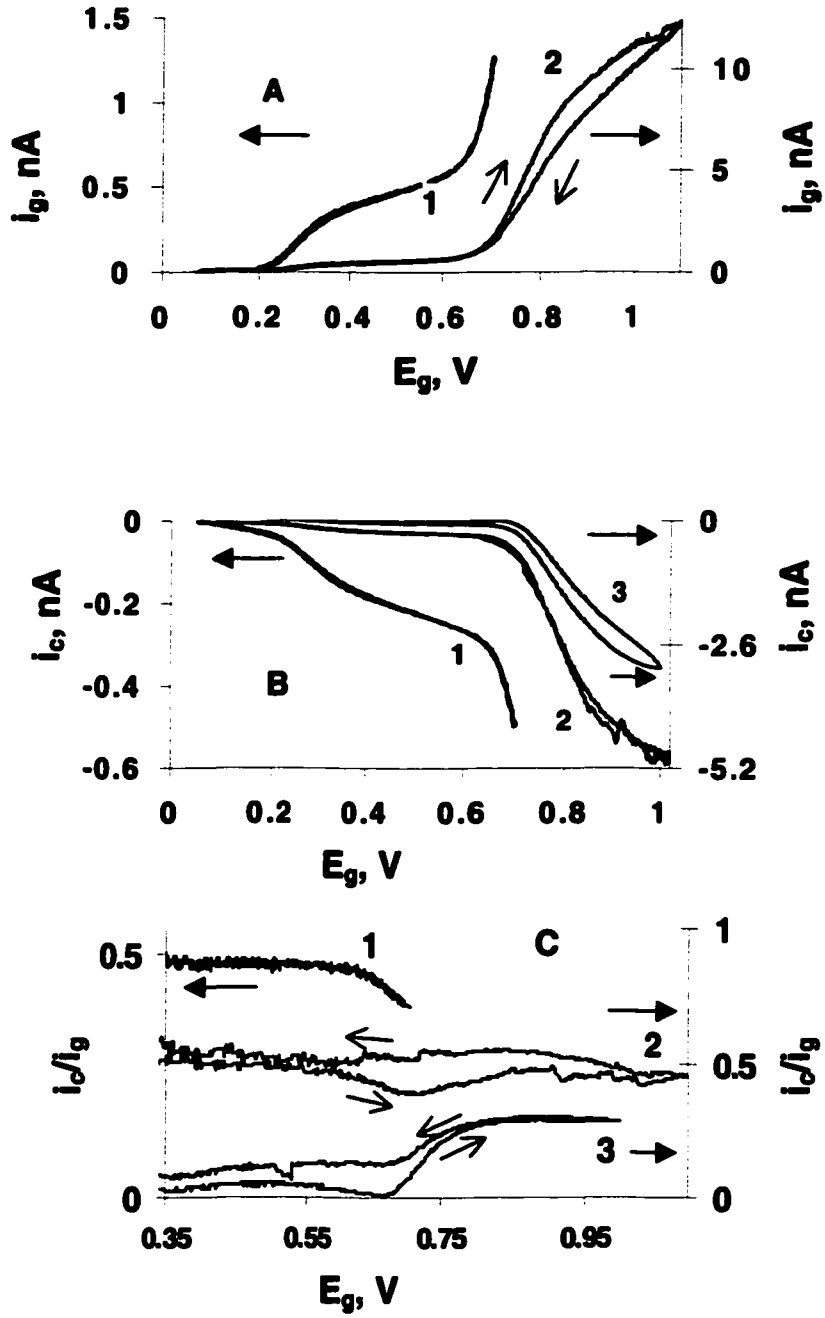

Figure 3.5. Generator (A) and collector (B) voltammograms and collection efficiency (C) for the transfer of K^+ between water and DCE containing DB18C6. V =20 mV/s. $r_g = r_c = 4.5$ μm. Curves 1 correspond to the left-hand current scale, curves 2 and 3, to the right-hand scale. In (B) and (C) E_c was: (1) 0.2, (2) 0.2, and (3) 0.6 V vs AgTPBCl. DCE contained 0.5 mM DB18C6. For other parameters see Cell 1.

microscopy. A more accurate radius value (4.8 μm) was determined from the slope of limiting current vs c_{DB18C6} (Fig. 3.6). As expected, this dependence was strictly linear with a practically zero intercept.

The study of simple IT of acetylcholine (Ach^+) between water and DCE phases has shown that the collection efficiency of Ach^+ remains practically constant over a wide range of E_g [21]. Similarly, the collection efficiency of K^+ depends strongly on the collection potential (η changed from 0 to ~ 50% over the range of E_c from 600 to 200 mV) and was practically independent of generator potential at E_g < 0.6 V (Figure 3.5C, curve 1). This indicates that generator current is produced by a single IT reaction, i.e., facilitated transfer of potassium (reaction 1a). The same half-wave potential ($E_{1/2}$) value of 290 ±10 mV was obtained from both generator and collector curves.

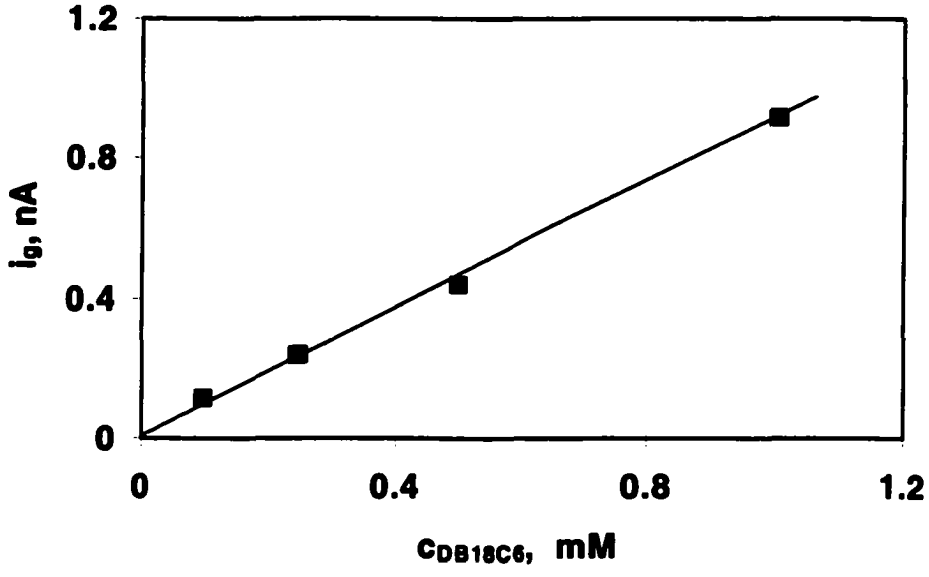

Figure 3.6. The dependence of the limiting generator current on the concentration of DB18C6 in DCE phase.

An increase in i_g at $E_g \geq 0.6$ V (Figure 3.5A, curve 1) is due to two simultaneously occurring processes, i.e., unassisted transfer of K^+ into DCE and the transfer of supporting electrolyte ($TPBCl^-$) into water [34,35]. Since $c_{KCl} \gg c_{DB18C6}$, the DB18C6 ligand is depleted in the proximity of the generator, and most ejected K^+ ions are uncomplexed. At $E_c = 0.2$ V (curve 2 in Figure 3.5B) both complexed and uncomplexed potassium ions are collected. Nevertheless, the η decreases at $E_g \geq 0.6$ V because the transfer of supporting electrolyte does not contribute to i_c (curve 2 in Figure 3.5C). The ratio of the collection efficiency at a given E_g to its plateau value (at $E_g < 0.6$ V) represents the fraction of i_g produced by potassium transfer. At $E_c = 0.6$ V (curve 3 in Figure 3.5B) only uncomplexed K^+ is collected (the interfacial dissociation of $K^+DB18C6$ at this potential is slow). Unlike in curve 2, no initial wave of facilitated transfer is seen in curve 3.

The collection efficiency at $E_c = 0.6$ V (curve 3 in Figure 3.5C) is low when $E_g < 0.6$ V because almost all of the transferred potassium ions are in a complexed form. The steep increase in η at more positive potentials is due to ejection of uncomplexed K^+. The ratio of the limiting collection efficiency in curve 3 to that in curve 2 (~ 0.7) equals the fraction of uncomplexed K^+ in all potassium arriving at the collector and represents the extent of complexation reaction.

Unlike i_g, the i_c wave at E_c =0.6 V (curve 3 in Figure 3.5B) is only due to the transfer of K^+. To our knowledge, this is the first direct observation of the simple potassium transfer wave. The interfering transfer of organic anions into the aqueous phase greatly complicates conventional voltammetric studies of alkali metal transfers [34,35]. From both curves 2 and 3 in Figure 3.5B the half-wave potential of simple potassium transfer, $E_{1/2} = 770 \pm 10$ mV, can be extracted. The difference between this value and the $E_{1/2}$ of the facilitated transfer of potassium is about 480 mV, which corresponds to a very large association constant for reaction 1a of the order of 10^9 M^{-1}.

As shown in Fig. 3.5C, when only one IT process occurs at a generator (i.e., at $E_g < 0.6$ V) the collection efficiency, η, is essentially independent of E_g. In this case, η is determined by collector potential and device geometry and is independent of i_g. Thus, one can measure the maximum value of

η (η_{max}) when all ions reaching the opening of the collector pipet are transferred into it. The η_{max} is a constant characteristic for a given θ-pipet. Consequently, it should be possible to reconstruct the generator voltammogram from an i_c vs E_g dependence. For an uncomplicated IT reaction with diffusion-controlled collection, the generator current at any E_g can be calculated as

$$i_g = i_c/\eta_{max} \qquad (4)$$

An example of such a reconstruction is shown in Figure 3.4A, where the generator voltammogram (curve 1, solid line) was calculated from the collector voltammogram (curve 2) using eq 4 with η_{max} = 0.396. A perfect agreement between calculated and measured i_g values (solid line and symbols) proves the validity of the reconstruction. A similar procedure is useful for more complicated processes in which more than one IT reaction contribute to the i_g, and the analysis of generator voltammograms is difficult. If only one kind of ion is collected, eq 4 gives the component of the generator current produced by transfer of this ion.

Two concurrent IT reactions can be separated as shown in Figure 3.7. The simple transfer of potassium from water to DCE (reaction 2a) occurs at a positively biased generator pipet simultaneously with the transfer of $TPBCl^-$ into the aqueous filling solution (see cell 1 with $c_{DB18C6} = 0$)

$$i_g = i_{g,K+} + i_{g,TPBCl-} \qquad (5)$$

Unlike the generator voltammogram (curve 1 in Figure 3.7), which is produced by two different IT reactions and consequently is hard to analyze, a collection voltammogram (curve 2) is only due to the transfer of K^+ from DCE to water. At a low scan rate (e.g., v = 20 mV/s in Figure 3.7) this quasi-steady-state curve is sigmoidal. One can use eq 4 with η_{max} = 0.31 determined independently for the employed θ-pipet to calculate the flux of K^+ ejected from the generator ($i_{g,K+}$) as a function of E_g (i.e., $i_{g,K+} = i_c/\eta_{max}$; curve 3 in Figure 3.5). The subtraction of $i_{g,K+}$ from the original voltammogram (i.e., the subtraction of curve 3 from curve 1) yields the $TPBCl^-$ transfer current at the generator orifice (curve

4). This current is produced by steady-state convergent diffusion of $TPBCl^-$ to a micrometer-sized generator pipet. Despite error produced by subtraction, this voltammogram is retraceable and sigmoidal. One should notice that the half-wave potential of $TPBCl^-$ transfer is ~ 100 mV more

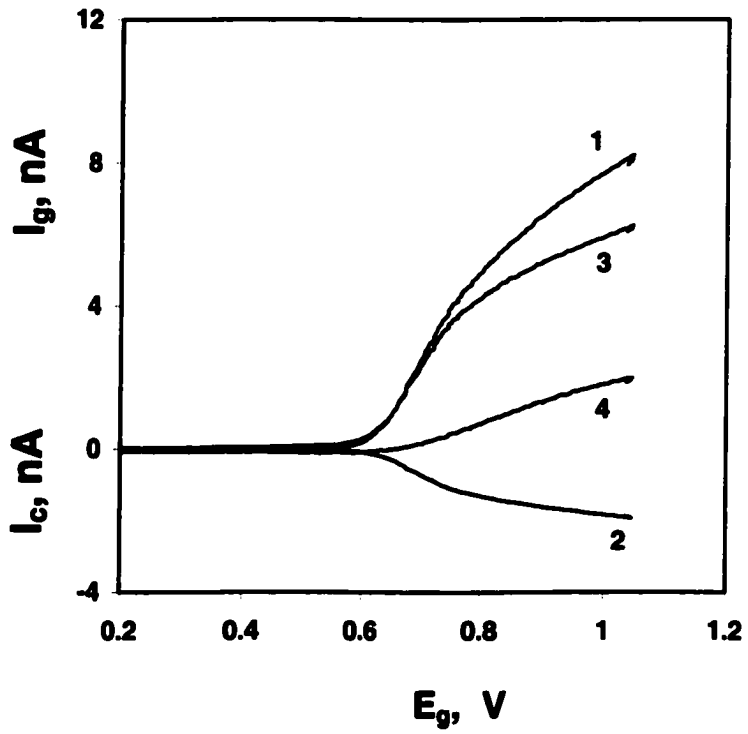

Figure 3.7. Separation of two concurrent IT processes. Generator voltammogram (curve 1) is produced by simultaneously occurring transfers of K^+ and $TPBCl^-$. The flux of K^+ ejected from the generator pipet (curve 3) was obtained from the collection current of K^+ (curve 2) using eq 4. The transfer current of $TPBCl^-$ (curve 4) was obtained by subtraction of curve 3 from curve 1. $E_c = 0.15$ V vs AgTPBCl. $c_{DB18C6} = 0$. For other parameters, see cell 1.

positive than the $E_{1/2}$ of potassium transfer. To our knowledge, this is the first direct observation of the $TPBCl^-$ transfer wave. The overlap of voltammetric waves of alkali metal transfers and those of

hydrophobic anions (e.g., $TPBCl^-$) has previously hindered kinetic studies of these reactions [34-36]. Using the G/C setup, one can quantitatively separate these processes and probe them independently.

A more complicated combination of several IT processes with a homogeneous ionic reaction can be observed when potassium transfer is conducted in the presence of DB18C6 and a large positive potential is applied to the generator pipet. If $c_{DB18C6} \ll c_{KCl}$, the generator current is produced by two IT processes, i.e., facilitated transfer of potassium by DB18C6 (reaction 1a) and simple transfer of K^+ (reaction 2a) (at $E_g < \sim 0.9$ V the transfer of $TPBCl^-$ can be neglected):

$$i_g = i_{g,KDB18C6} + i_{g,K+} \qquad (6)$$

The collector current in this case consists of two components

$$i_c = i_{c,KDB18C6} + i_{c,K+} \qquad (7)$$

where the $i_{c,KDB18C6}$ term represents interfacial dissociation (reaction1b) and $i_{c,K+}$ corresponds to simple transfer of potassium (reaction 2b). Figure 3.8 contains a generator voltammogram (curve 1) and two corresponding i_c vs E_g curves obtained at $E_c = 0.25$ (curve 2) and 0.6 V (curve 3) with $c_{KCl} = 20$ mM, $c_{DB18C6} = 0.25$ mM, and $c_{TPBCl^-} = 10$ mM. Since $c_{KCl} \gg c_{DB18C6}$, the i_g at positive E_g is much higher than the diffusion current of crown ether to the generator pipet ($i_{g,KDB18C6}$), which appears as a small wave at $E_g \sim 0.4$ V.

The collector voltammograms in Figure 3.8 are different because at $E_c = 0.25$ V both complexed and uncomplexed forms of potassium are collected, while only uncomplexed K^+ is collected at $E_c = 0.6$ V

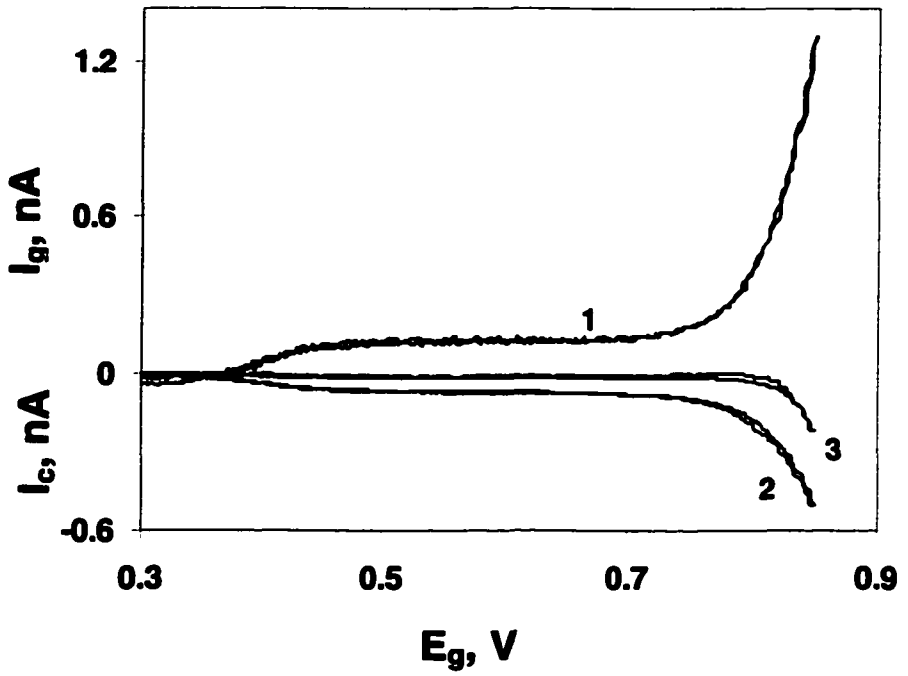

Figure 3.8. Analysis of IT coupled with a homogeneous ion complexation reaction. Generator voltammogram (1) of the transfer of potassium from the aqueous solution into DCE containing 0.25 mM DB18C6 and corresponding background-subtracted collector curves obtained at E_c = 0.25 (2) and 0.6 V (3) vs AgTPBCl. The shape of the generator voltammogram was practically independent of E_c. Collector pipet contained 0.01 M LiCl. r_g = 2 μm and r_c = 3.5 μm. For other parameters, see cell 1.

($i_c = i_{c,K^+}$ because the interfacial dissociation of K^+DB18C6 at this potential is slow). Accordingly, a small steady-state wave corresponding to reaction 1b can be seen in curve 2 but not in curve 3. Apparently, K^+ ejected from the generator pipet at more positive E_g participate in homogeneous complexation reaction with DB18C6 in DCE

$$K^+(DCE) + DB18C6(DCE) \xrightarrow{k_f} K^+DB18C6(DCE) \quad (8)$$

At E_c = 0.25 V (but not at 0.6 V), potassium from K^+DB18C6 species produced by both interfacial and homogeneous complexation reactions can be transferred into the collector pipet. Therefore, the difference between curves 2 and 3 (= $i_{c,KDB18C6}$) represents the total amount of K^+DB18C6 species produced via reactions 1a and 8 that reach the collector orifice. At high positive E_g, the magnitude of $i_{c,KDB18C6}$ is limited by one of three factors: (i) the diffusion of K^+ inside the generator pipet, (ii) the rate of reaction 8, and (iii) the diffusion of DB18C6 to the θ-pipet.

If the diffusion of K^+ were rate-limiting (assumption i), the collection efficiency would be independent of crown ether concentration in DCE. The data in Table 3.1 illustrate the effect of c_{DB18C6} at different collector potentials (i.e., E_c = 0.25 or 0.6 V). As expected, with no complexing agent present in DCE the same η_{max} = 0.37 was measured at both E_c values. At E_c = 0.25 V (at which both complexed and uncomplexed forms of potassium are collected), the collection efficiency is essentially independent of c_{DB18C6}. However, at E_c = 0.6 V, η decreases markedly with increasing c_{DB18C6}. The η vs c_{DB18C6} dependence in Table 3.1 is essentially linear. This is consistent with the diffusion-limited complexation rate (assumption ii). The limiting diffusion flux of DB18C6 in this case is not the flux to the generator orifice but rather to the entire tip area of the θ-pipet (the effective radius of the θ-pipet at the tip was ~ 3 times the radius of the generator aperture). This flux is sufficiently large to account for the amount of K^+DB18C6 arriving to the collector pipet. The rate of reaction 8 can be evaluated from the difference between i_c values at E_c = 0.25 V and E_c = 0.6 V, which represents the total amount of complexed potassium arriving to the collector. Dividing this quantity by collection efficiency, one gets an estimate for the total complexation rate in the system. To evaluate homogeneous complexation rate, the contribution of interfacial complexation (i.e., $i_{g,KDB18C6}$) has to be subtracted

$$\text{homogeneous complexation rate} = [i_c\,(0.25\text{ V}) - i_c\,(0.6\text{ V})]/\eta_{max} - i_{g,KDB18C6} \qquad (9)$$

Table 3.1. Effect of DB18C6 Concentration on Collection Efficiency of Potassium in Cell 1 at Different Collection Potentials; E_g = 0.85 V. η_{max}= 0.37

	collection efficiency	
c_{DB18C6} (mM)	E_c = 0.25 V	E_c = 0.6 V
0	0.38	0.37
0.10	0.35	0.30
0.25	0.35	0.17
0.50	0.36	0.07
1.0	0.37	0.03

Table 3.2. Effect of DB18C6 Concentration on Collection Efficiency of Potassium in Cell 1 at Different Collection Potentials[a]

	collection efficiency	
c_{DB18C6} (mM)	E_c = 0.25 V	E_c = 0.6 V
0	0.17	0.17
0.10	0.16	0.10
0.25	0.17	0.034
0.50	0.17	0.018
1.0	0.17	0.006

[a] The spacing between two pipet apertures is much larger than in Table 3.1. E_g = 0.7 V. η_{max} = 0.17.

Figure 3.9 shows that complexation rate is a linear function of c_{DB18C6}, as one would expect for a diffusion-controlled reaction. However, the linear dependence in Figure 3.9 does not go through he origin because of the approximate nature of eq 9.

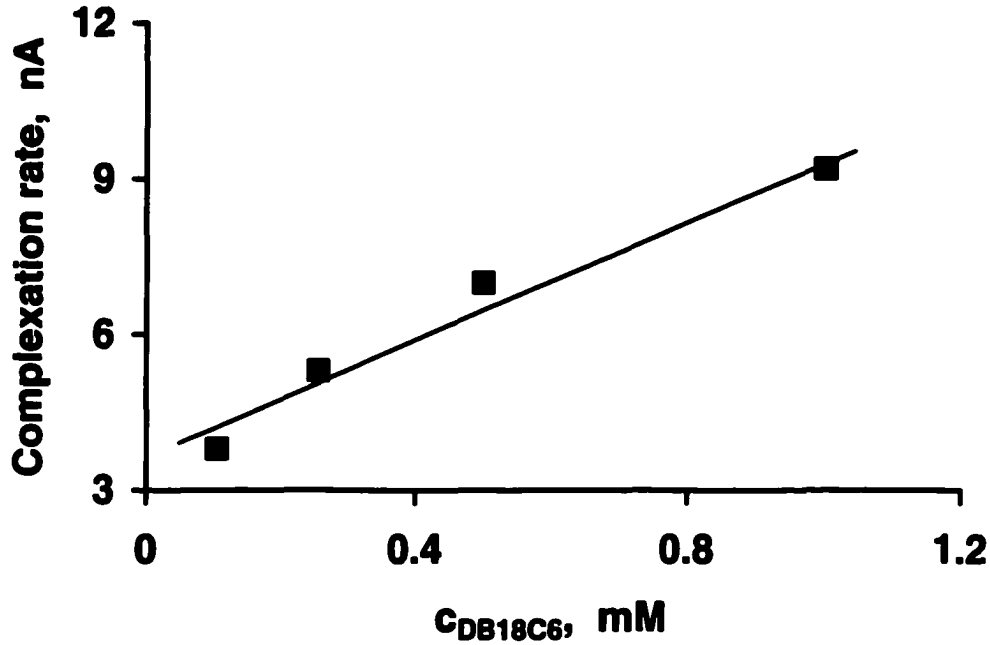

Figure 3.9. Dependence of the homogeneous complexation rate (eq 9) on c_{DB18C6}.

Table 3.2 contains the results of G/C experiments carried out with a different θ-pipet in which the separation distance between orifices was much larger. Hence the $\eta_{max} = 0.17$ is much smaller than the maximum collection efficiency in Table 3.1 (0.37). However, the concentration effect is qualitatively similar, i.e., at $E_c = 0.25$ V, the η is essentially independent of c_{DB18C6}, and at $E_c = 0.6$ V, it decreases with increasing c_{DB18C6}.

To explore the possibility of measuring the kinetics of reaction 8, we carried out G/C experiments with $c_{KCl} \ll c_{DB18C6}$ (e.g., $c_{KCl} = 0.2$ mM, $c_{DB18C6} \geq 0.5$ mM). Under these conditions, the concentration of DB18C6 near the pipet is essentially constant, independent of i_g, and equal to the bulk value (c_{DB18C6}). Reaction 8 can be considered as a pseudo-first-order process whose rate is

$$\text{rate} = k\, c_{K^+}^{\ s} = k_f c_{DB18C6}\, c_{K^+}^{\ s} \qquad (10)$$

where $c_{K^+}^{\ s}$ is the average concentration of K^+ at the θ-pipet surface proportional to i_g and $k = k_f c_{DB18C6}$ is the effective first-order rate constant (s^{-1}). If the kinetics of complexation reaction are rate-limiting, the collection efficiency of uncomplexed potassium for a given pipet (i.e., η at E_c = 0.6 V) should be determined by a single dimensionless parameter, $\kappa = ka^2/D$ [31]. Moreover, the η value measured at E_c = 0.6 V should decrease with increasing c_{DB18C6}. But at $c_{KCl} < c_{DB18C6}$ the measured η values were very low (<1%) and practically independent of c_{DB18C6}. This indicates that homogeneous complexation of potassium ions by DB18C6 in DCE is too fast to be measured using micrometer-sized dual pipets. According to ref [31], the lower limit for the dimensionless rate constant of reaction 8 is $\kappa \sim 10$, which corresponds to $k \geq 500\ s^{-1}$ or $k_f \geq 10^6\ M^{-1}\ s^{-1}$. These numbers represent the upper limit for the determinable complexation rate constant for the current configuration. Smaller (nanometer-sized) pipets are required for probing rapid complexation reactions.

3.3.3 Ion-Transfer Voltammetry "in Air"

In the G/C experiments described above, one has to eliminate the liquid film that spontaneously forms on the outer glass surface and connects two halves of the θ-pipet. The same film can be used to perform different types of electrochemical experiments that can be called voltammetry in air, i.e., with no external liquid macrophase. Several possible arrangements include the following: (i) one pipet filled with an aqueous solution, the second filled with organic phase, and either aqueous or organic film between (Figure 3.2A); (ii) both pipets filled with either water or organic phase and a thin film of an immiscible solvent between them (Figure 3.2B). In this work, only the first arrangement will be discussed. Since the outer surface of the θ-pipet was not silanized, the gap between two pipets was covered with an aqueous film.

Figure 3.10A shows a typical cyclic voltammogram obtained by application of voltage ($\Delta E = E_{Ag/AgCl} - E_{Ag/AgTPBCl}$) across the θ-pipet containing only supporting electrolyte (i.e., 10 mM TBATPBCl in DCE and 10 mM LiCl in water):

Cell 2:

Ag/AgCl/10 mM LiCl, H_2O//10 mM TBATPBCl, DCE/AgTPBCl/Ag

water-filled pipet DCE-filled pipet

This curve is similar to a conventional voltammogram which could be obtained with a single water- or organic-filled pipet immersed in an immiscible external solution [4-7]. The only significant difference is a much wider potential window (i.e., the difference between the onset of TBA^+ ejection from the pipet and Li^+ transfer. The window width is ~ 600 mV for a θ-pipet vs ~ 500 mV for a single pipet). This difference is caused by the resistive potential drop in the aqueous film covering the gap between two barrels. From the iR ~ 100 mV and the current of the order of 1 nA, the calculated resistance is ~ 100 MΩ, which is significantly larger than the resistance of a θ-pipet immersed in DCE. This indicates that the aqueous surface film may be thinner and more resistive in the absence of external solvent.

A well-defined IT cyclic voltammogram in Figure 3.10B was obtained after addition of 0.25 mM DB18C6 to the organic filling solution and replacement of LiCl with KCl in the water-filled pipet. While steady-state concentration profiles are formed in the thin aqueous film connecting two barrels, no full equilibration between this film and the bulk liquids inside pipets can be expected (this would require a long-range diffusion impossible at the experimental time scale). The solution gap works as a tiny (perhaps pL) microreactor in which the processes involving minuscule amounts of reagents can be probed. An example of such measurements is presented in the next section.

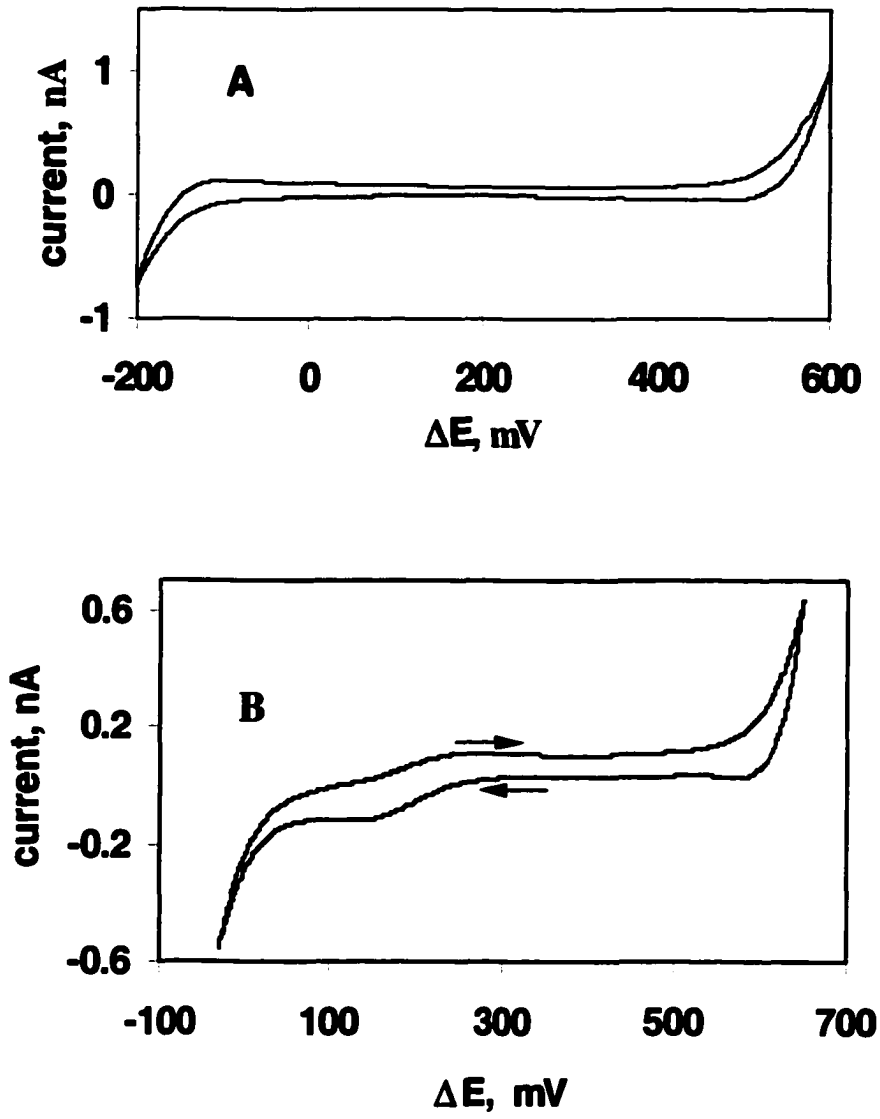

Figure 3.10. Voltammetry "in the air". Background voltammogram (A) and a voltammogram of facilitated potassium transfer (B) obtained by application of voltage between two reference electrodes in cell 2. (B) DCE contained 0.25 mM DB18C6; the aqueous solution contained 20 mM KCl. Arrows indicate the potential sweep direction. v = 20 mV/s. The radii of two orifices are 5.5 (water-filled pipet) and 4.5 μm (DCE-filled pipet).

3.3.4 θ-Pipets as Gas Sensors

The response of a θ-pipet "in air" is largely determined by the properties of the aqueous surface layer, and it is very sensitive to changes in the aqueous film composition. Such changes occur when the pipet is exposed to a soluble gas. Thus, IT voltammetry at a θ-pipet can be used for detection and quantification of gaseous substances. A small ratio of the film thickness to its surface area should result in a high sensitivity and fast response time of such a sensor.

Two detection modes can be used with θ-pipets, i.e., conductivity and IT. In the former case, the concentration of charge carriers in the surface layer increases upon exposure to soluble gas. Figure 3.11 shows two voltammograms obtained with the same θ-pipet (cell 2) exposed to air (curve 1) and ammonia vapors (curve 2). As discussed above, the apparent potential window is extended by resistive effect, and the IT current in curve 1 is very low. In contrast, the large currents produced by transfers of TBA^+ from DCE to water (at negative ΔE) and Li^+ from water to DCE (at positive ΔE) in curve 2 indicate that absorbed ammonia caused a significant decrease in the film resistance. One should notice that the wave of ammonium transfer cannot be seen within the potential window in this experiment. The presence of NH_3 in the gaseous phase is detected by increasing transfer of supporting electrolyte and significantly higher charging current in the middle of the potential window. These currents are directly proportional to the solution conductivity which, in turn, is proportional to ionic concentration (the response may also have been affected by increasing pH as discussed below). Thus, the current flowing at a given potential depends strongly on ammonium concentration in the surface layer, and a θ-pipet can be used for monitoring relative concentration of ammonia in the gaseous phase. To measure absolute values of NH_3 concentration, the pipet sensor has to be calibrated.

Alternatively, the concentration of a gaseous compound can be found from the transfer current of an ion generated in the liquid film by species absorbed from the gaseous phase. For example, NH_4^+ formed in the aqueous layer when the θ-pipet is exposed to ammonia vapor can be transferred to DCE. This reaction can be facilitated by DB18C6 (Figure 3.12A):

NH_4^+ (aqueous film) + DB18C6 (DCE) → NH_4^+DB18C6 (DCE) (11)

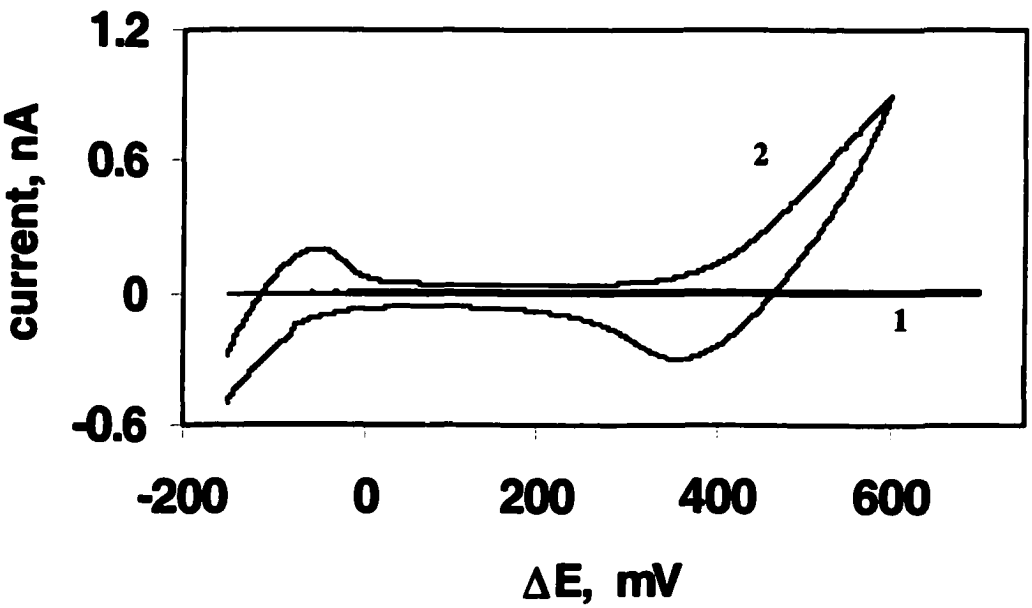

Figure 3.11. Effect of the exposure of a θ-pipet to ammonia vapor on the resistance of the aqueous film covering the gap between two barrels. (1) The pipet is in the air. The current is too small to be seen on the scale of curve 2. (2) The same pipet is exposed to a 1M solution of ammonia. v = 100 mV/s. The radii of the two orifices are 1 (water-filled pipet) and 1.5 μm (DCE-filled pipet). See cell 2 for solution compositions.

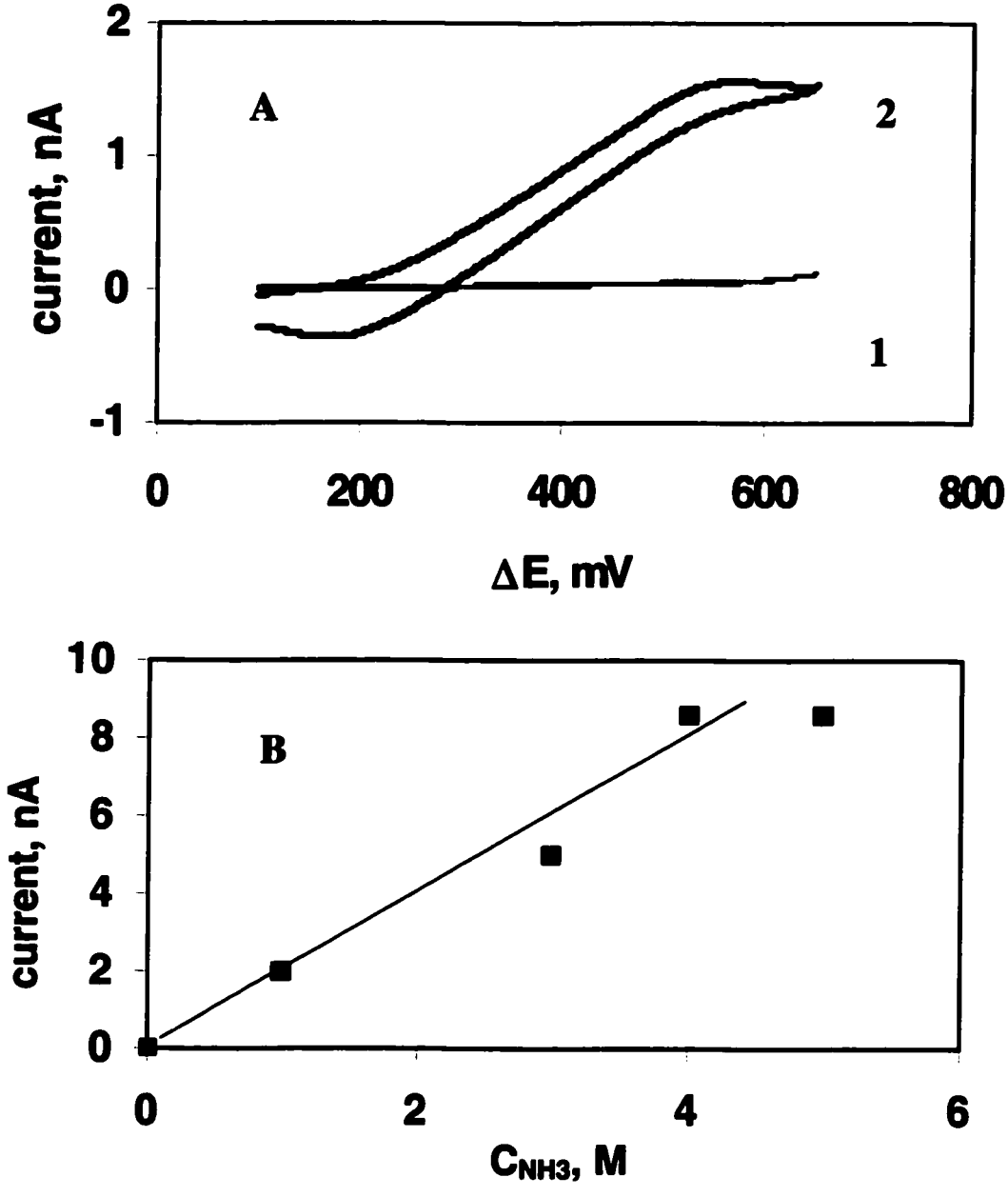

Figure 3.12. Detection of ammonia in the air. (A) Cyclic voltammograms obtained with a θ-pipet (cell 2 with 20 mM DB18C6 added to DCE) exposed to air (1) and ammonia vapor above its 2 M solution (2). (B) Dependence of voltammetric current at $\Delta E = 0.56$ V on concentration of NH_3 in the vapor-generating solution. v = 20 mV/s. The radii of the two orifices are 3 (water-filled pipet) and 1.5 μm (DCE-filled pipet).

The blank (background) curve obtained in the absence of ammonium ion (curve 1) is similar to one in Figure 3.10A. The wave of NH_4^+ appears immediately after the pipet is introduced in a vial containing ammonium hydroxide solution. The shape of the wave changes during next several minutes and then the response becomes stable and reproducible (curve 2 in Figure 3.12A). This time most probably reflects the dynamics of ammonia vaporization in a closed vial since the equilibration in a submicrometer-thick aqueous layer should be rapid. The wave of facilitated transfer (reaction 11) is sigmoidal while the reverse wave is peak-shaped. This means that the forward reaction is limited by convergent diffusion of NH_4^+ in the aqueous film to the orifice of the DCE-containing pipet. In contrast, the reverse peak is due to essentially linear diffusion of the NH_4^+DB18C6 complex inside the pipet containing DCE solution. Although the voltammogram is somewhat drawn out because of high film resistance, the diffusion limiting current is not affected by resistive potential drop and can be used for analytical determinations. The partial pressure of ammonia above the solution is expected to be proportional to its concentration when the latter is not very high. The diffusion limiting IT current measured at ΔE = 0.56 V applied to cell 2 increases linearly with concentration of ammonia in the vapor-generating solution at moderate c_{NH_3} values (Figure 3.12B). At c_{NH_3} > ~ 4 mol/L, the current vs concentration dependence levels off. This saturation may be caused by different reasons, e.g., deviations from Henry's law at high concentrations or extensive ion pairing inside the aqueous layer covering glass surface.

One should notice that the amount of analyte accumulated in the θ-pipet during described measurements is very small. In ~ 10 min after the pipet is removed from the ammonium atmosphere, "blank" voltammograms practically indistinguishable from curve 1 in Figure 3.12A could be obtained. Thus, the same pipet can be employed for a number of measurements or for continuous monitoring of a gaseous analyte. One also can use such a sensor for remote measurements of the concentration of a volatile solute in a liquid phase (i.e., without an electrochemical probe having to contact it).

Another example of IT-based sensing of a gaseous substance is shown in Figure 3.13. In this experiment, nitrate was accumulated in the aqueous film by exposing a dual pipet to HNO_3 vapor. In

this case, TBA^+ was replaced with THA^+ in the organic supporting electrolyte, so that nitrate ion transfer from water to

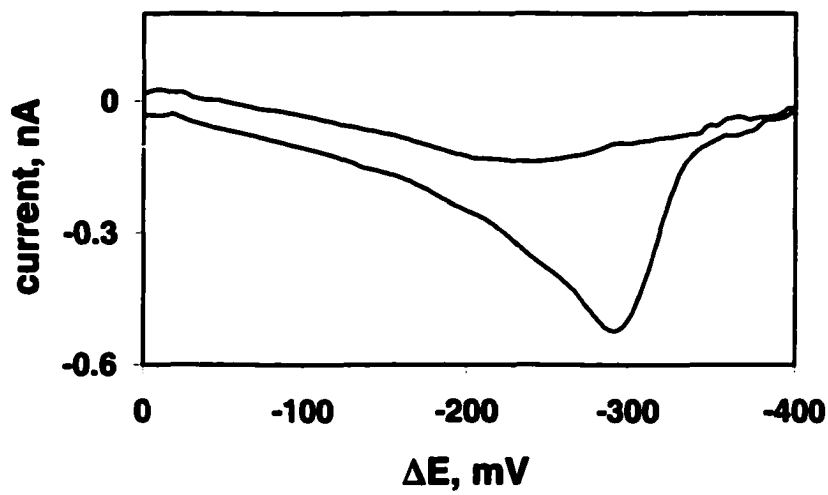

Figure 3.13. Background-subtracted voltammogram of nitrate transfer obtained with a θ-pipet (cell 2) exposed to a 1 M solution of nitric acid. v = 20 mV/s.

DCE occurred within the potential window. The voltammogram of nitrate transfer is peak-shaped and not as well defined as the one in Figure 3.12A. Moreover, the pipet seems to be more resistive, the wave is less

stable, and its height decreases with time. One of possible reasons for these differences is that absorption of HNO_3 makes the aqueous surface layer acidic while the exposure to NH_3 results in basic pH. The ion migration in the aqueous surface film is somewhat similar to capillary electrophoresis because a voltage drop of ~ 100 mV across a submicrometer gap between two orifices creates a large electric field. Since the film is only nanometers thick, the double-layer effect should be very important

[37]. This effect, in turn, depends on pH, which can affect the charge of the underlying glass surface [37]. The electrophoretic and electroosmotic mobilities of cationic NH_4^+ and anionic NO_3^- should also be different.

The conductivity-based detection of gaseous substances is more general than IT measurements because most soluble gases can affect film resistivity, but not all of them can be transferred across the ITIES. The advantages of IT detection include selectivity and somewhat higher sensitivity. The surface liquid layer in all pipets used in this work was aqueous, and only the detection of water-soluble gases was discussed. However, the detection of organic compounds in the gas phase may also be possible using a θ-pipet with a nonaqueous sensing film.

3.4 Conclusions

We have described electrochemical characterization of and voltammetric experiments with θ-pipet electrodes. Such a device consisting of two closely spaced micropipets is produced by pulling θ-shaped glass tubing. Voltammetric response of a dual pipet depends strongly on the extent of hydrophilicity of its outer surface. When a glass pipet is immersed in an organic solvent, its hydrophilic outer wall retains a submicrometer-thick aqueous layer. If both barrels of the pipet are filled with an aqueous solution, the surface water film links them producing a short circuit. The aqueous layer can be eliminated by silanizing the outer pipet wall to render it hydrophobic. The developed diagnostic procedures allow one to evaluate the adequacy of silanization.

Generation/collection measurements employing θ-pipets were used for probing charge-transfer processes at the liquid/liquid interface and homogeneous ionic reactions. Using this technique, concurrent IT reactions occurring at the ITIES can be quantitatively separated and the kinetics of homogeneous reactions involving ionic species can be probed. The upper limit for the determinable bimolecular rate constant is ~ 10^6 M^{-1} s^{-1} with currently available micrometer-sized pipets. Although this was not enough for measurements of rapid complexation of K^+ by DB18C6, it may be possible to

probe other ionic reactions such as binding of cations to DNA and polyelectrolytes. The fabrication of smaller θ-pipets will enable investigation of faster reactions and detection of short-lived intermediates.

Another mode of measurements is voltammetry "in air" in which a θ-pipet is not immersed in any external solvent and IT occurs in the nanometer-thick film of solvent linking its two barrels. This film acts as a microreactor and can be used to detect and quantitate various gaseous substances. In this way, IT voltammograms of NH_4^+ and NO_3^- were obtained when a pipet was exposed to vapors of ammonia and nitric acid, and linear dependence of the voltammetric response on concentration of vapor-generating solution has been demonstrated.

Chap IV

Scanning Electrochemical Microscopy of Living Cells

4.1. Introduction

Over the past 30 years, electrochemical methods have been developed for probing processes occurring in living cells (1-3). Single cell amperometry or voltammetry has focused on measuring the concentrations and monitoring the dynamic release of biologically important molecules such as catecholamines, insulin, and anti-cancer drugs from living cells (4-10). In such experiments, a micrometer-sized ultramicroelectrode (UME) is positioned in a close proximity of a cell membrane and used to oxidize (or reduce) the molecules ejected from the cell, to obtain information on cellular functions at single cell levels.

Recently, the scanning electrochemical microscope (SECM) has been used to study biological systems (11,12). In SECM, the tip is scanned over the surface of a cell to obtain topographic images and maps of chemical reactivity across the cell surface. In this way, SECM has been used to image fluxes of oxygen at living cells and to obtain topographic images of various biological substrates (13-16).

Unlike those works, the present work is focused on the measurements of electron transfer (ET) kinetics in single cells. Enzymatic redox reactions are essential for many cellular functions [metabolism, protein synthesis (17,18)]. It is well known that the energy production in living systems by respiration and photosynthesis is based on cellular redox reactions.

The cellular redox reaction is a complex multistep process that may include both transmembrane ion and electron transfers, as shown with model biomimetic systems [phospholipid membranes] (19-23). Previous measurements of interfacial redox activity typically employed large cell populations (24). Measurements with ultramicroelectrodes made at the level of a single cell are much faster and provide valuable information that is hard to extract from the averaged signal produced by a large number of cells. The fast response time also allows for detection of short-lived radicals such as reactive oxygen

species. A SECM that uses a scanning ultramicroelectrode probe is capable of mapping transmembrane charge transfer (CT) rates with high spatial resolution.

For the present work, we will use SECM-based approaches that were developed for liquid/liquid and solid/liquid interfaces (25-27), to investigate the pathway of transmembrane CT and to identify the factors limiting the overall CT rate. Another objective of the present study is to compare the intrinsic redox reactivity of cell types that exhibit different motile behaviors. This idea was prompted by observations (28, 29) that oxidants modulate the activity of protein kinase Cα (PKCα), an enzyme that has been linked with motility and metastasis of various cell types (30,31). Engineered expression of PKCα in non-motile MCF-10A human breast cells was found to engender a high degree of motility in those cells (11α cells), as previously described (32). Here, we use the SECM to measure and compare the redox reactivity of MCF-10A cells, 11α cells, and overtly metastatic MDA-MB-231 human breast cells. A mechanistic basis for the difference in the redox behavior of these cell types is explored in terms of PKCα function.

Another application of SECM explored in this work is imaging the topography and mapping redox and acid-base activities in single mammalian cells. The topographic images of cells were obtained using hydrophilic redox mediators, which cannot penetrate the cell membrane. In contrast, with a hydrophobic mediator one can map redox reactivity with a micrometer or submicrometer spatial resolution. Micrometer-sized Sb electrodes were used to monitor the efflux of acid and image pH profiles around a single cell.

4.2. Experimental Section

4.2.1. Chemicals

$Na_4Fe(CN)_6$, iodine, and KI were from Fisher Scientific (Fair Lawn, NJ). Menadione (General Biochemicals, Chagrin Falls, OH), 1,2-naphthoquinone (Aldrich, Milwaukee, WI), $Ru(NH_3)_6Cl_3$ (Strem Chemicals, Newburyport, MA) and other chemicals were reagent grade. All aqueous solutions

were prepared from deionized water (Milli-Q, Millipore Corp.).

4.2.2. Amperometric and Potentiometric Probes

A two-electrode setup was employed for both amperometric and potentiometric measurements. A 0.25-mm AgCl-coated Ag wire served as a reference electrode. Pt UME tips (12.5, 5, and 1-μm-radius) and carbon UME tips (5.5 and 3.5-μm-radius) were prepared as described in chapter II. Antimony potentiometric pH microprobes were fabricated similarly to those described in Ref. 33. A modification of that procedure was in drawing melted antimony into a Pyrex capillary (2 mm outer diameter, 1 mm inner diameter). The Sb-filled capillary was pulled using a helix heating coil. Fibers as small as 2-μm-diameter could be prepared by adjusting the coil temperature. The glass-coated antimony fiber was subsequently heat-sealed in a low melting point glass capillary under vacuum. The Sb UME was beveled, as usually done in the preparation of SECM tips [34] and polished with 0.05-μm alumina before each experiment. As shown previously [33], an antimony tip operated amperometrically at negative potentials regains its potentiometric response to pH after its potential is returned to 0 V vs. SCE for a few seconds.

4.2.3. Cell Culture

Mid-passage MCF-10A cells, a human breast epithelial cell line, were cultured in DMEM/F12 media (1:1) supplemented with 15% equine serum, insulin (10 μg/ml), epidermal growth factor (20 ng/ml), cholera toxin (100 ng/ml), and hydrocortisone (0.5 μg/ml), and maintained with penicillin (100 units/ml), streptomycin (100 μg/ml), and fungizone (0.5 μg/ml). Cells were passaged at 1:3 to 1:6 every 3 to 4 days. A stable transfectant clone (11α cells) that constitutively expresses bovine PKCα was isolated by neomycin-resistance, as previously described (35). Transfectants were maintained in complete growth medium containing 125 μg/ml G418, and cultured up to 20 passages. MDA-MB-231 cells were cultured in Iscove's Modified Dulbecco's Medium with L-glutamine, 10% fetal bovine serum, and 1% penicillin/streptomycin. Culture media, serum, and antibiotics (fungizone, penicillin, streptomycin) were purchased from GibCo-BRL (Rockville, MD). All other reagents were obtained

from Sigma Co. (St. Louis, MO).

Prior to each experiment, adherent cells that had been plated at low density in a 60-mm plastic culture dish, were washed with phosphate buffered saline (153 mM Na^+, 4 mM K^+, 1 mM Ca^{2+}, 1 mM Mg^{2+}, 144 mM Cl^-, and 10 mM phosphate, pH 7.4).

4.2.4. Instrumentation and Procedures

All measurements were performed at ambient temperature in a plastic culture dish mounted on a horizontal stage of the SECM. The cells were immobilized on the bottom of the dish and were immersed in phosphate-buffered saline (pH 7.4) containing the redox mediator at the specified concentration (Fig. 4.1). The SECM apparatus and procedure were the same as described in chapter II. In amperometric feedback mode, three types of experiments were performed: (i) the tip current (i_T) was recorded as a function of the tip position as the tip was moved laterally in a horizontal (x-y) plane a few micrometers above the cell surface; (ii) similarly, a gray scale image of the cell was obtained by recording variations in tip current while the probe was scanned in the x-y plane above the cell; and (iii) i_T vs. d curves were obtained by positioning the tip above the cell and slowly moving it vertically down to the cell surface (where d is the distance between the tip and the cell surface). The data were acquired using software generously provided by D. O. Wipf (Mississippi State University). The analysis of i_T - d curves was based on an earlier model developed for ET at the liquid/liquid interface (25).

Because of negative standard potentials of menadione and naphthoquinone mediators, the deaeration of solutions was necessary in experiments with those mediators. After finding an immobilized cell, a flow of nitrogen was quickly passed through a small volume (~5 mL) of aqueous solution covering the cells. The nearly complete removal of O_2 was evident from cyclic voltammetry. To prevent damage to the cells, oxygen was removed from the medium for a brief period (~ 10 min) that immediately preceded the actual measurements.

According to previously developed models (25-27,36), the rate of interfacial charge transfer should

appear immeasurably low if the concentration of redox species in solution is much higher than the intracellular concentration of redox centers. In previous SECM measurements, the concentration of the redox mediator in solution was typically in the millimolar range (37). In contrast, significantly lower (μM) concentrations have to be employed for experiments with living cells. The possibility of quantitative kinetic measurements with concentrations of redox species in solution as low as 10 μM was confirmed by fitting experimental current-distance curves obtained at both conductive and insulating substrates to the theory.

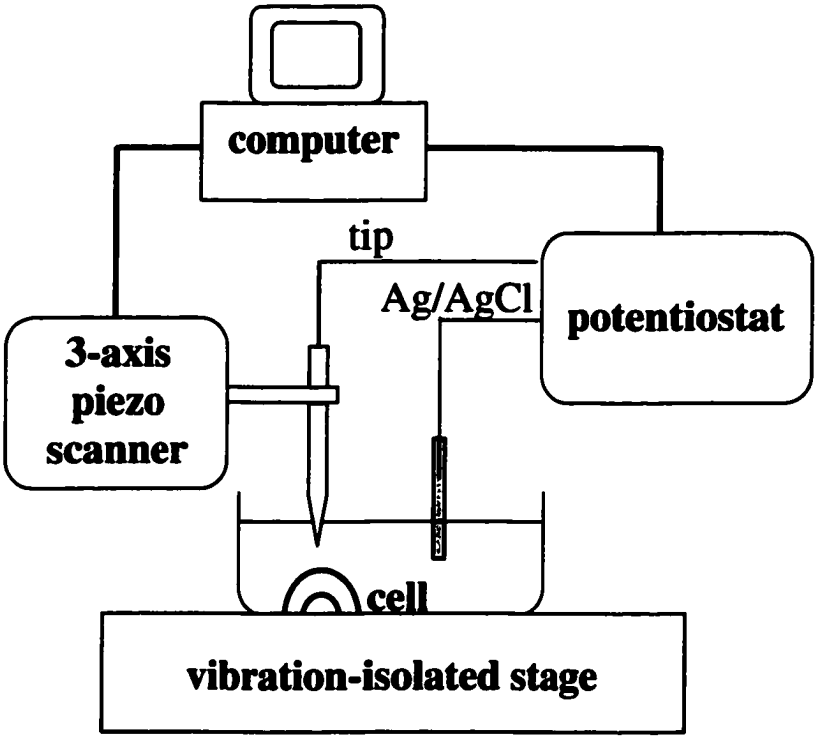

Fig.4.1. Schematic presentation of SECM measurements of living cells.

For pH imaging, the variations in Sb tip potential were measured using a high-impedance electrometer (Model 6512, Keithley Instruments, Cleveland, OH) while the probe was scanned in the x-y plane above the cell. The output of the electrometer was fed directly into one of the ADC channels to allow acquisition of the data by the computer. Voltammetric characterization of antimony electrodes was performed using a BAS 100B electrochemical workstation (Bioanalytical Systems, West Lafayette, IN). The pH calibration curves were obtained with a Fisher (Model 800) pH meter.

A proper choice of the buffer concentration was essential for pH imaging. In an unbuffered solution, the diffusion layer of protons released from a cell is very thick. This results in a significant "image broadening" (i.e., an enlarged image size compared to the cell dimensions) and the loss of spatial resolution [33]. When the buffer concentration is too high, the pH changes near the cell surface are small and hard to detect. A 2 mM buffer concentration was found suitable for cell imaging. Potentiometric tips were calibrated before and after each SECM experiment.

4.2.5. Assay of the cell viability

The SECM measurements of cells usually take 1 ~ 2 hours. To make sure that the cells maintain alive during the measurements, viability assay was performed by measuring SECM signal with a hydrophobic mediator in buffer. Figure 4.2 shows that the MCF-10A cells lost reactivity after about 3.5 hours. This time can be to evaluate the cell viability. Similar measurements were carried out for MDA-MB-231 and 11α cells, and both of the two cell types kept alive within 3 hours.

The cell viability was also determined by dyeing experiments. To simulate the SECM condition, the buffer solution in which the cells were immersed was continuously deaerated with nitrogen. Trypan Blue solution (0.4%, Sigma) was added to the buffer in a 1:1 ratio. Living cells are able to pump out the blue dye molecules, but dead cells cannot. Accordingly, dead cells look blue and living cells look unchanged in color under an optical microscope. In this way, the viability of the MDA-MB-231 and MCF-10A cells was found unchanged within 4 and 5 hours, respectively. The cells gradually died beyond this time scope. For MCF-10A cells, 20% and 50% cells became dead after 6.5 and 8 hr,

respectively. For MDA-MB-231 cells, 20% and 50% cells became dead after 5 and 7 hr, respectively.

4.3. Results and Discussion

4.3.1. The Pathway of the Transmembrane Charge Transfer Reaction

To investigate the pathway of the transmembrane CT reaction, SECM experiments were carried out with different types of redox mediators. When the tip was scanned horizontally above the cells in the presence of a hydrophilic redox mediator (e.g., ferrocene carboxylate), the tip current above the cell was significantly lower than that above the plastic surface (Fig. 4.3A). The cell surface thus impeded diffusion of the mediator to the tip (Figure 4.4A). Analogous results obtained with other hydrophilic mediators (e.g., $Ru(NH_3)_6^{3/2+}$, $Fe(CN)_6^{3/4-}$) show that no unmediated ET occurs across the cell membrane.

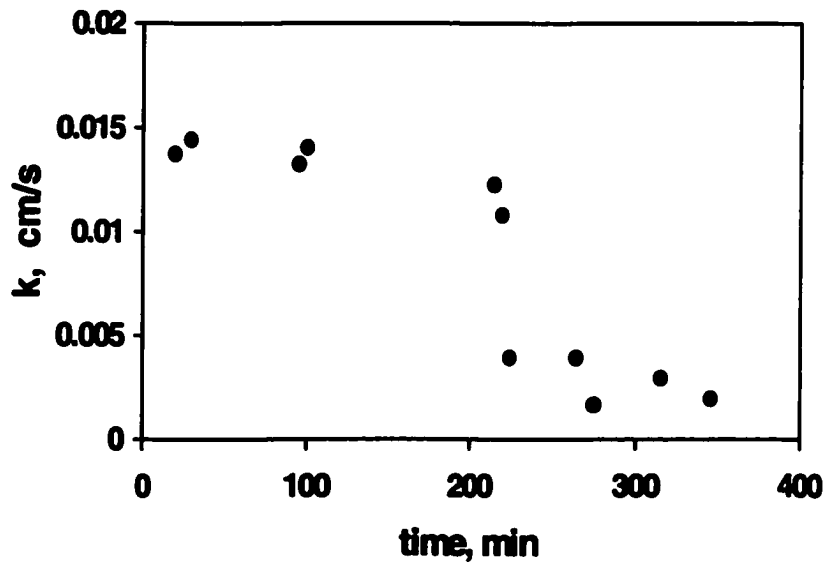

Fig. 4.2. The lifetime measurement of MCF-10A cells. Mediator: 30 μM 1,2-naphthoquinone in phosphate buffer (pH 7.4). The tip: 5.5-μm-radius carbon fiber.

By contrast, with a lipid-soluble mediator (e.g., menadione or 1,2-naphthoquinone), the i_T increased

when the tip was scanned horizontally above the cell (Figure 4.3B). Both oxidized and reduced forms of menadione

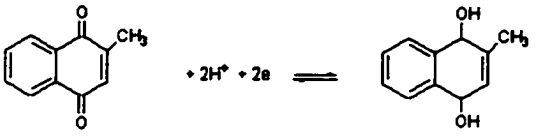

and 1,2-naphthoquinone

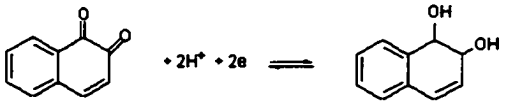

are neutral and can cross the cell membrane [38]. Thus the increase in the I_T above the cell in Fig. 4.3B can be explained either by intracellular oxidation of the reduced mediator species (menadiol) generated by the tip reaction (Figure 4.4, C and D), or by diffusion of menadione from a preaccumulated intracellular pool (Figure 4.4B). Whatever the mechanism, I_T reflects the overall rate of menadione regeneration by the cell.

The apparent rate constant of the mediator regeneration process, k, can be extracted from the dependence of the normalized current (I_T) vs. the normalized distance (d/a) between the tip and the cell (where a is the tip radius). The data obtained with a tip approaching the plastic surface of the culture dish (curve 1 in Figure 4.5A and 4.5B) fit the theory for an insulating substrate (solid line). When the same tip approached an MDA-MB-231 cell (metastatic cell) (curve 2), the I_T was higher, indicating that the mediator was regenerated by the cell at a measurable rate. The effective heterogeneous rate constant, $k = 2 \times 10^{-3}$ cm/s, was obtained by fitting this curve to the SECM theory (solid line). The tip current for a MCF-10A cell (non-metastatic cell) (curve 4) was significantly higher than the I_T obtained for an MDA-MB-231 cell (curve 2), resulting in $k = 3.8 \times 10^{-3}$ cm/s. Thus, a non-metastatic

cell regenerates menadione at a significantly higher rate than does a metastatic cell. For an 11α cell (MCF-10A cell that overexpresses PKCα), the rate constant (k = 2.1 $\times 10^{-3}$ cm/s from curve 3) was slightly higher than the k value for an MDA-MB-231 cell, but significantly lower than that for a MCF-10A cell.

The rate of the multistep reaction underlying the observed SECM response can be influenced by a number of factors including: (i) the rate of intracellular ET, which is governed either by the intracellular redox potential or concentrations of redox species; (ii) the rate of mass/charge transport across the membrane; and (iii) the mediator diffusion in solution. However, the intracellular redox potential is not the rate-limiting factor for any reaction in Figure 4.5. If it were limiting, the effective rate constants for 1,2-naphthoquinone (Fig. 4.5B) would be much lower than for menadione (Fig. 4.5A) because the standard potential of menadione is ~170mV more negative than that of 1,2-naphthoquinone. However, the k values extracted from the approach curves for 1,2-naphthoquinone are somewhat higher than those determined for menadione (Table 4.1).

Table 4.1. Dependence of the heterogeneous rate constant measured for MCF-10A cells on the redox potential of hydrophobic mediators

Redox species in solution (30 μM)	$E_{1/2}$, mV vs. Ag/AgCl	k, $\times 10^{-3}$ cm/s
menadione	-380	2.9 ± 0.2
1,4-naphthoquinone	-320	11 ± 0.8
1,2-naphthoquinone	-207	14 ± 1.1

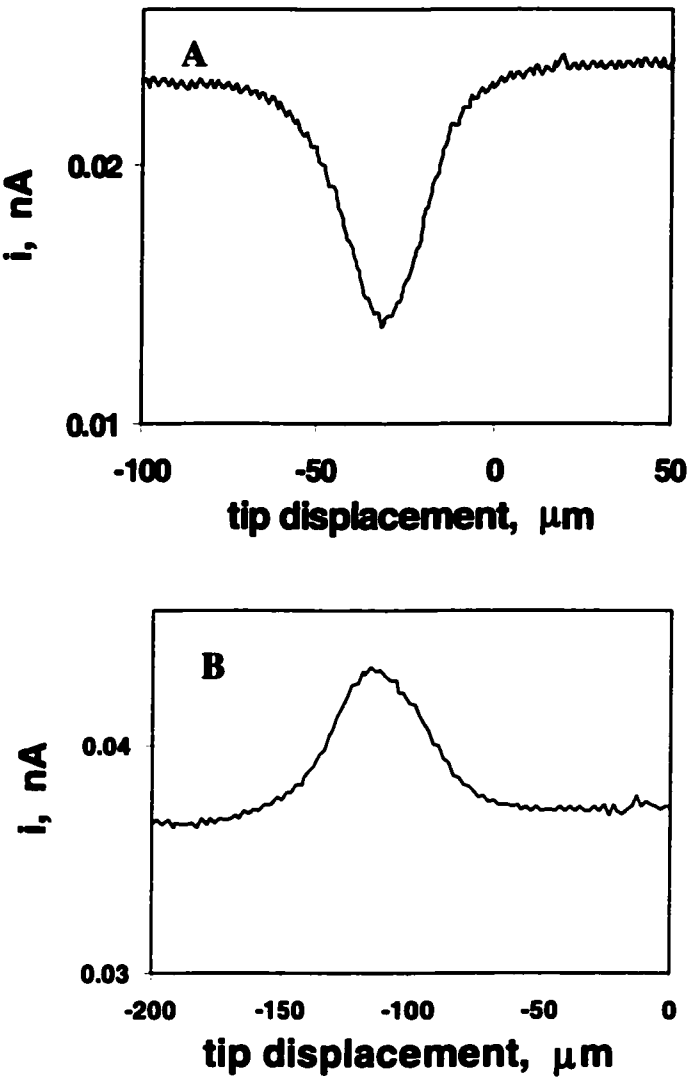

Fig. 4.3. Current vs. tip position dependencies for an SECM tip scanned laterally over a MCF-10A cell in solution containing (A) 50 μM FcCOONa and (B) 40 μM menadione. The tip radius is 5.5-μm.

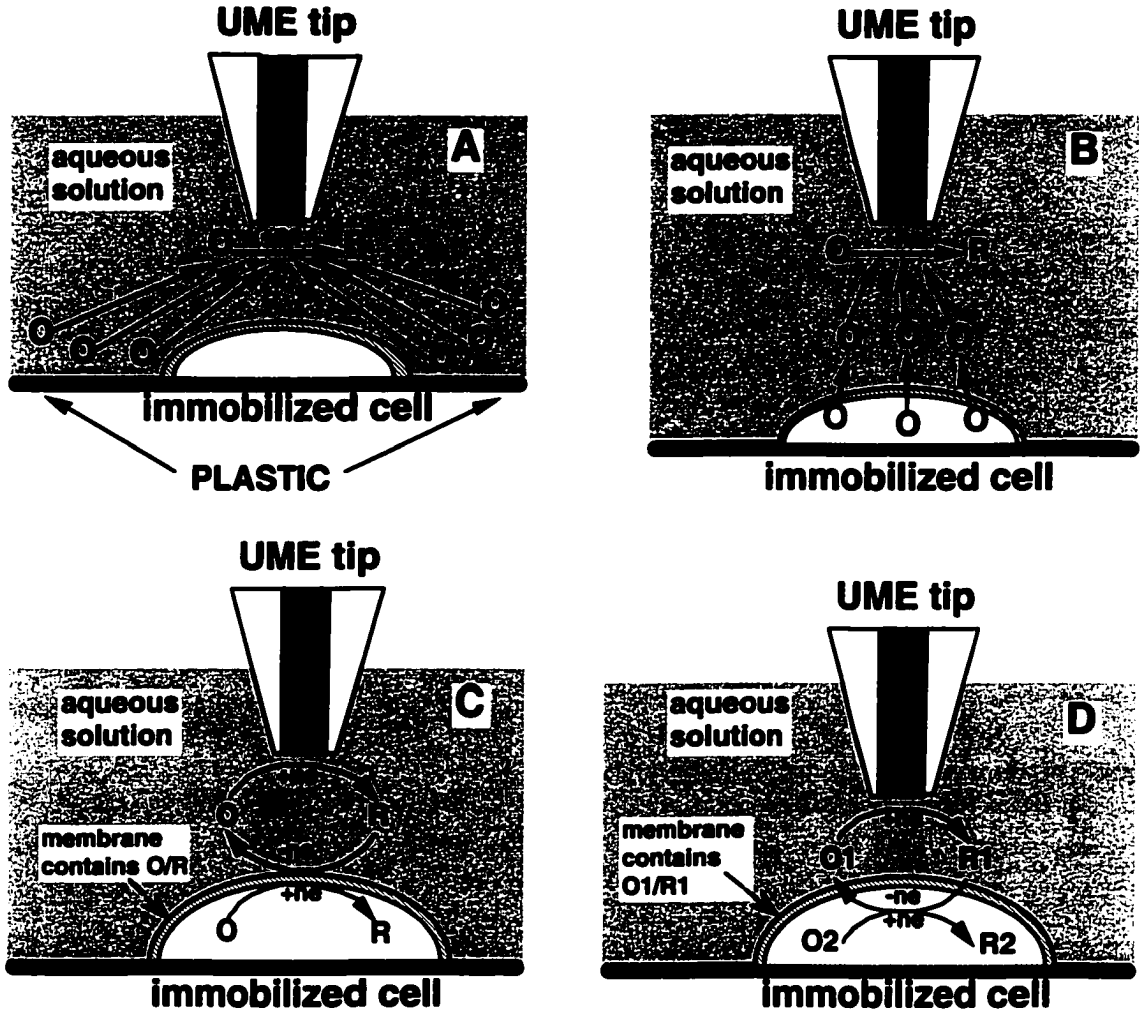

Fig. 4.4. Schematic diagrams of the SECM experiments with four different types of mediator regeneration. (A) The tip is positioned in the solution close to the cell surface. The lipid cell membrane is impermeable for a hydrophilic redox mediator. Negative feedback is due to the hindered diffusion of redox species to the tip electrode. (B) The ultramicroelectrode tip induces the ejection of the redox species, O, from the cell by depleting its concentration near the cell surface via electrolysis. (C) Mediator regeneration proceeds via self-exchange ET reaction. The charge is shuttled across the membrane by the same hydrophobic redox species (O/R). (D) Bimolecular ET between hydrophobic redox mediator (O1/R1) and cell-bound redox moieties (O2/R2).

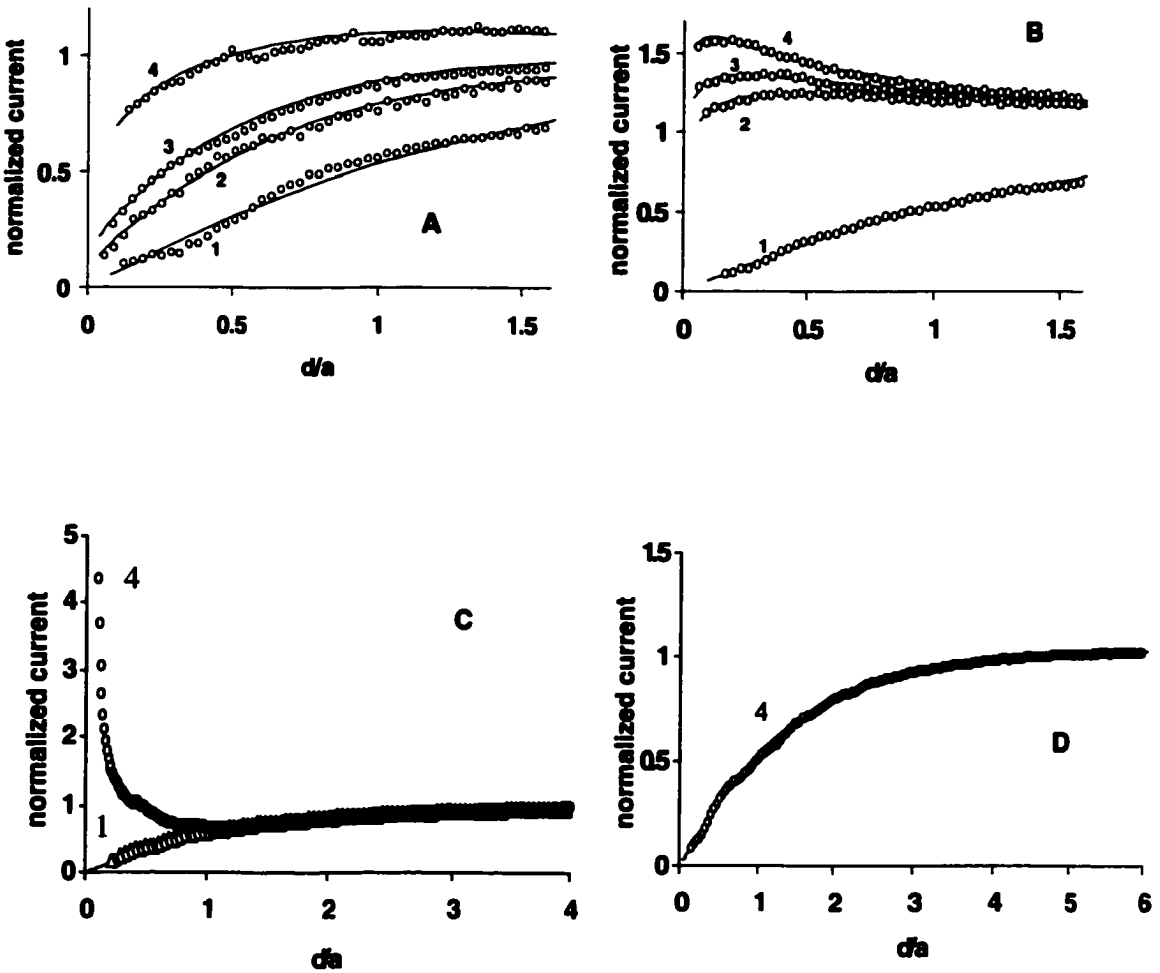

Fig. 4.5. An UME tip approaches (1) plastic surface, (2) MDA-MB-231 cell, (3) 11α cell, and (4) MCF-10A cell. Solid lines are the theoretical curves for an insulating substrate (1) and finite heterogeneous kinetics (2, 3, 4). Phosphate buffer (pH 7.4) contained (A) 20 μM menadione, (B) 30 μM 1,2-naphthoquinone, (C) 0.1 mM KI, and (D) 0.1 mM KI + 20 μM I_2. (C) Curves for MDA-MB-231 and 11α cells were very similar to Curve 4. (D) Curves 1-4 were essentially identical. The tip current is normalized by the i_T value measured in the bulk solution. The tip was 5.5-μm-radius carbon fiber (A and B), and 5-μm-radius Pt (C and D).

In contrast to quinone mediators, the standard potential of the I_3^-/I^- couple is more positive. In this case, I^- is oxidized to I_3^- by the tip, and I_3^- enters the cell where it is reduced to I^-. Because I^- cannot permeate the cell membrane, the CT pathway is easier to identify. According to the mode previously developed for ET at liquid/liquid interfaces (25-27), the high current in Figure 4.5C indicates that the rate of I_3^- reduction to I^- in all three cell types is essentially diffusion-controlled and almost identical. In curve 4 of Figure 4.5C, I_T at the cell surface ($d/a<<1$, where a is the tip radius) is almost five times higher than the bulk solution. This is possible only when the intracellular concentration of a reducing agent is at least ten times the concentration of I^- in solution (25-27). It is not likely therefore that this reducing agent is I^-. The addition of a low concentration of I_2 to the I^- solution quenches the regeneration of I^- by the cell, as shown by a drastic decrease in I_T (Figure 4.5D). In this case, I_3^- enters the cell and depletes the intracellular concentration of a redox component responsible for I^- regeneration. This greatly diminishes the rate of I^- regeneration by the cell (Figure 4.5D). This effect would not be observed if either diffusion of preaccumulated I^- from the cell (Figure 4.4B), or a self-exchange mechanism (Figure 4.4C) were responsible for regeneration of I^-. Rather, this result is consistent with a bimolecular ET mechanism involving some intracellular reducing agent (Figure 4.4D). Additional support for this model comes from I_T vs. time dependence (Figure 4.6). The curves in Fig. 4.6 are obtained by positioning a tip in a close proximity of the cell, keeping it at rest potential for a few minutes, and then switching the tip potential to the value corresponding to diffusion-controlled reduction (or oxidation) of the redox mediator. The tip current is recorded as a function of time. Curve A was obtained in solution containing relatively high concentration (0.1 mM) of iodide, which was oxidized at the tip. Immediately after the application of a positive potential to the tip positioned near the cell surface, i_T is low because the membrane is impenetrable to I^- and contains no species capable of shuttling the charge. When I_2 that is produced by the tip accumulates in the membrane, the i_T increases sharply. An increase in conductivity by I_2 was previously observed in lipid bilayers (23). A subsequent slow decrease in i_T points to the depletion of an intracellular reducing species responsible for reduction of iodine.

For quinone mediators such as 1,2-naphthoquinone or menadione, no initial increase in i_T with time is observed (Figure 4.6B) because both oxidized and reduced forms can enter the cell to react with the intracellular redox agents, and no accumulation of mediator in the membrane is required for charge shuttling. The increase in the tip current immediately after the application of a negative potential to the tip positioned near the cell surface is due to the bimolecular ET reactions involving some intracellular oxidizing agent (additional evidence for this model is given below).

The current vs. time dependencies can be used to evaluate the amounts of redox moieties contained in the cell. When the concentration of redox species in solution is sufficiently high (as in Fig. 4.6), within a few minutes after the potential step the tip current decreases to the value corresponding to pure negative feedback. This means that the intracellular redox centers responsible for regeneration of the mediator have been completely eliminated by mediator species produced at the tip. This was confirmed by pure negative feedback obtained immediately after the current vs. time was recorded (Fig. 4.7). The total amount of those redox centers initially present in the cell can be evaluated by integrating the tip current vs. time dependence (the shaded area shown in Fig. 4.6). The intracellular concentrations of redox species measured with different mediators are shown in Table 4.2.

The data in Table 4.2 indicate that the intracellular concentrations of a species capable of oxidizing menadiol measured with different quinone mediators (i.e., menadione, 1,2-naphathoquinone, 1,4-naphathoquinone) were nearly the same for the same cell type, and the concentration of the intracellular oxidants is higher in MCF-10A cells than in MDA-MB-231 cells. Table 4.2 also shows that the intracellular concentration of a species capable of oxidizing menadiol is much lower than the concentration of the component reducing I_2. This conclusion is consistent with a much lower current in Figures 4.5A and 4.5B as compared to Figure 4.5C. The availability of an intracellular oxidant is apparently the rate-limiting factor for menadione and 1,2-naphthoquinone mediators. This can be further supported by the fact that an increase of menadione concentration in solution resulted in a marked decrease in the apparent rate constant of CT (Fig.4.8). According to earlier models developed for the bimolecular ET at the liquid/liquid interface (25-27,36), this observation suggests that a

bimolecular ET mechanism (Figure 4.4D) is in effect rather than simple diffusion of menadione from the cell (Figure 4.4B), or a self-exchange reaction (Figure 4.4C). According to the earlier models, the normalized feedback tip current depends on the ratio of the concentrations of the redox species in the two phases, C_2/ C_1, where C_1 and C_2 are the concentrations of the reactant in the top and bottom phases, respectively. When $C_2/ C_1 > 10$, the feedback current does not depend on C_1. When $C_2/ C_1 < 10$, the feedback current decreases as C_1 increases. In the case of $C_2/ C_1 > 10$, the deletion of the reactant in the bottom phase is less significant. Accordingly, the diffusion of the reactant in the bottom phase is not the rate-limiting factor, and the kinetics of the heterogeneous ET process is controlled by either the diffusion of the redox species in the top phase or the ET across the interface. When $C_2/ C_1 < 10$, the deletion of the reactant in the bottom phase become significant, and the diffusion of the reactant in the bottom phase can be the rate-limiting step.

Table 4.2. The intracellular concentrations of the redox species responsible for the mediator regeneration (10^{-14} mole/cell)[a]

mediator	$E_{1/2}$, mV vs Ag/AgCl	Intracellular Reaction	MCF-10A	MDA-MB-231
KI	500	reduction	11 ~ 12	3.6 ~ 8.9
1,2-naphathoquinone	-207	oxidation	0.8 ~ 1.3	0.5 ~ 0.8
1,4-naphathoquinone	-320	oxidation	0.9 ~ 1.5	0.5 ~0.9
menadione	-380	oxidation	0.7 ~ 1.1	0.5 ~ 0.6

[a] The data were obtained by integrating the current vs. time curves. The mediator concentration was 100 μM.

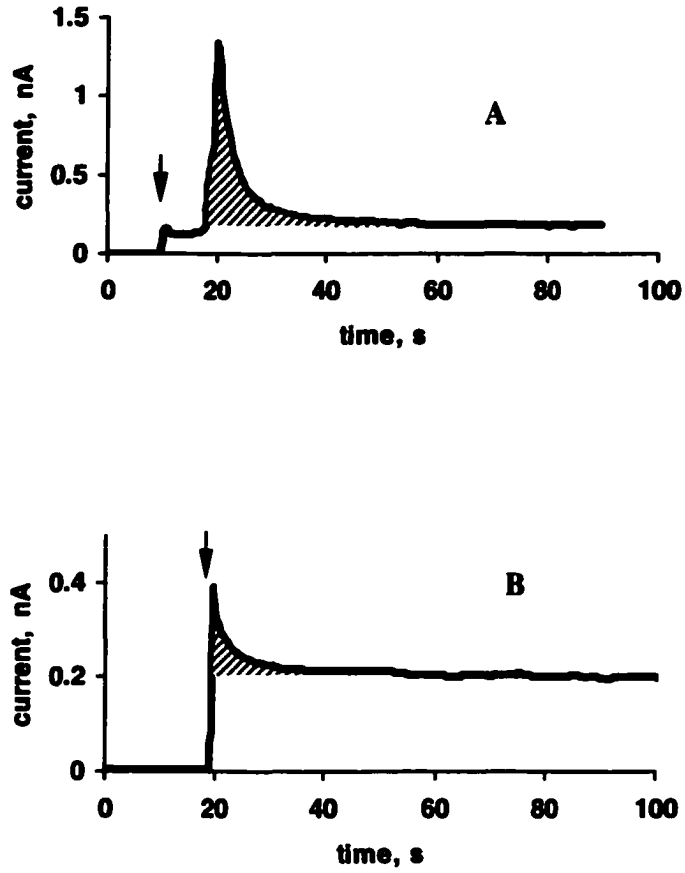

Fig. 4.6. Current vs. time dependencies obtained at an ultramicroelectrode tip positioned at a constant distance (about 5 μm) above a MCF-10A cell. Solution contained (A) 100 μM KI and (B) 100 μM menadione. Tip potential was (A) 0.64 V and (B) -0.44 V vs Ag/AgCl reference. The arrow indicates when the potential was applied. The tip was (A) 5-μm-radius Pt, and (B) 5.5-μm-radius carbon fiber.

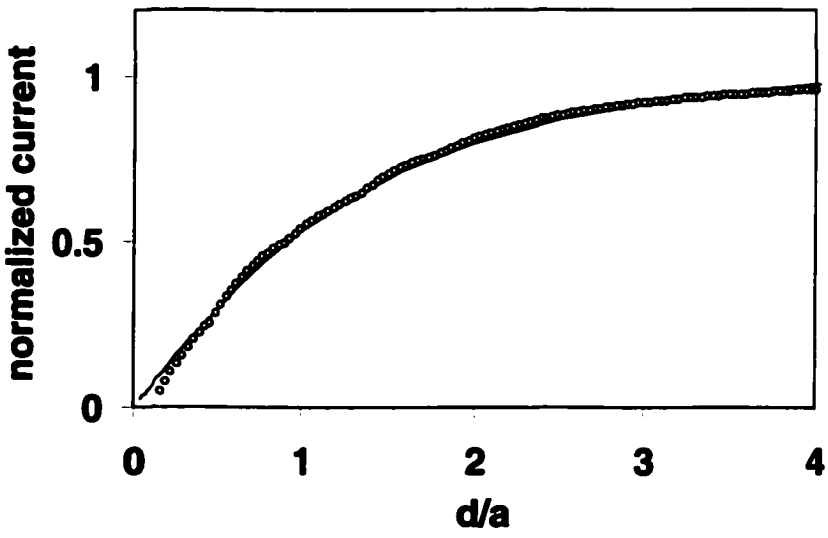

Fig.4.7. Approach curve recorded after obtaining a current vs. time curve (400 s). Points – experiment; Solid line – theory for an insulating substrate. Cell: MCF-10A cell. Mediator: 100 μM menadione. Tip: 5.5-μm-radius carbon.

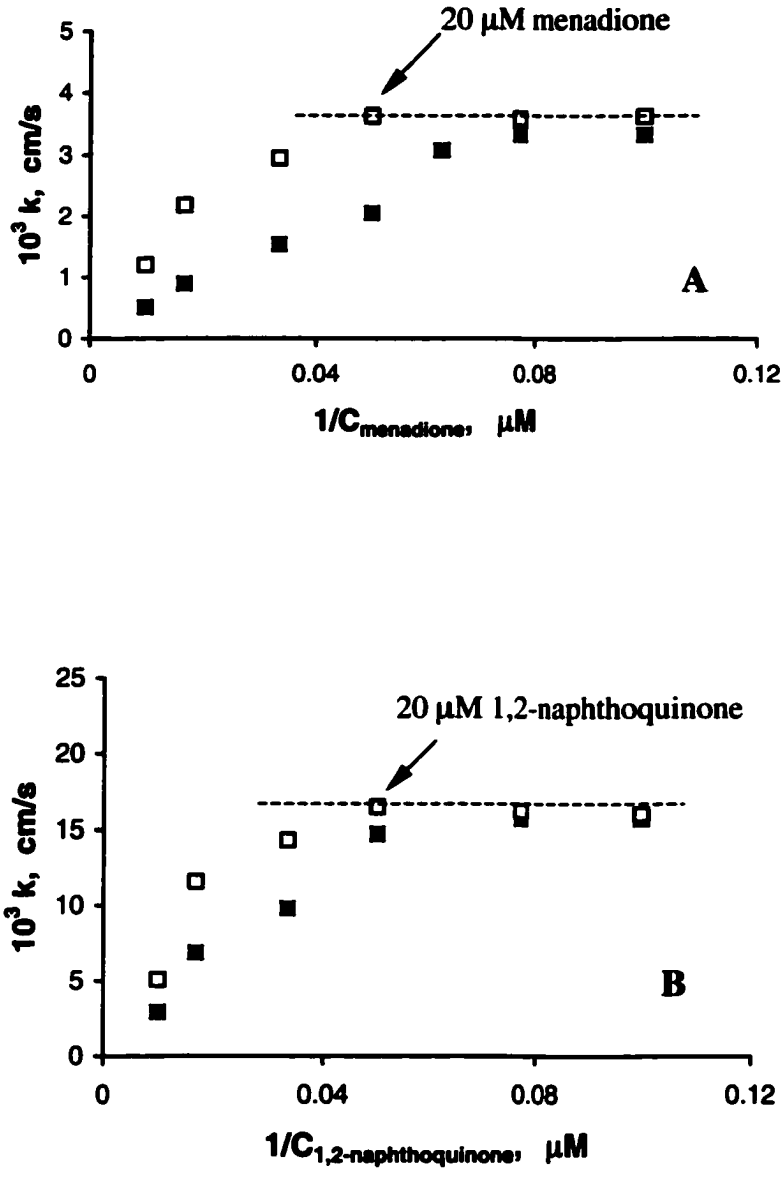

Fig. 4.8. Concentration dependence of the effective heterogeneous rate constant for MCF-10A (□) and MDA-MB-231 (■) cells. The mediator was (A) menadione and (B) 1,2-naphthoquinone.

The transmembrane charge transfer in cells is similar to the charge transfer process across the liquid/liquid interface. In fact, the liquid/liquid interface has been suggested as a simple model for biological membranes (20,39,40). Fig. 4.8 indicates that for MCF-10A cells, the CT rate constant is independent of the mediator concentration as the concentration of the quinone mediator is smaller than 20 μM. When the mediator concentration is larger than 20 μM, the rate constant decreases with increasing mediator concentration. A lower transition concentration (~ 13 μM) was found for MDA-MB-231 cells (solid squares in Fig.4.8). According to the model discussed above, when the mediator concentration in the aqueous solution is low (e.g., < 20 μM for MCF-10A cells), the rate-limiting step of the heterogeneous redox reaction can be either mediator diffusion in the aqueous solution or the mediator transport across the cell membrane. Fig. 4.5 has shown that for quinone mediator the charge transfer is not diffusion controlled. Otherwise, the feedback current in Fig 4.5A and 4.5B would be much higher (compare to diffusion controlled current shown in Fig 4.5C). Therefore, the mediator transport across the cell membrane should be rate-limiting step at low mediator concentration. If this is the case, we can expect that at low mediator concentration, the values of the rate constants obtained for both MCF-10A and MDA-MB-231 cells are identical for the same mediator because the two cell types are all human breast cells and similar to each other in their membrane structures, and thus have similar membrane permeability. This is supported by the data shown in Fig.4.8. At low mediator concentration (i.e., < 20 μM for MCF-10A cells; < 13 μM for MDA-MB-231 cells), nearly the same values of the rate constants were obtained for MCF-10A and MDA-MB-231 cells for the same mediator (Fig. 4.8A and 4.8B).

The plateau value in Fig 4.8B (~ 15×10^{-3} cm/s) is higher than in Fig 4.8A (~ 4×10^{-3} cm/s), which suggests that the transmembrane transport rate of 1,2-naphthoquinone is higher than that of menadione. The difference may be due to the different structures of the two mediators. The methyl group in a menadione molecule makes it bulkier than a 1,2-naphthoquinone molecule, and presumably makes it more difficult to transfer across the membrane than a 1,2-naphthoquinone molecule does. It is well known that permeability across biological membranes and model lipid bilayers depends strongly on the

size of the permeating solute (41-43). For instance, permeability across lipid bilayers was found to decrease with increasing chain length for short-chain monocarboxylic acids (44).

According to the model discussed above, when the concentration of the intracellular redox reactants is about 10 times larger than that of the quinone mediators in aqueous solution, the rate constant of the mediator regeneration will not depend on the mediator concentration. This criterion can be used to evaluate the concentration of the intracellular redox agents for the cells studied. Fig. 4.8 show that for MCF-10A cells, when the extracellular quinone concentration is small than 20 μM, the rate constant does not vary with the quinone concentration any more. Thus, the intracellular concentration of the redox agents that can oxidize menadiol in a MCF-10A cell is about 200 μM. Similarly, the intracellular oxidant concentration in an MDA-MB-231 cell was found to be about 130 μM.

The concentrations of the intracellular redox agents can also be evaluated from the transient measurements (table 4.2). The diameter of the cells studied in this research is about 50 μm. Based on the data measured with quinone mediator in table 4.2, the volumetric concentrations of the intracellular oxidant can be calculated assuming the cell is hemisphere-shaped (table 4.3). The data in table 4.3 indicate that the intracellular oxidant concentrations obtained from the steady-state measurements are consistent with the results obtained from transient measurements.

Table 4.3. The intracellular concentrations of the redox species responsible for the regeneration of the quinone mediators.

Cell Type	intracellular concentration (μM)	
	steady-state	transient
MCF-10A	200	230 ~ 360
MDA-MB-231	130	160 ~ 200

At high concentration of the extracellular mediator, the rate of the transmembrane mass transport increases, and the availability of an intracellular redox species becomes important. When the mediator

concentration is sufficiently high, the transmembrane mass transfer is not rate-limiting, and the kinetics of the overall CT process should be controlled by the intracellular redox reactions. In this case, the rate constant depends on the intracellular concentration of the redox species. The preceding data indicate that for quinone mediators, the intracellular oxidant concentration of a MCF-10A cell is about 1.5 times larger than that of an MDA-MB-231 cell. Accordingly, it can be expected that at high quinone concentration the CT rate constant measured for a MCF-10A cell should be larger than that measured for an MDA-MB-231 cell. This postulation is supported by the data shown in Fig. 4.8. The ratio of the CT rate constants for MCF-10A cells and for MDA-MB-231 cells, k_{10A}/k_{231}, calculated with the data in Fig. 4.8 was summarized in table 4.4, which clearly shows that at high mediator concentration, the CT rate constant of MCF-10A cells is larger than that of MDA-MB-231 cells.

Table 4.4. The effect of the mediator concentration on the difference in CT rate between MCF-10A cells and MDA-MB-231 cells.

mediator concentration, μM	k_{10A}/k_{231}	
	1,2-naphthoquinone	menadione
10	1.0	1.1
20	1.1	1.8
30	1.5	1.9
60	1.7	2.4
100	1.7	2.4

Living cells typically contain numerous redox couples such as NAD$^+$/NADH, NADP$^+$/NADPH, cystine/cysteine, and the oxidized and reduced forms of glutathione and metalloenzymes. Menadione and menadiol can react with multiple cellular substrates. The lower level of some unknown oxidizing species in metastatic cells as compared with MCF-10A cells may stem from the differing metabolism,

which is largely determined by the intracellular enzymatic activities. To explore the biochemical basis for the difference in redox activities between the normal and cancer cells, we performed the SECM measurements of cells with different enzymatic activities. The results are presented in the next section.

4.3.2 Correlation between Cellular Redox Response and Intracellular Enzyme Activity

Despite small quantitative differences in the SECM data obtained with individual cells of the same type, the lower oxidizing activity of 11α and MDA-MB-231 cells relative to MCF-10A cells was highly reproducible with different SECM tips and with different lipid-soluble mediators (Fig.4.9).

Because quinones can react with multiple cellular substrates, pinpointing the biochemical reactions responsible for these SECM signals is challenging. One possible approach to this problem is to study genetically engineered cells which either lack or overexpress key enzymes. This approach was taken in this research.

Compared with MCF-10A cells, both 11α and MDA-MB-231 cell lines are highly motile and exhibit slower proliferation rates (35). For 11α cells, the slower proliferative rate was the direct outcome of protein kinase Cα (PKCα) overexpression (35). PKCα is a redox-active enzyme that participates in growth signaling pathways. It has been linked with the metastatic behavior of several cell types including melanoma, intestinal and breast cells (30,31,35). PKCα itself is known to undergo redox reactions (28). This serine/threonine monomeric protein kinase exists as a family of highly related isoforms that are variously expressed in all tissues. The discovery in 1982 that PKC is a major receptor for phorbol esters, which is known to promote the occurrence of tumors, immediately cast this enzyme in a pivotal role in carcinogenesis and identified it as a potential target for anti-cancer drug design (29).

Since both 11α and MDA-MB-231 cells express high levels of PKCα. Figure 4.9 seems to reveal the interplay between PKCα expression and cellular redox activity. This idea was supported by the following SECM measurements of cells with different PKCα activities. In these experiments, the

PKCα activity was modulated either by the engineered expression of PKCα mutant proteins or by the addition of small molecule PKCα inhibitors.

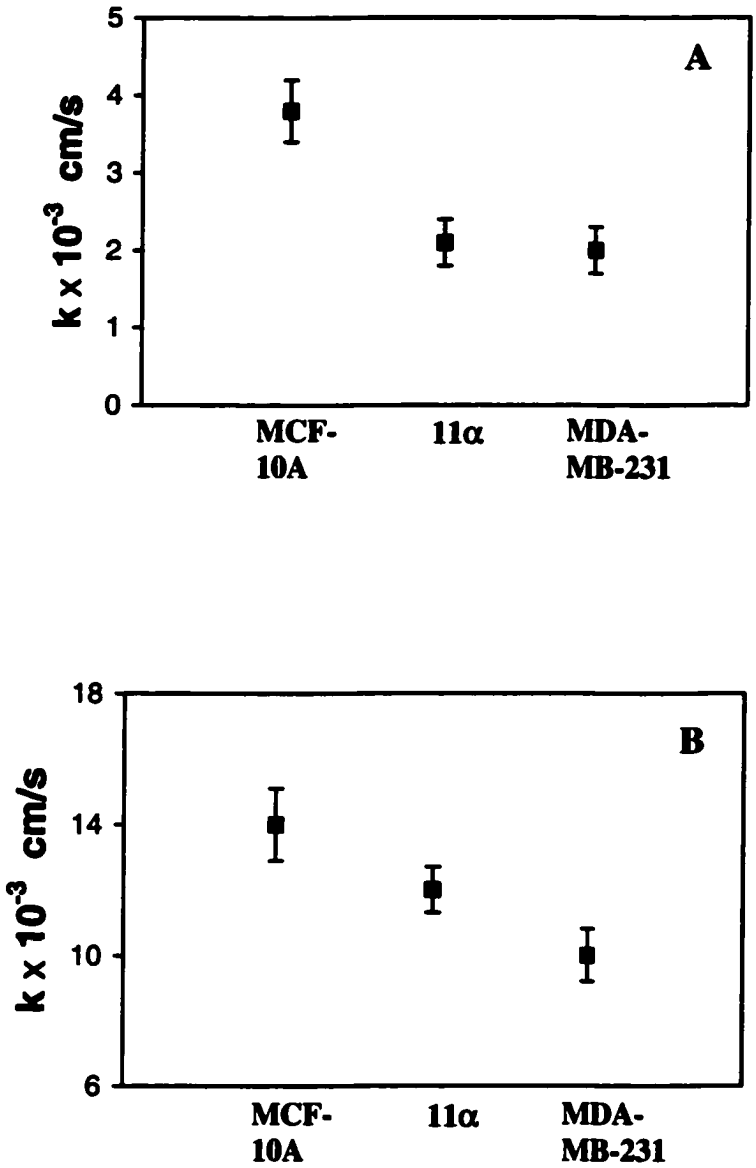

Fig. 4.9 Variability of heterogeneous rate constants measured for different cell lines. The mediator was (A) 20 μM menadione; (B) 30 μM 1,2-naphthoquinone. The shown uncertainties are 95% confidence intervals.

We first examined MCF-10A cells transfected with a PKCα expression plasmid and a control plasmid. After the transfection, MCF-10A cells express higher levels of PKCα. Fig. 4.10 clearly shows that PKCα overexpression in MCF-10A cells resulted in a decrease in the rate of the mediator regeneration.

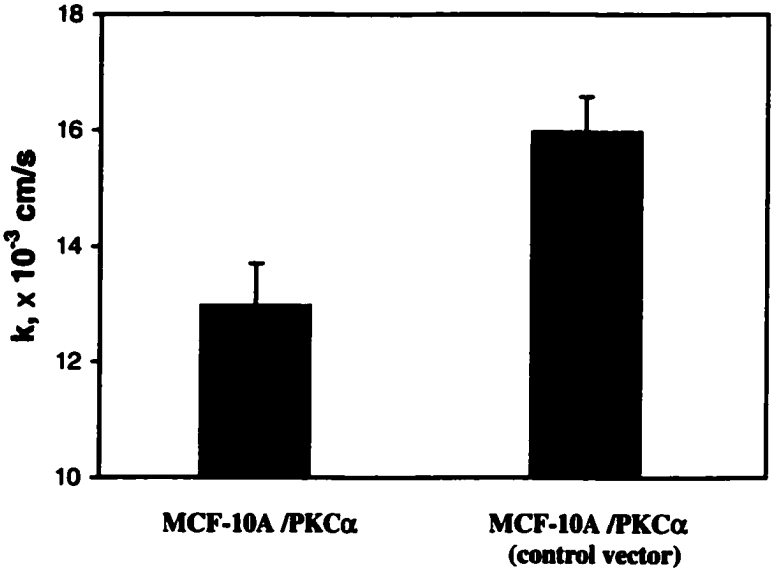

Fig. 4.10 The Effect of PKCα expression on the redox activity of cells.

Mediator: 30 μM 1,2-naphthoquinone

In another experiment, a kinase-defective mutant of PKCα (in which the ATP-binding lysine residue in the active site has been replaced with an arginine residue) was overexpressed in MCF-10A cells. The overexpressed PKCα was catalytically inactive since it cannot to bind ATP, which is required for catalysis. The kinase-defective PKCα-expressing cells and the control cells (which have low level of PKCα) showed nearly identical redox responses (Fig. 4.11). This finding identified PKCα catalytic activity as critical to cellular redox properties.

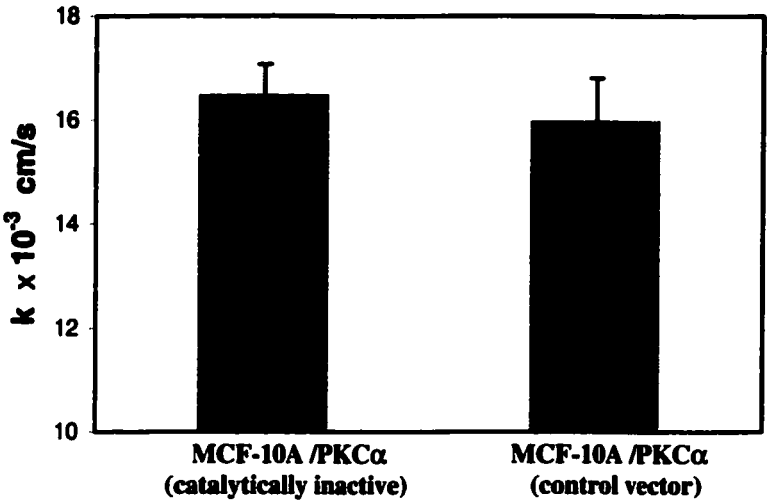

Fig. 4.11 The Effect of the catalytic activity of PKCα on the redox activity of cells. Mediator: 30 μM 1,2-naphthoquinone

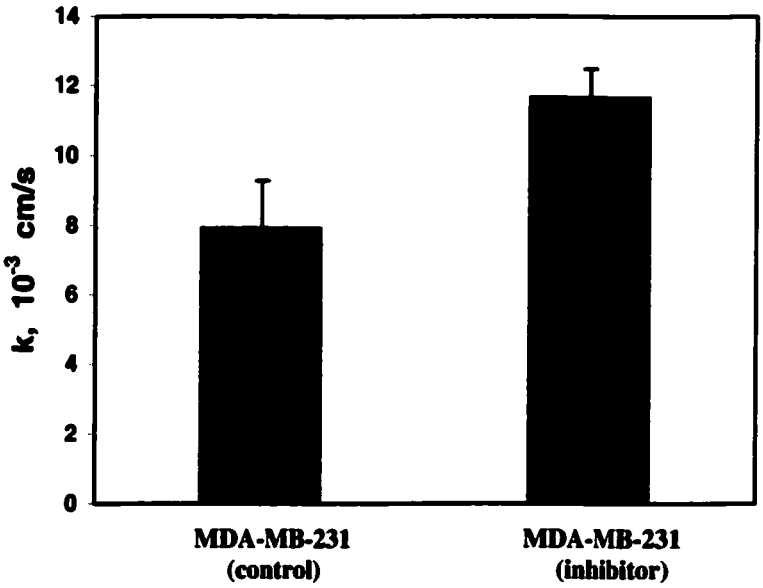

Fig. 4.12 The Effect of PKCα activity on the redox activity of cells. The MDA-MB-231 cells were treated with 1 μM Gö6976. Mediator: 30 μM 1,2-naphthoquinone.

Next, we performed the SECM measurement of MDA-MB-231 cells treated with indolocarbazole Gö6976, a specific inhibitor of PKCα (45). The highly-specific PKCα inhibitor is targeted to the active site of the catalytic domain of the enzyme. Accordingly, the treatment of MDA-MB-231 cells with Gö6976 lowered the catalytic activity of PKCα in the cells, and increased the SECM signal (Fig. 4.12). This finding confirmed the active role of PKCα in suppressing the cellular redox activity.

The preceding data indicated that intracellular oxidation of the quinol to the quinone occurred more slowly in the PKCα-overproducing cells and metastatic cells than in non-metastatic cells. This outcome is consistent with a lower level of oxidizing species in metastatic cells as compared with MCF-10A cells (see last section). The reason for this result may stem from the overall decrease in metabolism (lower protein synthesis) that would be predicted for the lower proliferative rate induced by PKCα overexpression in 11α and MDA-MB-231 cells (35). Furthermore, the lower oxidizing activity observed with the menadione/menadiol couple is in agreement with a study by others that employed menadione as a mediator in the potentiometric measurement of mammalian cultured cells that had been stimulated with growth factors (and thereby produced activation of PKC) (24). In that study, the authors cited the possibility that the PKC activation by these growth factors may activate signaling pathways that either inhibit oxidation of menadiol, or enhance the reduction of menadione.

4.3.3 Topographic Imaging of Cells with Hydrophilic Mediators

SECM current vs. distance (I_T - d) curves obtained with a tip approaching a mammalian cell in the presence of different hydrophilic redox mediators exhibited pure negative feedback (Fig. 4.13). When mediator species are not soluble in lipid phase and cannot permeate the membrane, no mediator regeneration by the cell is possible because the lipid bilayer is too thick for efficient electron tunneling (22,23,46). When the tip was scanned horizontally in a plane parallel to the bottom of a Petri dish, the tip current above the cell was significantly lower than that above the plastic surface (Fig. 4.14A). The cell surface thus impeded diffusion of the mediator to the tip (Fig. 4.4A). Similar experiments were performed with various hydrophilic mediators (e.g., ferrocene carboxylate, $Ru(NH_3)_6^{3/2+}$, $Fe(CN)_6^{3/4-}$,

and $Ru(CN)_6^{3/4-}$). Despite very different standard potentials of those redox couples, pure negative feedback was always observed, and no unmediated CT across the cell membrane could be detected.

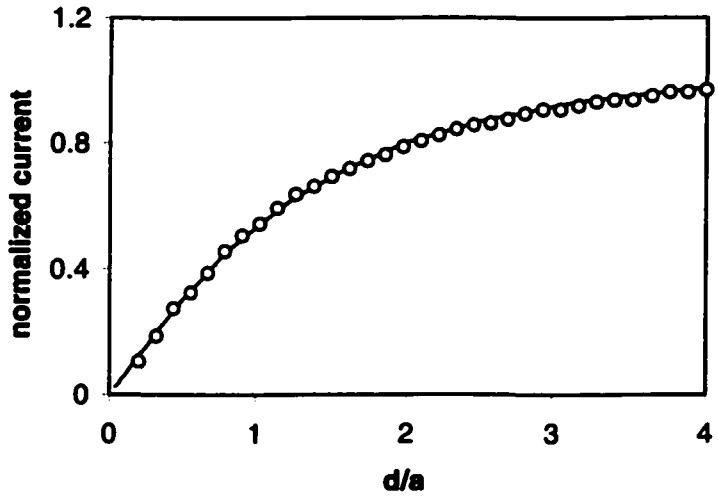

Fig. 4.13. A 5-μm-radius platinum tip approaches a MCF-10A cell. The solid line is the theoretical curve for an insulating substrate. Phosphate buffer contained 40 μM $Na_4Fe(CN)_6$. The tip potential was 0.3 V vs. Ag/AgCl. Similar curves were obtained with other hydrophilic mediators such as ferrocene carboxylate, $Ru(NH_3)_6^{3/2+}$, and $Ru(CN)_6^{3/4-}$.

A typical gray-scale image of a MCF-10A breast cell (Fig. 4.15A) contains only topographic information. In agreement with a one-dimensional scan in Fig. 4.14A, it shows a nucleus near the center of the cell surrounded by a much thinner cytoplasm. The MCF-10A cells are not motile. They spread over the surface and their shape appears irregular.

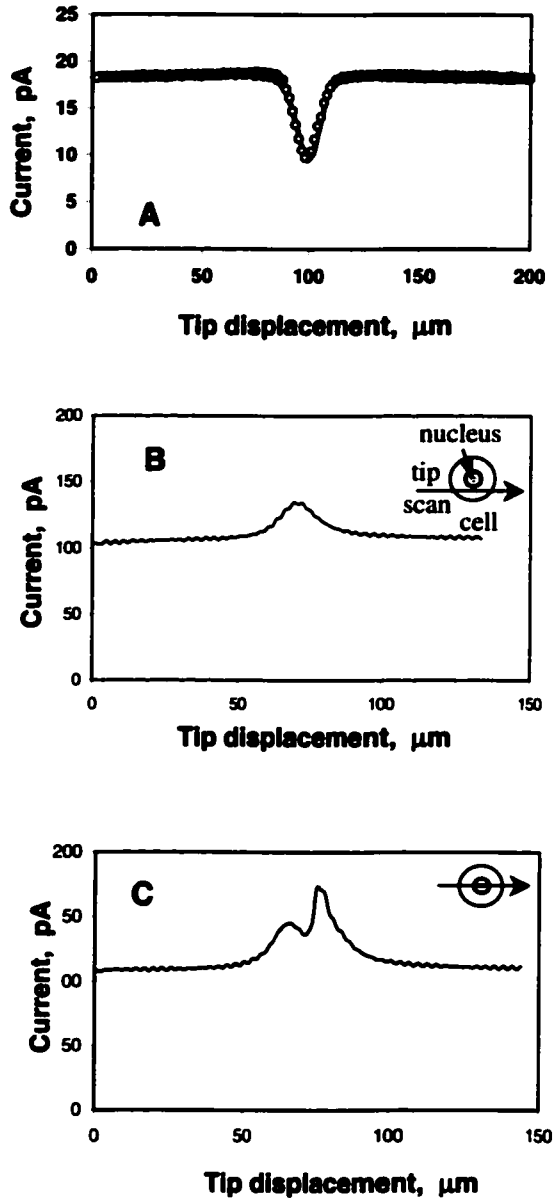

Fig. 4.14. Current vs. tip position dependencies for a 11-μm (A) and 7-μm (B, C) carbon tip scanned laterally over a MCF-10A cell in phosphate buffer solution containing 30 μM FcCOONa (A) and 40 μM 1,2-naphthoquinone (B, C). The scan rate was 20 μm/s. The tip potential was 0.35 V (A) and -0.36 V (B, C) vs. Ag/AgCl reference. The inserts in B and C show schematically the trajectory of the tip scan line relative to the cell nucleus. The solid line and symbols in (A) are obtained by scanning the probe in the forward and reverse directions above the same cell.

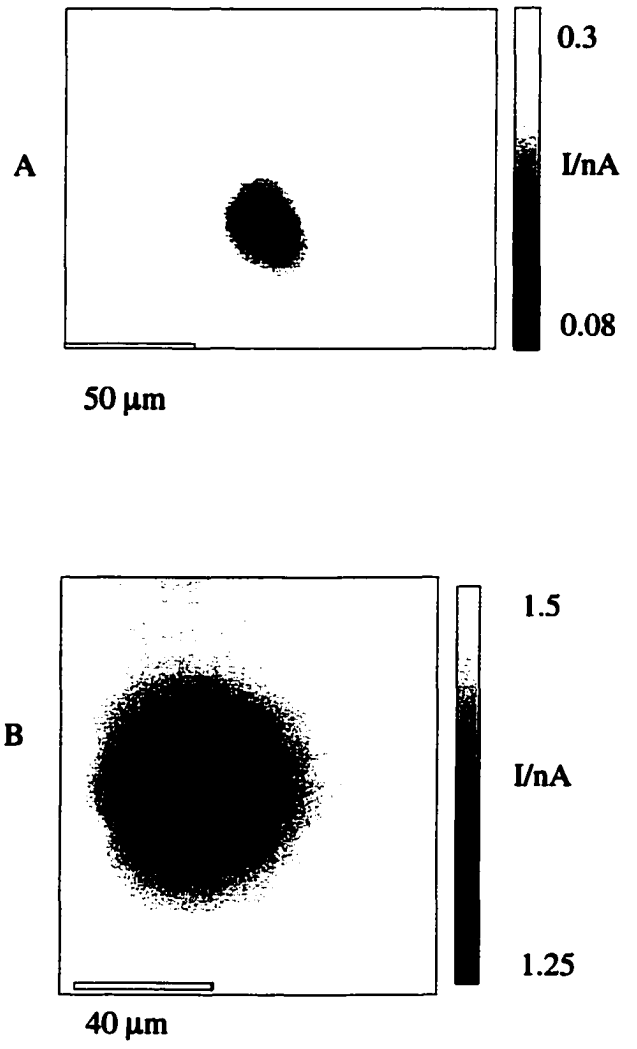

Fig. 4.15 Normal human breast (A) and metastatic (B) cells imaged by the SECM in solutions containing hydrophilic redox mediators [1 mM $Na_4Ru(CN)_6$ (A) and 1 mM $Ru(NH)_6Cl_3$ (B)]. The tip was an 5.5-μm-radius carbon (A) and a 12.5-μm-radius Pt UME (B). The tip potential was 0.84 V (A) and -0.3 V (B). The scan rate was 10 μm/s.

A topographic image of a metastatic (MDA-MB-231) cell (Fig. 4.15B) can be compared to the image in Fig. 4.15A. Unlike MCF-10A breast cells, the MDA-MB-231 cells are highly motile. They are less strongly attached to the plastic surface and appear to be essentially hemispherical. The cell diameter is about 50 μm, i.e., close to a typical cell size observed by optical microscopy. This is not surprising since (unlike generation/collection mode) feedback mode images are not distorted by diffusion broadening (37).

4.3.4 Mapping Redox Activity in the Cell

Unlike hydrophilic redox couples, with a lipid-soluble mediator (e.g., menadione or 1,2-naphthoquinone), the i_T increased when the tip was scanned horizontally above the cell (Figure 4.14B). As discussed previously, the increase in the i_T above the cell shown in Figure 4.14B can be attributed to intracellular oxidation of the reduced mediator species (menadiol) generated by the tip reaction. The tip current variations in this case represent the distribution of redox reactivity over the cell surface. An interesting feature in Fig. 4.14C is the presence of two closely spaced current maxima corresponding to the same immobilized cell. Such dual peaks are observed when the tip is scanned over the center of the cell rather than over its periphery (compare inserts in Figs. 4.14C and B). Apparently, the mediator regeneration rate is higher at the periphery of the cell than around its center. This deduction is confirmed by the gray-scale image of two aggregated MCF-10A cells in Figure 4.16A obtained using 40 μM 1,2-naphthoquinone mediator. The bright halo over the cell cytoplasm signifies the region of high redox activity, while dark, redox inactive area in the center of the cell is a nucleus that is apparently impenetrable to the mediator species. Figure 4.16B is the image of MDA-MB-231cells obtained with the same hydrophobic mediator. Compared with Figure 4.16B, the spatial resolution of Figure 4.16A is significantly higher because of a smaller tip size (1-μm-radius).

A large number of different redox couples are active within the cell, each of which may reside in different subcellular compartments (17). Although the images in Figure 4.16 show a fairly uniform distribution of redox reaction rate in the cytoplasm, one may wonder whether the redox process can be

confined to smaller organelles, e.g., mitochondria (24). Such a localization of redox activity would result in the appearance of small bright spots on SECM images corresponding to high local rate of mediator regeneration. Such micrometer-sized spots can be seen in Fig. 4.17. So far, the observation of locally increased redox activity has not been reproducible. Small bright spots apparent in Fig. 4.17 are present in some images, but cannot be seen in the others (compare Figs. 4.16A and 4.17). Although the origins of this irreproducibility have yet to be understood, such factors as the time interval since the cells have been removed from the incubator and the completeness of oxygen removal may be important.

The choice of a specific redox mediator allows one to image different chemical processes occurring in the cell. An interesting example is an image of a MCF-10A cell obtained with oxygen used as a redox mediator (Figure 4.18). The tip process in this case was

$$O_2 + 4H^+ + 4e^- = 2H_2O \qquad \text{(at the Pt tip)} \qquad (1)$$

Although the regeneration of molecular oxygen by the cell is highly improbable, the i_T above the cell is significantly higher than the tip current above the plastic surface (Fig. 4.18). The mechanism of the mediator regeneration in this case is most likely to be oxygen diffusion from the cell (Fig. 4.4B). The tip current enhancement near the cell surface is observed because of the high solubility of molecular oxygen in lipids (46). The high concentration of oxygen in the membrane provides an efficient pathway for its transport to the tip electrode and increases the effective mass transfer rate.

One should notice the differences between the data in Figure 4.18 and the images of oxygen fluxes at living cells by the SECM (14,15). In previous studies (14,15), the cells produced (or consumed) O_2, and the local changes in its concentration were monitored by the UME tip (substrate generation/tip collection mode of the SECM operation (37)). The magnitude of O_2 flux at the cell surface was determined by the rate of metabolism, solution composition, etc. The tip was only used as a "passive"

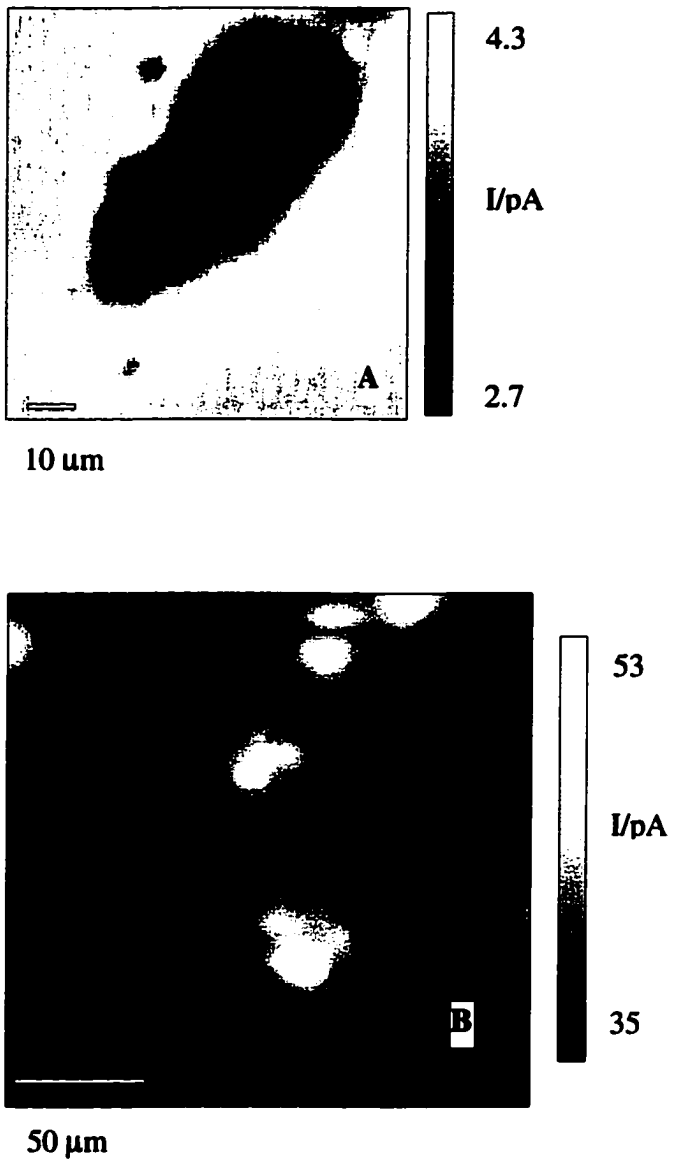

Fig. 4.16. Maps of redox activity in MCF-10A (A) and MDA-MB-231 (B) cells obtained with a hydrophobic redox mediator. The concentration of 1,2-naphthoquinone in solution was (A) 40 and (B) 30 µM. A 1-µm-radius Pt (A) or 5.5-µm C (B) tip was biased at -0.36 V vs. Ag/AgCl and scanned at 10 µm/s.

Fig. 4.17. Locally increased redox activity in a MCF-10A cell.

For parameters see Fig. 4.16A.

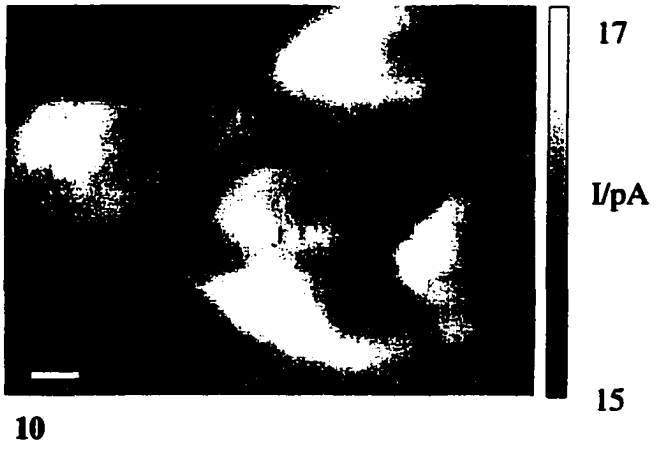

Fig. 4.18. Diffusion of oxygen mapped in several MCF-10A cells. No redox mediator was added to solution, and O_2 was not removed. Tip potential was -0.48 V vs. Ag/AgCl. For other parameters see Fig. 4.16A.

probe. By contrast, in our experiments, the expulsion of oxygen from the cell was induced by the depletion of its concentration in the proximity of the cell by the tip reaction (Eq 1). (A conceptually similar approach has recently been employed to probe the transfer of oxygen across liquid/liquid and liquid/air interfaces (47)). Such feedback mode measurements provide higher spatial resolution and allow accurate determination of interfacial mass/charge transfer rates (48).

Although it is assumed that no physical contact between the probe and the cell occurs in SECM experiments, it is hard to completely exclude the possibility of the cell surface being touched by the scanning tip during the imaging. An important question is how such a contact affects the cell. In general, the reproducibility of current vs. tip position curves obtained during successive scans of the tip over the cell surface (or by scanning the probe in the forward and reverse directions, see Fig. 4.14A) indicates that no physical contact occurred between the tip and the specimen. Two examples of the tip/cell collisions are shown in Figure 4.19. In Fig. 4.19A, the tip either destroyed the cell or dislodged it and pushed out of the image limits. Hence, the sharp horizontal boundary separating the imaged half of the cell from the featureless portion of the picture was obtained after the collision. In Fig. 4.19B, the collision was softer, and the cell was not destroyed. Nevertheless, a bright large spot caused by sudden increase in the tip current appears in the image at the moment when the tip touches the cell. No such spot can be seen in Fig. 4.19A where a high concentration of a hydrophilic mediator was used for topographic imaging.

Shown in Figure 4.20 is the preliminary redox map that was obtained for a homogenous population of MCF-10A cells (Figure 4.20 A) and a mixed population of 70% MCF-10A cells and 30% MDA-MB-231 cells (Figure 4.20 B). In figure 4.20B, a pocket of MDA-MB-231 cells (located in the lower left-hand quadrant) can be distinguished by their shape from the tightly aggregated MCF-10A cells. This result suggested that SECM may be used to screen for aberrant responses (indicative of metastatic cells) in a large field of non-metastatic breast cells in culture and in tissues.

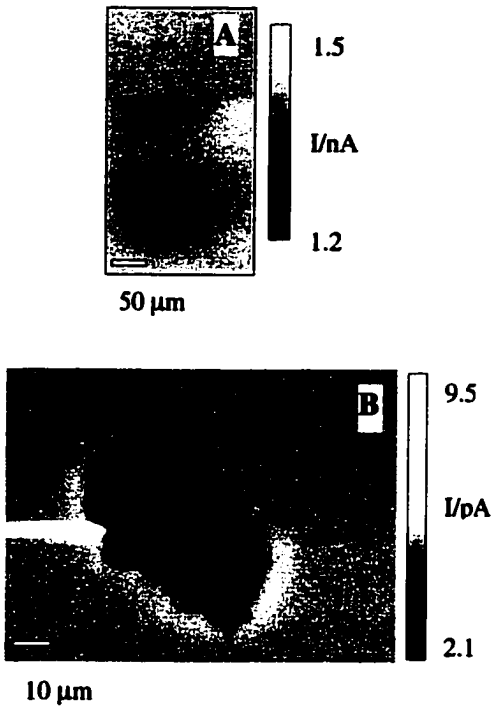

Fig. 4.19. Effect of the tip touching the cell surface on the SECM images. (A) A MDA-MB-231 cell is destroyed by the 25-μm Pt tip. The mediator was 1 mM $Ru(NH_3)_6Cl_3$. (B) The cell remains intact after a physical contact with a tip. A bright spot corresponds to the place of the tip/cell collision. For parameters see Fig. 4.16A.

4.3.5. Imaging pH profiles around living cells

Another application of the SECM explored in this research is the measurement of acid fluxes of acid produced by immobilized cells. Acid excretion is an important characteristic that is often used as a measure of metabolic rate (49). The differences in the capacity to excrete protons between normal and cancer cell (50) and specifically MDA-MB-231 metastatic breast cells (51) have been investigated previously. The methodology for potentiometric SECM measurements has been previously developed and used to probe pH profiles around microscopic targets (33,52,53). In the present research, we employed micrometer-sized Sb electrodes to monitor the efflux of acid and image pH profiles around a single cell (Fig. 4.21). We reproducibly prepared 2- to 20-μm-diameter disk-shaped antimony tips with fast and stable pH responses. These electrodes can be operated in both amperometric and potentiometric modes (33). In amperometric regime, diffusion-controlled reduction of oxygen occurs at the Sb surface. This mode of SECM operation was used to find an immobilized cell on the plastic surface and to evaluate the distance between the Sb tip and the cell membrane. The use of oxygen as a mediator is especially advantageous for experiments with living cells because it allows one to avoid adding to the solution other redox species, which might influence the cell response. After using the amperometric function of the tip to find an immobilized cell, potentiometric pH measurements can be performed.

Two typical potential vs. pH calibration curves for a 3.5-μm-radius antimony electrode are shown in Figure 4.22. Curve 1 was obtained before the Sb probe was used for cell imaging. Curve 2 was obtained after the electrode was employed as an SECM tip and worked in both amperometric (i.e., finding the cell) and potentiometric (probing pH profiles) regimes for about two hours. Clearly, the two calibration curves are very similar, and the slope of 50 – 51 mV pH^{-1} unit is consistent with the previously reported values (33). Thus, the potentiometric response of a Sb tip did not change significantly during fairly long SECM experiments and was not greatly affected by switching between potentiometric and amperometric modes of operation. The response stability and a short response time (i.e., ≤ 5 s required for the potential to stabilize after the electrode is moved from one buffer solution to

the other) were crucial for mapping pH profiles generated by cell metabolism. A typical one-dimensional pH profile obtained by scanning the Sb tip over an 11 α cell (curve 1 in Fig. 4.23) shows a significant increase in $[H^+]$ above the cell surface in agreement with previous studies (49-51). Scanning the tip in the opposite direction above the same cell produces a similar profile (curve 2 in Fig. 4.23). Minor differences between the curves 1 and 2 represent non-steady-state effects produced by the moving tip, i.e., stirring the diffusion layer and screening the cell surface from solution.

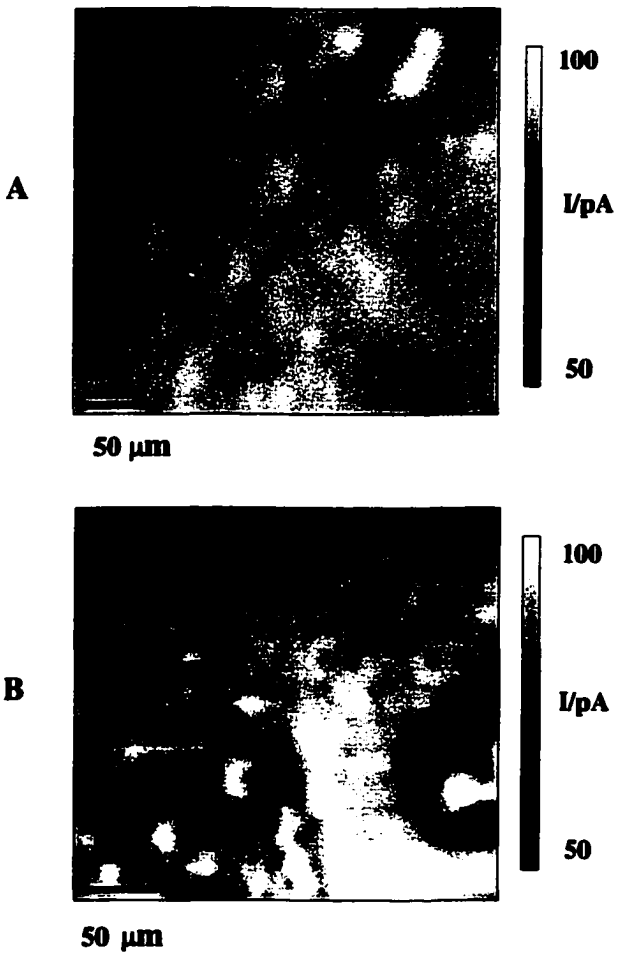

Fig. 4.20 The image of MCF-10A (A) and the mixture of MCF-10A and MDA-MB-231 cells (B). Tip: 5.5 μm-radius carbon. Mediator: 30 μM menadione. Scan rate: 10 μm/s.

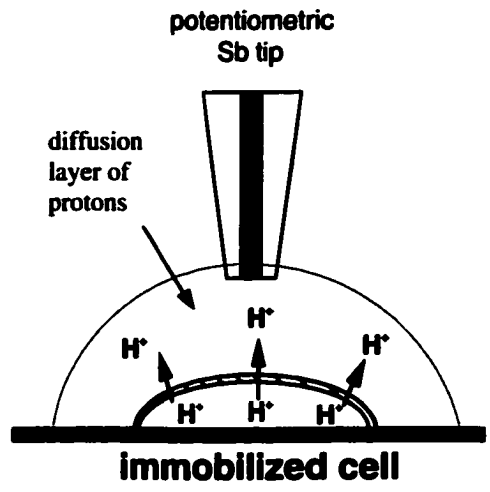

Fig. 4.21. Concentration profile of protons around an immobilized cell measured with a potentiometric Sb tip.

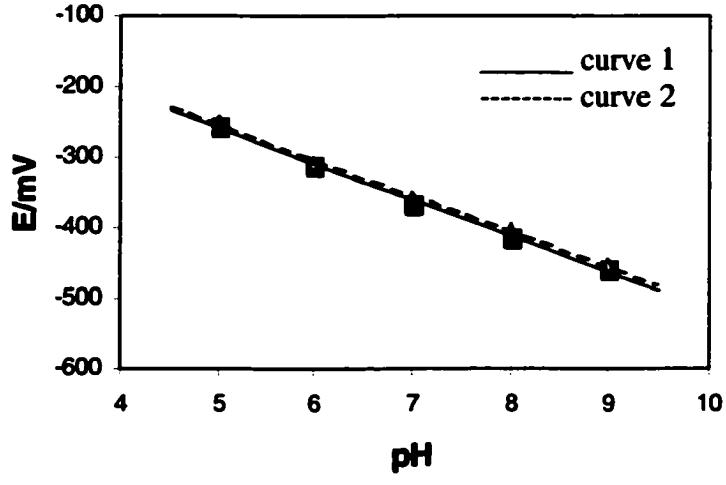

Fig. 4.22. Potential vs. pH calibration curves obtained for a 7-μm Sb potentiometric tip before (squares, curve 1) and after (triangles, curve 2) SECM measurements. The solid line (51 mV/pH unit slope) and the dashed (50 mV/pH unit slope) lines represent the best linear fit.

Unlike feedback mode maps of redox reactivity (Fig. 4.16), gray scale images of the pH profiles (Fig. 4.24) are obtained using generation/collection mode of the SECM operation (37). The flux of protons ejected from the cell produces a concentration profile around it, which can be probed by a potentiometric Sb tip. The cells in Fig. 4.24 are somewhat enlarged by diffusion broadening effect. The resolution could be slightly improved by increasing the buffer concentration to reduce the thickness of the diffusion layer of protons. However, it is very difficult to avoid crushing a potentiometric tip into a cell when it is moved within a thin diffusion layer. The comparison of pH profiles measured for different cells showed that the pH near the

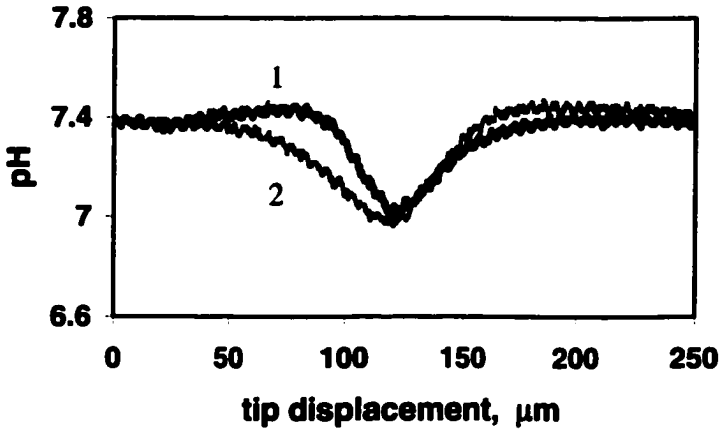

Fig. 4.23. One-dimensional pH profile obtained by scanning a 7-μm Sb tip over an 11α cell. Curves 1 and 2 represent the successive forward and reverse scans of the tip over the cell surface. Solution was a 2 mM pH 7.4 phosphate buffer. The scan rate was 10 μm/s.

surface of a MCF-10A cell is lower than that for an 11α cell and significantly lower than the pH in a close proximity of an MDA-MB-231 cell. Further research work need to be carried out to correlate the level of acid release with metastasis. Besides diagnostic possibilities (51), this approach may allow one to evaluate the anti-metastatic activity of prospective pharmacological agents (54).

Fig. 4.24. pH profile around a group of MCF-10A cells obtained with a 7-μm potentiometric Sb probe. The scan rate was 10 μm/s. Solution was a 2 mM pH 7.4 phosphate buffer.

4.4 Conclusions

This study has shown that the SECM is a suitable tool for probing ET reactions in single biological cells. Effective rate constants have been measured for bimolecular reactions between hydrophobic redox mediators and intracellular redox moieties. The difference in redox activities between the normal

and cancer cells has been correlated with the expression level and the catalytic activity of PKCα enzyme in the cells.

The intracellular concentration of the redox agents that can oxidize menadiol is larger in a MCF-10A cell than in an MDA-MB-231 cell. Depending on the mediator concentration, the overall charge transfer rate may be limited by the mediator transport across the membrane or by the availability of intracellular redox agents.

Topography and redox reactivity of human breast cells have been imaged by the scanning electrochemical microscope. Various chemical processes occurring in living cells (e.g., electron transfer reactions, molecular diffusion of oxygen, proton pumping across the membrane) can be imaged with a submicrometer spatial resolution. Mapping intracellular redox activity combined with potentiometric measurements employing scanning pH microprobe can provide valuable information about cell metabolism, respiration, photosynthesis and other important biochemical processes.

SECM imaging of biological cells is challenging because they are soft, not flat and can be easily damaged by the tip. This is especially true for potentiometric imaging and for feedback mode experiments, in which the feedback from the cell is neither purely positive nor purely negative. Nevertheless, a conventional, constant height imaging is feasible and can provide useful information on both topography and reactivity. Because the scanning ultramicroelectrode probe allows one to map transmembrane CT rates with high spatial resolution, a potential application of SECM is to detect aberrant responses in large fields of cells and tumor specimens.

Bibliography

Chapter I

1. Girault, H. H. in *Modern Aspects of Electrochemistry*; Bockris, J. O. M.; Conway, B. E. and White R. E., Eds., Plenum Press, New York, 1993, Vol. 25, p. 1.
2. Volkov, A.G., Ed., *Liquid Interface in Chemical, Biological, and Pharmaceutical Applications*, Marcel Dekker, New York, 2001.
3. Arai, K.; Ohasawa, M.; Kusu, F.; Takamura, K. *Bioelectrochem. Bioenerg.* 1993, 31, 65.
4. Sun, K.; Mauzerall, D. J. *J. Phys. Chem.* B. 1998, *102*, 6440.
5. Samec, Z.; Kakiuchi, T. in *Advances in Electrochemical Science and Electrochemical Engineering*, Vol. 4, Gerischer, H. and Tobias, C. W., Eds., VCH, NY 1995, p. 297
6. Ohkouchi, T.; Kakutani, T.; Senda, M. *Bioelectrochem. Bioenerg.* 1991, 25,81.
7. Girault, H. H.; Schiffrin, D. J. In *Charge and Field Effects in Biosystems;* Allen, M.J., Usherwood, P. N. R., Eds.; Abacus Press: Turnbridge Wells, England, 1984, p. 171.
8. Gennis, R. B. *Biomembranes*, Springer: New York, 1995.
9. Nernst, W.; Riesenfield, E.H. *Ann. Phys.* 1902, 8, 600.
10. Cremer, M. *Z. Biol.* 1906, 47, 562.
11. Gavach, C.; Mlodnicka, T.; Gustalla, J. *C. R. Acad. Sci.* 1968, C266, 1196.
12. Samec, Z.; Marecek, V.; Weber, J. *J. Electroanal. Chem.* 1979, 103, 11.
13. Samec, Z.; Marecek, V.; Weber, J. *J. Electroanal. Chem.* 1978, 96, 245.
14. Samec, Z.; Marecek, V.; Koryta, J.; Khalil, M. W. *J. Electroanal. Chem.* 1977, 83, 393.
15. Taylor, G.; Girault, H.H. *J Electroanal Chem* 1986, 208, 179.
16. Campbell, J.A.; Girault, H.H. *J Electroanal Chem* 1989, 266, 465.
17. Shao, Y.; Girault, H.H. *J Electroanal Chem* 1992, 334, 203.
18. Liu, B.; Mirkin, M. V. in *Liquid Interface in Chemical, Biological, and Pharmaceutical Applications*, Volkov, A.G., Ed., Marcel Dekker, New York, 2001, pp. 373-397.
19. Liu, B.; Mirkin, M. V. *Anal. Chem.* 2001, 73, 670A.

20. Marcus, R. A. *J. Phys. Chem.* 1990, *94*, 1050.

21. Marcus, R. A. *J. Phys. Chem.* 1990, *94*, 4152; addendum, *J. Phys. Chem.* 1990, *94*, 7742.

22. Marcus, R. A. *J. Phys. Chem.* 1991, *95*, 2010.

23. Benjamin, I. *Chem. Rev.* 1996, *96*, 1449.

24. Benjamin, I. *Acc. Chem. Res.* 1995, *28*, 233.

25. Benjamin, I. *Science* 1993, *261*, 1559.

26. Schweighofer, K. J. Benjamin, I. *J. Electroanal. Chem.* 1995, *391*, 1.

27. Benjamin, I. *Ann. Rev. Phys. Chem.* 1997, 48, 407.

28. Schmickler, W. *J. Electroanal. Chem.* 1997, *428*, 123.

29. S Frank, W. Schmickler, *J. Electroanal. Chem.* 2000, 483, 18.

30. S Frank, W. Schmickler, *J. Electroanal. Chem.* 2001, 500, 491.

31. Kakiuchi, T.; Takasu, Y. *J. Phys. Chem. B* 1997, *101*, 5963.

32. Ding, Z.; Fermin, D. J.; Brevet, P.-F.; Girault, H. H. *J. Electroanal. Chem.*, 1998, 458, 139.

33. Dryfe, R. A. W.; Ding, Z. F.; Wellington, R. G.; Brevet, P.-F.; Kuznetzov, A. M.; Girault, H. H. *J. Phys. Chem.* A, 1997, 101, 2519.

34. Conboy, C.; Richmond, G. L. *J. Phys. Chem.* B, 1997, 101, 983.

35. Naujok, R. R.; Paul, H. J.; Corn, R. M. *J. Phys. Chem*, 1996, 100, 10497.

36. Luca, A. A. T.; Hebert, P.; Brevet, P.-F.; Girault, H. H. *J. Chem. Soc., Faraday Trans.*, 1995, 91,1763.

37. Mirkin, M.V. *Anal. Chem.* 1996, 68, 177A.

38. Mirkin, M.V. *Microchim. Aata* 1999, 130, 127.

39. Amemiya, S.; Ding, Z.; Zhou, J.; Bard, A.J. *J. Electroanal. Chem.* 2000, 483, 7.

40. Girault, H. H.; Schiffrin, D. J. *in Electrochemistry of Liquid/Liquid Interfaces*, Marcel Dekker, Bard, A.J. Ed., New York and Basel, 1989; Vol. 15, pp 1.

41. Senda, M.; Kakiuchi, T.; Osakai, T. *Electrochim. Acta* 1991, *36*, 253.

42. Koryta, J. *Electrochim. Acta* 1979, *24*, 293.

43. Koryta, J. *Electrochim. Acta* 1984, *29*, 445.

44. Koryta, J. *Electrochim. Acta* 1988, *33*, 189.

45. Samec, Z. *Chem. Rev.* 1988, *88*, 617.

46. Reymond, F.; Fermin, D.; Lee, H.J.; Girault, H. H. *Electrochimica Acta* 2000, *45*, 2647.

47. Volkov, A.G.; Deamer, D.W., Eds., *Liquid-Liquid Interfaces Theory and Methods*; CRC Press, 1996.

48. Verwey, E.J.W.; Niessen, K.F. *Phylos. Mag.* 1939, 28, 435.

49. Bard, A.J.; Faulkner, L.R. Eds., *electrochemical Methods, Fundamental and Applications*, 2nd Edition, John Wiley, New York, 2001.

50. Gavach C.; Seta, P.; D'Epenoux, B. *J. Electroanal. Chem.* 1977, *83*, 225.

51. Gros, M.; Gromb, S.; Gavach, C. *J. Electroanal. Chem.* 1978, 89, 29.

52. Reid, J. D.; Melroy, O. R.; Buck, R. P. *J. Electroanal. Chem.* 1983, 147, 71.

53. Kakiuchi, T.; Senda, M. *Bull. Chem. Soc. Jpn.* 1983, 56, 1322.

54. Kakiuchi, T.; Senda, M. *Bull. Chem. Soc. Jpn.* 1983, 56, 1753.

55. Kakiuchi, T.; Senda, M. *Bull. Chem. Soc. Jpn.* 1983, 56, 2912.

56. Samec, Z.; Marecek, V.; Homolka, D. *Faraday Discuss. Chem. Soc.* 1984, 77, 277.

57. Samec, Z.; Marecek, V.; Homolka, D. *J. Electroanal. Chem.* 1981, 126, 121.

58. Samec, Z.; Marecek, V.; Holub, K.; Racinsky, S.; Hajkova, P. *J. Electroanal. Chem.* 1983, 151, 277.

59. Samec, Z.; Marecek, V.; Holub, K.; Racinsky, S.; Hajkova, P. *J. Electroanal. Chem.* 1987, 255, 65.

60. Samec, Z.; Marecek, V.; Homolka, D. *J. Electroanal. Chem.* 1985, 187, 31.

61. Girault, H. H.; Schiffrin, D. J.; Smith, B. D. V. *J. Colloid Interface Sci.* 1984, 101, 257.

62. Girault, H. H.; Schiffrin, D. J. *J. Electroanal. Chem.* 1983, 150, 43.

63. Girault, H. H.; *Electrochim. Acta* 1987, 32, 383.

64. Cheng, Y.; Cunnane, V.J.; Schiffrin, D.J.; Murtomäki, L.; Kontturi, K. *J. Chem. Soc. Faraday Trans.* 1991, 87, 107.

65. Fernandes, P.A.; cordeiro, M.N.D.S Gomes,.; J.A.N.F. *J. Phys. Chem. B* 1999, 103, 6290.

66. Kakiuchi, T.; Kobayash, M.; Senda, M. *Bull. Chem. Soc. Jpn.* 1987, 60, 3109.

67. Wiles, M. C.; VanderNoot, T.; Schiffrin, D. J. *J. Electroanal. Chem.* 1990, 281, 231.

68. Higgins, D. A.; Corn, R. M.; *J. Phys. Chem.* 1993, 97, 489.

69. Samec, Z. *J. Electroanal. Chem.* 1997, 426, 31.

70. Pereira, C.M.; Schmickler, W.; Silva, F.; Sousa, M. J. *J. Electroanal. Chem.* 1997, 436, 9.

71. Frank, S.; Schmickler, W. *J. Electroanal. Chem.* 2001,500, 491.

72. Girault, H. H.; Schiffrin, D. J. *J. Electroanal. Chem.*, 1984, 179, 277.

73. Kakiuchi, T.; Yamane, M.; Osakai, T.; Senda, M. *Bull. Chem. Soc. Jpn.*, 1987, 60, 4223.

74. Kakiuchi, T.; Nakanishi, M.; Senda, M. *Bull. Chem. Soc. Jpn.*, 1988, 61, 1845.

75. Wandlowski, T.; Marecek, V.; Samec, Z. *J. Electroanal. Chem.*, 1988, 242, 277.

76. Kakiuchi, T.; Kondo, T.; Kotani, M.; Senda, M. *Langnmuir* 1992, 8,169.

77. Kakiuchi, T.; Kondo, T.; Senda, M. *Bull. Chem. Soc. Jpn.*1990, 63, 3270.

78. Samec, Z.; MareČek, V.; Homolka, D. *J. Electroanal. Chem.* 1981, 126, 105.

79. Samec, Z. *J. Electroanal. Chem.* 1980, 111, 211.

80. Girault, H. H.; Schiffrin, D. J. *J. Electroanal. Chem.* 1988,244,15.

81. Tsionsky, M.; Bard, A. J.; Mirkin, M. V. *J. Phys. Chem.* 1996, *100*, 17881.

82. Tsionsky, M.; Bard, A. J.; Mirkin, M. V. *J. Am. Chem. Soc.* 1997, *119*, 10785

83. Samec, Z. *J. Electroanal. Chem.* 1979, 99,197.

84. Kharkats, Yu. I.; Volkov, A.G. *J. Electroanal. Chem.* 1985, 184, 435.

85. Geblewicz, G.; Schiffrin, D. J. *J. Electroanal. Chem.* 1988, 244,27.

86. Cheng, Y.; Schiffrin, D. J. *J. Electroanal. Chem.* 1991, 314, 153.

87. Cunnane, V.J.; Schiffrin, D. J.; Beltran, C.; Geblewicz, G.; Solomon, T. *J. Electroanal. Chem.* 1988, 247, 203.

88. Nicholson, R.S. *Anal. Chem.* 1965, 37, 1351.

89. Chen, Q.Z.; wamoto, K.I.; Seno, M. *Electrochim. Acta* 1991, 36,291.

90. Cheng, Y.; Schiffrin, D.J. *J.Chem. Soc. Faraday Trans.* 1993, 89, 199.

91. Bard, A.J.; Fan, F-R.; Mirkin, M.V. in: Electrochemistry, vol. 18, Bard, A.J. Ed., Marcel Dekker, New York, 1993, p. 243.

92. Bard, A.J.; Mirkin, M.V. Eds., Scanning Electrochemical Microscopy, Marcel Dekker, New York, 2001, p. 299.

93. Wei, C.; Bard, A.J.; Mirkin, M.V. *J. Phys. Chem.* 1995, 99, 16033.

94. Delville, M-H.; Tsionsky, M.; Bard, A. J. *Langmuir* 1998, 14, 2774.

95. Liu, B.; Mirkin, M.V. *J.Am. Chem. Soc.* 1999, 121, 8352.

96. Barker, A.L.; Unwin, P.R.; Amemiya, S.; Zhou, J.F.; Bard, A.J. *J. Phys. Chem.* B 1999, 103, 7260.

97. Solomon, T.; Bard, A.J. *Anal Chem* 1995, 67, 2787.

98. Quinn, B.; Lahtinen, R.; Murtomäki, L.; Kontturi, K. *Electrochim Acta* 1998, 44, 47.

99. Oldham, K. B.; Myland, J.C.; Zoski, C.G.; Bond, A.M. *J Electroanal Chem* 1989, 270, 79.

100. Mirkin, M.V.; Bard, A.J. *Anal Chem* 1992, 64, 2293.

101. Samec, Z.; Marecek, V. *J Electroanal Chem* 1986, 200, 17.

102. Gavach, C.; Epenoux, B.d'; Henry, F. *J Electroanal Chem* 1975, 64, 107.

103. Shao, Y.; Girault, H.H. *J Electroanal Chem* 1990, 282,59.

104. Samec, Z.; Marecek, V.; Weber, J. *J Electroanal Chem* 1979, 100, 841.

105. Gavach, C.; Henry, F. *J Electroanal Chem* 1974, 54, 361.

106. Buck, R.P.; Bronner, W.E. *J Electroanal Chem* 1986, 197, 179.

107. Bronner, W.E.; Meleroy, O.R.; Buck, R.P. *J Electroanal Chem* 1984, 162, 263.

108. Osakai, T.; Kakutani, T.; Senda, M. *Bull. Chem. Soc. Jpn.* 1985, 58, 2826.

109. Kakiuchi, T.; Noguchi, J.; Kotani, M.; Senda, M. *J Electroanal Chem* 1990, 296, 517.

110. Kakiuchi, T.; Noguchi, J.; Senda, M. *J Electroanal Chem* 1992, 336, 137.

111. Wandlowski, T.; Marecek, V.; Samec, Z. *J Electroanal Chem* 1988, 242, 291.

112. Wandlowski, T.; Marecek, V.; Holub, K.; Samec, Z. J. Phys. Chem. 1989, 93, 8204.

113. Wandlowski, T.; Marecek, V.; Samec, Z.; Fuoco, R. *J Electroanal Chem* 1992, 331, 765.

114. Shao, Y.; Mirkin, M.V. *J Am Chem Soc* 1997, 119, 8103.

115. Beattie, P.D.; Delay, A.; Girault, H.H. *Electrochim Acta* 1995, 40, 2961.

116. Tokuda, K.; Kitamura, F.; Liao, Y.; Okuwaki, M.; Ohsaka, T. in *Charge Transfer at Liquid/Liquid and Liquid/Membrane Interface.* Kyoto, 1996, pp.7-8.

117. Liao, Y.; Okuwaki, M.; Kitamura, F.; Ohsaka, T.; Tokuda, K. *Electrochim Acta* 1998, 44, 117.

118. Shao, Y.; Mirkin, M.V. *J Electroanal Chem* 1997, 439, 137.

119. Shao, Y.; Mirkin, M.V. *J Phys Chem* B 1998, 102, 9915.

120. Koryta, J.; Hung , L. Q.; Hofmanova, A. *Studia Biophys.*, 1982, 90, 25.

121. Cunnane, V. J.; Schiffrin, D. J.; Fleishmann, M.; Geblewicz, G.; Williams, D. *J. Electroanal. Chem.*, 1988, 243, 455.

122. Kakiuchi, T.; Kotani, M.; Noguchi, J.; Nakanishi, M.; Senda, M. *J. Colloid Interface Sci.* 1992, 149, 279.

123. Kakiuchi, T. In *Liquid-Liquid Interfaces. Theory and Methods*; Volkov, A. G.; Deamer, D. W., Eds; CRC Press: Boca Raton, 1996. p 317.

124. Murtomaki, L.; Manzanares, J.A.; Mafe, S.; Kontturi, K. in *Liquid Interface in Chemical, Biological, and Pharmaceutical Applications,* Volkov, A.G., Ed., Marcel Dekker, New York, 2001, pp. 533-552.

125. Shao, Y.; Campbell, J.A.; Girault, H.H. *J. Electroanal. Chem.* 1991, 300, 415.

126. Girault, H.H.; Schiffrin, D. J. *J Electroanal Chem* 1985, 195, 213.

127. Vandernoot, T.J.; Schiffrin, D. J. *J Electroanal Chem* 1990, 35, 1359.

128. Samec, Z.; Kakiuchi, T.; Senda, M. *Electrochim. Acta,* 1995, 40, 2971.

129. Senda, M. *Anal. Sci.* 1991, 7, 585.

130. Kakiuchi, T. *J Electroanal Chem* 1992, 322.55.

131. Kontturi, K.; Manzanares, J.A.; Murtomaki, L. *Electrochim Acta* 1995, 40, 2979.

132. Senda, M. *Electrochim Acta* 1995, 40, 2993.

133. Kontturi, K.; Manzanares, J.A.; Murtomaki, L.; Schiffrin, D. J. *J. Phys. Chem. B*, 1997, 101, 10801.

134. Bard, A.J.; Mirkin, M.V. Eds., *Scanning Electrochemical Microscopy*, Marcel Dekker, New York, 2001, p. 397

Chapter II

1. Sun, K.; Mauzerall, D. J. *J. Phys. Chem.* B. 1998, *102*, 6440.

2. Clark, J. F.; Clark, D. L.; Strauss, S. H. *EnViron. Sci. Technol.* 1996, *30*, 3124.

3. Tsionsky, M.; Bard, A. J.; Mirkin, M. V. *J. Phys. Chem.* 1996, *100*, 17881.

4. Tsionsky, M.; Bard, A. J.; Mirkin, M. V. *J. Am. Chem. Soc.* 1997, *119*, 10785.

5. Wei, C.; Bard, A.J.; Mirkin, M.V. *J. Phys. Chem.* 1995, 99, 16033.

6. Ding, Z.; Fermin, D. J.; Brevet, P.-F.; Girault, H. H. *J. Electroanal. Chem.*, 458 (1998) 139.

7. Fermin, D. J.; Ding, Z.; Duong, H. D.; Brevet, P.-F.; Girault, H. H. *J. Phys. Chem.* B 1998, *102*, 10334.

8. Girault, H. H. in *Modern Aspects of Electrochemistry*; Bockris, J. O. M.; Conway, B. E. and White R. E., Ed.; Plenum Press, New York, 1993, Vol. 25, p. 1.

9. Marcus, R. A. *J. Phys. Chem.* 1990, *94*, 1050.

10. Marcus, R. A. *J. Phys. Chem.* 1990, *94*, 4152; addendum, *J. Phys. Chem.* 1990, *94*, 7742.

11. Marcus, R. A. *J. Phys. Chem.* 1991, *95*, 2010.

12. Geblewicz, G.; Schiffrin, D. J. *J. Electroanal. Chem.* 1988, 244,27.

13. Cheng, Y.; Schiffrin, D.J. *J.Chem. Soc. Faraday Trans.* 1993, 89, 199.

14. Girault, H. H.; Schiffrin, D. J. *J. Electroanal. Chem.* 1988,244,15.

15. Samec, Z.; Marecek, Homolka, V.; D. *J Electroanal Chem* 1983, 156, 25.

16. Katano, H.; Maeda, K.; Senda,. M. *J. Electroanal. Chem.* 1995, *396*, 391.

17. Schmickler, W. *J. Electroanal. Chem.* 1997, *428*, 123.

18. A.J. Bard and L.R. Faulkner, Eds., *electrochemical Methods, Fundamental and Applications,* 2nd Edition, John Wiley, New York, 2001. pp. 534-579.

19. Hanzlik, J.; Hovorka, J.; Samec, Z.; Toma, S. *Collect. Czech. Chem.Commun.* 1988, *53*, 903.

20. Amemiya, S.; Ding, Z.; Zhou, J.; Bard, A.J. *J. Electroanal. Chem.* 2000, 483, 7.

21. Bard, A.J.; Mirkin, M.V. Ed. Scanning Electrochemical Microscopy, Marcel Dekker, New York, 2001. p. 299.

22. Liu, B.; Mirkin, M.V. *J.Am. Chem. Soc.* 1999, 121, 8352.

23. Barker, A. L.; Gonsalves, M.; Unwin, P. R. *Anal. Chim. Acta* 1999, *385*, 223.

24. Zhang, Z.; Yuan, Y.; Sun, P.; Su, B.; Guo, J.; Shao, Y.; Girault, H. H. *J. Am. Chem. Soc., submitted.*

25. Palmer, G. A., Ed, *Long-Range Electron-Transfer in Biology;* Structure and Bonding 75; Springer-Verlag: Berlin; 1991.

26. Lahiri, J.; Fate, G. D.; Ungashe, S. B.; Groves, J. T. *J. Am. Chem. Soc.* 1996, *118*, 2347.

27. Chidsey, C. E. D. *Science* 1991, *251*, 919.

28. Finklea, H. O. In *Electroanalytical Chemistry* ; Bard, A. J., Ed.; Marcel Dekker: New York, 1996; Vol. 19, p. 109.

29. Sachs, S. B.; Dudek, S. P.; Hsung, R. P.; Sita, L. R.; Smalley, J. F.; Newton, M. D.; Feldberg, S. W.; Chidsey, C. E. D. *J. Am. Chem. Soc.* 1997, *119*, 10563.

30. Kakiuchi, T. In *Liquid-Liquid Interfaces. Theory and Methods*; Volkov, A. G.; Deamer, D. W., Eds; CRC Press: Boca Raton, 1996. p. 317.

31. Kakiuchi, T.; Kondo, T.; Senda, M. *Bull. Chem. Soc. Jpn.* 1990, *63*, 3270.

32. Krause, R. A.; Violette, C. *Inorg. Chim. Acta* 1986, *113*, 161.

33. Bard, A.J.; Fan, F-R.; Mirkin, M.V. in: A.J. Bard (Ed.), Electrochemistry, vol. 18, Marcel Dekker, New York, 1993, p. 243.

34. Shao, Y.; Mirkin, M. V.; Rusling, J. F. *J. Phys. Chem. B* 1997, *101*, 3202.

35. Delville, M-H.; Tsionsky, M.; Bard, A. J. *Langmuir* 1998, 14, 2774.

36. Zhang, J.; Barker, A. L.; Unwin, P. R. *J. Electroanal. Chem.* 2000, 483, 95.

37. Shi, C.; Anson, F. C. *J. Phys. Chem.* 1998, *102*, 9850.

38. Wang, H.; Borguet, E.: Eisenthal, K. B. *J. Phys. Chem. B* 1998,*102*, 4927.

39. Weaver, M. J. *Chem. ReV.* 1992, *92*, 463.

40. Weaver, M. J. In *Electrified Interfaces in Physics, Chemistry and Biology*; Guidelli, R., Ed.;Kluwer Academic Publishers: Netherlands, 1992; p 427.

41. Fawcett, W.R. *Langmuir* 1989, 5, 661.

42. Girault, H.H. unpublished results.

43. Reid, J. D.; Melroy, O. R.; Buck, R. P. *J. Electroanal. Chem.* 1983, 147, 71.

44. Uchiyama, Y.; Kitamori, T.; Sawada, T. *Langmuir* 2000, *16*, 6597.

45. Girault, H. H. *Electrochim. Acta* 1987, 32, 383.

46. Barker, A.L.; Unwin, P.R.; Amemiya, S.; Zhou, J.F.; Bard, A.J. *J. Phys. Chem.* B 1999, 103, 7260.

47. Zhang, J.; Unwin, P. R.*J. Phys. Chem. B* 2000, *104*, 2341.

48. Ding, Z.; Quinn, B. M.; Bard, A. J. *J. Phys. Chem. B* 2001; *105*, 6367.

49. Kakiuchi, T. *J. Electroanal. Chem.* 2001, *496*, 137.

50. Quinn, B.; Kontturi, K. *J. Electroanal. Chem.* 2000, *483*, 124.

51. Pereira, C. M.; Silva, F.; Sousa, M. J.; Kontturi, K.; Murtomäki, L. *J. Electroanal. Chem.* 2001, *509*, 148.

52. Amatore, C.; Savéant, J. M.; Tessier, D. *J. Electroanal. Chem.* 1983, *147*, 39.

53. Forouzan, F.; Bard, A. J.; Mirkin, M. V. *Isr. J. Chem.* 1997, *37*, 155.

54. Kakiuchi, T. In *Liquid-Liquid Interfaces. Theory and Methods*; Volkov, A. G.; Deamer, D. W., Eds; CRC Press: Boca Raton, 1996. p. 317.

55. Seimiya, T.; Ohki, S. *Biochim. Biophys. Acta* 1973, *298*, 546.

56. Ohnishi, S.; Ito, T. *Biochemistry*, 1974, *13*, 881.

57. Miller, C. J. In *Physical Electrochemistry: Principles, Methods, and Applications;* Rubinstein, I., Ed.; Marcel Dekker: New York, 1995, p. 27.

Chapter III

1. Koryta, J. *Ions, electrodes and membranes*, 2nd ed.; Wiley & Sons: New York, 1992.

2. Inzelt, G. In *Electroanalytical Chemistry*; Bard, A. J., Ed.; Marcel Dekker: New York, 1994; Vol. 18, p 89.

3. Reymond, F.; Fermin, D.; Lee, H. J.; Girault, H. H. *Electrochimica Acta* 2000, 45, 2647.

4. Girault, H. H. In *Modern Aspects of Electrochemistry*; Bockris, J. O'M.,Conway, B. E., White, R. E., Eds.; Plenum Press: New York, 1993; Vol. 25, p 1.

5. Samec, Z.; Kakiuchi, T. In *Advances in Electrochemical Science and Electrochemical Engineering;* Gerischer, H., Tobias, C. W., Eds.; VCH: New York, 1995; Vol. 4, p 297.

6. Samec, Z. In *Liquid-Liquid Interfaces. Theory and Methods*; Volkov, A. G., Deamer, D. W., Eds.; CRC Press: Boca Raton, 1996.

7. Benjamin, I. *Chem. Rev.* 1996, *96*, 1449.

8. Liu, B.; Mirkin, M. V. *Electroanalysis*, 2000, 12, 1433.

9. Taylor, G.; Girault, H. H. *J. Electroanal. Chem.* 1986, *208*, 179.

10. Shaik, S. S.; Schlegel, H. B.; Wolfe, S. *Theoretical Aspects of Physical Organic Chemistry. The SN2 Mechanism*; Wiley-Interscience: New York, 1992.

11. Marcus, R. A. *J. Phys. Chem. A*1997, *101*, 4072.

12. Harman, W. D. *Chem. Rev.* 1997, *97*, 1953.

13. Ciszkowska, M.; Osteryoung, J. G. *J. Phys. Chem. B* 1998, *102*, 291.

14. Horrocks, B. R.; Mirkin, M. V. *Anal. Chem.* 1998, *70*, 4653.

15. Albery, W. J.; Hitchman, M. L. *Ring-Disc Electrodes*; Calrendon: Oxford,1971.

16. Chidsey, C. E. D.; Feldman, B. J.; Lundgren, C.; Murray, R. W. *Anal.Chem.* 1986, *58*, 601.

17. Varco Shea, T.; Bard, A. J. *Anal. Chem.* 1987,*59*, 2101.

18. Tatistcheff, H. B.; Fritsch-Faules, I.; Wrighton, M. S. *J. Phys.Chem.* 1993, *97*, 2732.

19. Fosset, B.; Amatore, C. A.; Bartelt, J. E.; Michael A. C.; Wightman, R. M. *Anal. Chem.* 1991, *63*, 306.

20. Bard, A. J.; Fan, F.-R. F.; Mirkin, M. V. In *Electroanalytical Chemistry*; Bard, A. J., Ed.; Marcel Dekker: New York, 1994; Vol. 18, p 243.

21. Shao, Y.; Liu, B.; Mirkin, M. V. *J. Am. Chem. Soc.* 1998, *120*, 12700.

22. Liu, B.; Shao, Y.; Mirkin, M. V. *Anal. Chem.* 2000, 72, 510.

23. Brina, R.; Pons; S.; Fleischmann *J. Electroanal. Chem.* 1988, *244*, 81.

24. Fang, Y.; Leddy, J. *J. Electroanal. Chem.* 1995, *384*, 5.

25. Mossier-Boss,P. A.; Lieberman, S. H. *J. Electroanal. Chem.* 1999, *460*, 105.

26. Fan, F.-R. F.; Bard, A. J. *Science* 1995, *270*, 1849.

27. Shao, Y.; Girault, H. H. *J. Electroanal. Chem.* 1990, *282*, 59.

28. Shao, Y.; Mirkin, M. V. *J. Am. Chem. Soc.* 1997, *119*, 8103.

29. Stewart, A. A.; Taylor, G.; Girault, H. H.; McAleer J. *J. Electroanal. Chem.* 1990, *296*, 491

30. Shao, Y.; Mirkin, M. V. *Anal. Chem.* 1998, *70*, 3155.

31. C.G. Phillips, H.A. Stone, *J Electroanal Chem* 1997, 437, 157.

32. Beattie, P. D.; Delay A.; Girault, H. H. *J. Electroanal.Chem.* 1995, *380*, 167.

33. Beattie, P. D.; Wellington, R. G.; Girault, H. H. *J. Electroanal.Chem.* 1995, *396*, 317.

34. Samec, Z.; Marecek, V.; Colombini, M. P. *J. Electroanal. Chem.* 1988,*257*, 147.

35. Shao, Y.; Stewart, A. A.; Girault, H. H. *J. Chem. Soc., Faraday Trans.* 1991, *87*, 2593.

36. Stewart, A. A.; Shao, Y.; Pereira, C. M.; Girault,H. H. *J. Electroanal. Chem.* 1991, *305*, 135.

37. Wei, C.; Bard, A. J.; Feldberg, S. W. *Anal. Chem.* 1997, *69*, 4627.

Chapter IV

1. Adams, R. N. Anal. Chem. 1976, 48, 1128A-1134A.

2. Wightman, R. M., Kennedy, R. T., Wiedemann, D. J., Kawagoe, K. T., Zimmerman, J. B. & Leszczyszyn, D. J. (1991) in Microelectrodes: Theory and Applications, eds. Montenegro, M. I., Queirós, M. A. & Daschbach, J. L. (Kluwer Acad. Publ., Dordrecht), p. 453-462.

3. O'Neill, R. D. (1994) Analyst 119, 767-780.

4. Wightman , R. M., Jankowski, J. A., Kennedy, R. T., Kawagoe, K. T., Schroeder, T. J., Leszczyszyn, D. J., Near, J. A., Diliberto, E. M., Jr. & Viveros, O. H. (1991) Proc. Natl. Acad. Sci. USA 88, 10754-10758.

5. Ewing, A. G., Strein, T. S. & Lau, Y. Y. (1992) Acc. Chem. Res. 25, 440-447.

6. Kennedy, R. T.; Huang, L.; Atkinson, M. A.; Dush, P. (1993) Anal. Chem. 65, 1882-1887.

7. Kuhr, W. G.; Pantano, P. (1995) Electroanalysis 7, 405-416.

8. Lu, H. & Gratzl, M. (1999) Anal. Chem. 71, 2821-2830.

9. Yi, C. & Gratzl, M. (1998) Biophys. J. 75, 2255-2261.

10. T.K. Chan, G. Luo, A.G. Ewing, 1994, Anal. Chem. 66, 3031.

11. B. R. Horrocks, G. Wittstock in Scanning Electrochemical Microscopy, A.J. Bard, M.V. Mirkin, Ed. Marcel Dekker, New York, 2001, pp. 445-519.

12. T Yasukawa, T. Kaya, T. Matsue, Anal. Chem. 2000, 12, 653.

13. Lee, C. M., Kwak, J. Y. & Bard, A. J. (1990) Proc. Natl. Acad. Sci. USA 87, 1740-1743.

14. Tsionsky, M., Cardon, Z. G., Bard, A. J. & Jackson, R. B. (1997) Plant Physiol. 113, 895-901.

15. Yasukawa, T., Kondo, Y. , Uchida, I. & Matsue, T. (1998) Chem. Lett. No. 8, 767-768.

16. Yasukawa, T., Kaya, T. & Matsue, T. (1999) Anal. Chem. 71, 4637-4641.

17. Stryer, L. (1995) Biochemistry (W. H. Freeman and Co., New York).

18. Mayfield, S. P., & Danon, A.. (1994) Science 266, 1717-1720.

19. Ottova-Leitmannova, A. & Tien, H. T. (1993) Progr. Surf. Sci. 41, 337-412.

20. Girault H. H. & Schiffrin, D. J. (1984) in Charge and Field Effects in Biosystems , eds. Allen, M. J. & Usherwood, P. N. R. (Abacus Press, Turnbridge Wells) p. 171-186.

21. Moncelli, M. R., Becucci, L. & Guidelli, R. (1996) Biophys. J. 70, 2716-2722.

22. Tsionsky, M., Bard, A. J. & Mirkin, M. V. (1997) J. Am. Chem. Soc. 119, 10785-10792.

23. Tsionsky, M., Zhou, J., Amemiya, S., Fan, F.-R. F, Bard, A. J. & Dryfe, R. A. W. (1999) Anal. Chem. 71, 4300-4305.

24. Rabinowitz, J. D., Vacchino, J. F., Beeson, C. & McConnell, H. M. (1998) J. Am. Chem. Soc. 120, 2464-2473.

25. Wei, C., Bard, A. J. & Mirkin, M. V. (1995) J. Phys. Chem. 99, 16033-16042.

26. Tsionsky, M., Bard, A. J. & Mirkin, M. V. (1996) J. Phys. Chem. 100, 17881-17888.

27. Barker, A. L., Macpherson, J. V., Slevin, C. J. & Unwin, P. R. (1998) J. Phys. Chem. B 102, 1586-1598.

28. Gopalakrishna, R. & Anderson, W. B. (1989) Proc. Natl. Acad. Sci. USA 86, 6758-6762.

29. Rotenberg, S. A. In: Cellular and Molecular Biology of Nitric Oxide, J. D. Laskin and D. L. Laskin, Eds. Marcel Dekker, Inc., NY, 1999; pp. 171-198.

30. Batlle, E., Verdu, J., Dominguez, D., del Mont Llosas, M., Diaz, V., Loukili, N., Paciucci, R., Alameda, F. & Garcia de Herreros, A. J. Biol. Chem. 273, 15091-15098 (1998).

31. La Porta, C. A. M. & Comolli, R. (1997) Clin. Exp. Metastasis 15, 568-579.

32. Soule, H. D., Maloney, T. M., Wolman, S. R., Peterson, W. D. Jr., Brenz, R., McGrath, C. M., Russo, J., Pauley, R. J., Jones, R. F. & Brooks, S. C. (1990) Cancer Res. 50, 6075-6086.

33. Horrocks, B. R.; Mirkin, M. V.; Pierce, D. T.; Bard, A. J.; Nagy, G.; Toth, K. Anal. Chem. 65 (1993) 1213.

34. Bard, A. J.; Fan, F.-R. F.; Kwak, J.; Lev, O. Anal. Chem. 61 (1989) 1794.

35. Sun, X.-g. & Rotenberg, S. A. (1999) Cell Growth & Diff. 10, 343-352.

36. Barker, A. L.; Unwin, P. R.; Bard, A. J. J. Phys. Chem. B 103: 7260 (1999).

37. Bard, A. J., Fan, F.-R. F. & Mirkin, M. V. (1994) in Electroanalytical Chemistry, Vol. 18, ed. Bard, A. J. (Dekker, New York), pp. 243 – 373.

38. Grimaldi, J. J.; Boileau, S.; Lwhn, J. M.; Nature, 1977, 265, 229.

39. Ohkouchi, T.; Kakutani, T.; Senda, M. "Electrochemical Theory of the Transfer of Protons Across a Biological Membrane Facilitated by Weak Acid Uncouplers Added to the Medium", *Bioelectrochem. Bioenerg. 25:* 81 (1991).

40. Gennis, R. B. *Biomembranes,* Springer, New York, 1995.

41. Stein, W. D., ed. (1986), Transport and Diffusion across Cell Membranes. Academic Press, Orlando, FL.

42. Walter, A., and J. Gutknecht. (1986). J. Membr. Biol. 90, 207-217.

43. Xiang, T.-X., B. D. Anderson. (1994). J. Pharm. Sci. 83, 1511-1518).

44. Xiang, T.-X.; Anderson, B. D. (1998), Biophys J, 75,2658-2671.

45. Martiny-Baron, G.; Kazanietz, M. G.; Mischak, H.; Blumberg, P. M.; Kochs, G.; Hug, H.; Marme, D.; Schachtele, C. J. Biol. Chem. 268: 9194 (1993).

46. Smotkin, E. S.; Moy, F. T.; Plachy, W. Z. Biochim. Biophys. Acta 1061 (1991) 33.

47. Barker, A.L.; Gonsalves, M.; Macpherson, J. V.; Slevin, C. J.; P. R. Unwin, Anal. Chim. Acta 385 (1999) 223.

48. Liu, B.; Rotenberg, S. A.; Mirkin, M. V. Proc. Natl. Acad. Sci. USA 97 (2000) 9855.

49. McConnell, H. M.; Owicki, J. C.; Parce, J. W.; Miller, D. L.; Baxter, G. T.; Wada H. G.; Pitchford, S. Science 257 (1992) 1906.

50. Van Sluis, R.; Bhujwalla, Z. M.; Raghunand, N.; Ballesteros, P.; Alvarez, J.; Cerdan, S.; Galons, J. P.; Gillies, R. J. Magn. Reson. Med. 41 (1999) 743.

51. Montcourrier, P.; Silver, I.; Farnout R.; Bird, I.; Rochefort, H. Clin. Exp. Metastasis 15 (1997) 382.

52. Wei, C.; Bard, A. J.; Nagy, G.; Toth, K. "Scanning Electrochemical Microscopy 28. Ion-Selective Neutral Carrier-Based Microelectrode Potentiometry", *Anal. Chem. 67:* 1346 (1995).

53. Horrocks, B. R.; Mirkin, M. V. "Evidence for a Potential-Dependent Reversible Inactivation of Urease Adsorbed on a Gold Electrode", *J. Chem. Soc. Faraday Trans. 94:*1115 (1998).

54. Ekelund, S.; Nygren, P.; Larsson, R. Anticancer Drugs 9 (1998) 531.